Global Carbon Budget 2026 - Supplementary Information

S.1 Methodology Fossil Fuel CO_2 emissions (E_{FOS})

S.1.1 Cement carbonation

From the moment they are created, cement products begin to absorb CO_2 from the atmosphere, a process known as 'cement carbonation'. We estimate this CO_2 sink, from 1931 onwards, as the average of three studies in the literature (Cao et al., 2020; Niu et al., 2025; Xiao et al., 2026). The Global Cement and Concrete Association reports a much lower carbonation rate, but this is based on the highly conservative assumption of 0% mortar (GCCA, 2021). Modelling cement carbonation requires estimation of a large number of parameters, including the different types of cement material in different countries, the lifetime of the structures before demolition, of cement waste after demolition, and the volumetric properties of structures, among others (Xi et al., 2016). Lifetime is an important parameter because demolition results in the exposure of new surfaces to the carbonation process. The main reasons for differences between the studies are assumed lifetimes of cement structures, geographic resolution, whether mortar is modelled separately, and whether end-of-life and secondary use phases are included.

S.1.2 Emissions embodied in goods and services

Our national emission statistics are in line with IPCC reporting guidelines and 'include greenhouse gas emissions and removals taking place within national territory and offshore areas over which the country has jurisdiction' (Rypdal et al., 2006), and are called territorial emission inventories. Consumption-based emission inventories allocate emissions to products that are consumed within a country and are conceptually calculated as the territorial emissions minus the 'embodied' territorial emissions to produce exported products plus the emissions in other countries to produce imported products (Consumption = Territorial – Exports + Imports). Consumption-based emission attribution results (e.g. Davis and Caldeira, 2010) provide additional information to territorial-based emissions that can be used to understand emission drivers (Hertwich and Peters, 2009) and quantify emission transfers by the trade of products between countries (Peters et al., 2011a). The consumption-based emissions have the same global total but reflect the trade-driven movement of emissions between countries in response to human activities.

We estimate consumption-based emissions from 1990 by enumerating the global supply chain using a global model of the economic relationships between economic sectors within and between every country (Andrew and Peters, 2013; Peters et al., 2011b). Our analysis is based on the economic and trade data from the Global Trade and Analysis Project (GTAP; Narayanan et al., 2015), and we make detailed estimates for the years 1997 (GTAP version 5), 2001 (GTAP6), and 2004, 2007, 2011, 2014, and 2017 (GTAP11.0), covering 57 sectors and 141 countries and regions. The detailed results are then extended into an annual time series from 1990 to the latest year of the Gross Domestic Product (GDP) data (typically one year less than the territorial emissions data), using GDP data by expenditure in current exchange rate of US dollars (USD; from the UN National Accounts main Aggregates database; UN, 2025) and time series of trade data from GTAP (based on the methodology in Peters et al., 2011b). We estimate the sector-level CO_2 emissions using the GTAP data and

methodology, add the flaring and cement emissions from our fossil CO_2 dataset, and then scale the national totals (excluding bunker fuels) to match the emission estimates from the carbon budget. We do not provide a separate uncertainty estimate for the consumption-based emissions, but based on model comparisons and sensitivity analysis, they are unlikely to be significantly different than for the territorial emission estimates (Peters et al., 2012b).

S.1.3 Uncertainty assessment for E_{FOS}

We estimate the uncertainty of the global fossil CO_2 emissions at ±5% (scaled down from the published ±10 % at ±2σ to the use of ±1σ bounds reported here; Andres et al., 2012). This is consistent with a more detailed analysis of uncertainty of ±8.4% at ±2σ (Andres et al., 2014) and at the high-end of the range of ±5-10% at ±2σ reported by (Ballantyne et al., 2015). This includes an assessment of uncertainties in the amounts of fuel consumed, the carbon and heat contents of fuels, and the combustion efficiency. While we consider a fixed uncertainty of ±5% for all years, the uncertainty as a percentage of emissions is growing with time because of the larger share of global emissions from emerging economies and developing countries (Marland et al., 2009). Generally, emissions from mature economies with good statistical processes have an uncertainty of only a few per cent (Marland, 2008), while emissions from strongly developing economies such as China have uncertainties of around ±10% (for ±1σ; Gregg et al., 2008; Andres et al., 2014). Uncertainties of emissions are likely to be mainly systematic errors related to underlying biases of energy statistics and to the accounting method used by each country.

S.1.4 Growth rate in emissions

We report the annual growth rate in emissions for adjacent years (in percent per year) by calculating the difference between the two years and then normalising to the emissions in the first year: $(E_{FOS}(t_0+1)-E_{FOS}(t_0))/E_{FOS}(t_0)\times 100\%$. We apply a leap-year adjustment where relevant to ensure valid interpretations of annual growth rates. This affects the growth rate by about 0.3% yr^{-1} (1/366) and causes calculated growth rates to go up approximately 0.3% if the first year is a leap year and down 0.3% if the second year is a leap year.

The relative growth rate of E_{FOS} over time periods of greater than one year can be rewritten using its logarithm equivalent as follows:

$$\frac{1}{E_{FOS}}\frac{dE_{FOS}}{dt} = \frac{d(lnE_{FOS})}{dt} \quad \text{(S1)}$$

Here we calculate relative growth rates in emissions for multi-year periods (e.g. a decade) by fitting a linear trend to $ln(E_{FOS})$ in Eq. (S1), reported in percent per year. We define the average growth rate over a decadal period to include the growth in the first year. For example, when calculating the growth rate of 2000-2009, we include the growth rate in the year 2000, thus the regression is for the years 1999-2009, otherwise the growth from 1999-2000 would not be included in either 1990-1999 or 2000-2009 time periods.

S.1.5 Emissions projection for 2026

To gain insight on emission trends for 2026, we provide an assessment of global fossil CO_2 emissions, E_{FOS}, by combining individual assessments of emissions for China, USA, the EU, India, and Japan (five countries/regions with the largest emissions), international aviation, international shipping, and the rest of the world.

The methods are specific to each country or region, as described in detail below.

China: We use a regression between monthly data for each fossil fuel and cement, and annual data for consumption of fossil fuels / production of cement to project full-year growth in fossil fuel consumption and cement production. The monthly data for each product consists of the following:

- Coal: Production data from the National Bureau of Statistics (NBS), plus net imports from the China Customs Administration (i.e., gross supply of coal, not including inventory changes), adjusted using monthly production data for thermal electricity, crude steel, pig iron, coke and cement from NBS.
- Oil and Natural gas: Production data from NBS, plus net imports from the China Customs Administration (i.e., gross supply, not including inventory changes)
- Cement: Production data from NBS

For oil, we use data for production and net imports of refined oil products rather than crude oil. This choice is made because refined products are one step closer to actual consumption, and because crude oil can be subject to large market-driven and strategic inventory changes that are not captured by available monthly data.

For each fuel and cement, we make a Bayesian linear regression between year-on-year cumulative growth in supply (production for cement) and full-year growth in consumption (production for cement) from annual consumption data. In the regression model, the growth rate in annual consumption (production for cement) is modelled as a regression parameter multiplied by the cumulative year-on-year growth rate from the monthly data through the last month of observation (m) of each year for past years (through 2025). We use broad Gaussian distributions centered around 1 as priors for the ratios between annual and through-m growth rates. We then use the posteriors for the growth rates together with cumulative monthly supply/production data through month m of 2026 to produce a posterior predictive distribution for the full-year growth rate for fossil fuel consumption / cement production in 2026.

If the growth in supply/production through the last month of observation were an unbiased estimate of the full-year growth in consumption/production, the posterior distribution for the ratio between the monthly and annual growth rates would be centered around 1. However, in practice the ratios are different from 1 (in most cases below 1). This is a result of various biasing factors such as uneven evolution in the first and second half of each year, inventory changes that are somewhat anti-correlated with production and net imports, differences in statistical coverage, and other factors that are not captured in the monthly data.

For fossil fuels, the mean of the posterior distribution is used as the central estimate for the growth rate in 2026, while the edges of a 68% credible interval (analogous to a 1-sigma confidence interval) are used for the upper and lower bounds.

USA: We use emissions estimated by the U.S. Energy Information Administration (EIA) in their Short-Term Energy Outlook (STEO) for emissions from fossil fuels to get a full year projection (EIA, 2026). The STEO uses a near-term forecast based on an energy forecasting model which is updated monthly (we use the October 2026 edition), and takes into account expected temperatures, household expenditures by fuel type, energy markets, policies, and other effects. We combine this with our estimate of emissions from cement production

using the monthly U.S. cement clinker production data from USGS for January-June 2026, assuming changes in clinker production over the first part of the year apply throughout the year.

India: We use monthly emissions estimates for India updated from Andrew (2020b) through August/September 2026. These estimates are derived from many official monthly energy and other activity data sources to produce direct estimates of national CO_2 emissions, without the use of proxies. Emissions from coal are then extended using a regression relationship based on power generated from coal, coal dispatched by Coal India Ltd. (CIL) and the Singareni Collieries Company Limited (SCCL), the composite Purchasing Managers' Index (PMI), time, and days per month. For the last months of the year without observations, each series is extrapolated assuming typical trends from previous years.

EU: We use a refinement to the methods presented by Andrew (2021), deriving emissions from monthly energy data reported by Eurostat. Some data gaps are filled using data from the Joint Organisations Data Initiative (JODI, 2026). Sub-annual cement and cement-clinker production data are limited, but data for Germany, Poland and Spain, the three largest producers, are available, and we also use indices of cement production for France and Italy. For fossil fuels this provides estimates through July-September, varying by fuel. We extend coal emissions through October using a regression model built from generation of power from hard coal, power from brown coal, and the number of working days in Germany, the biggest coal consumer in the EU, and then extend through December using typical trends. We extend oil emissions through December by building a regression model between our monthly CO_2 estimates and oil consumption reported by the EIA for Europe in its Short-Term Energy Outlook (October 2025 edition), and then using this model with EIA's monthly forecasts. For natural gas, we first extend through September using the daily demand estimation method of Fernandez-Blanco et al. (2024) and then extend through December using Holt-Winters, which captures recent trends.

Japan: We derive estimates of monthly emissions from official monthly activity data including energy flows and industrial production statistics (Kunimitsu & Andrew, *accepted*). This gives very robust estimates through July, which we extend through December using typical trends from previous years.

International transport: Given the divergence in behaviour of international shipping from countries' emissions since the COVID-19 pandemic, we project international bunkers separately. For aviation we construct a model of available seat kilometres (ASK) and cargo-dedicated flights using data from IATA and assume some recovery before the end of the year from the dip caused largely by a sharp reduction of traffic in the Middle East, but still well below the previous trend. For international shipping, while there has been a sharp drop in shipping from the Middle East, much of this has been made up with increased supply elsewhere, often on much longer routes. No reliable estimates of sub-annual international shipping emissions are available. Data from AIS have become less reliable, not only because of many more ships disabling their transmitters or spoofing their locations, but also because of ship-to-ship transfers of cargoes, which turn one international voyage into two non-international voyages. We combine information from the OECD, ClimateTRACE, and bunker-fuel sales from major ports to qualitatively arrive at a reduction of -1%.

Rest of the world: For oil and gas emissions, we use the global oil demand forecast (EIA) and global gas demand forecast (IEA) and subtract the other regions explicitly modelled, and estimate uncertainty as the maximum absolute difference over the period available for such forecasts using the specific monthly editions of the respective forecasts. For coal and cement, we use the close relationship between the growth in GDP and the

growth in emissions (Raupach et al., 2007) to project emissions for the current year. This is based on a simplified Kaya Identity, whereby E_{FOS} (GtC yr^{-1}) is decomposed by the product of GDP (USD yr^{-1}) and the fossil fuel carbon intensity of the economy (I_{FOS}; GtC USD^{-1}) as follows:

$$E_{FOS} = GDP \times I_{FOS} \quad \text{(S2)}$$

Taking a time derivative of Equation (S2) and rearranging gives:

$$\frac{1}{E_{FOS}}\frac{dE_{FOS}}{dt} = \frac{1}{GDP}\frac{dGDP}{dt} + \frac{1}{I_{FOS}}\frac{dI_{FOS}}{dt} \quad \text{(S3)}$$

where the left-hand term is the relative growth rate of E_{FOS}, and the right-hand terms are the relative growth rates of GDP and I_{FOS}, respectively, which can simply be added linearly to give the overall growth rate.

The I_{FOS} is based on GDP in constant PPP (Purchasing Power Parity) from the International Energy Agency (IEA) up to 2017 (IEA/OECD, 2019) and extended using the International Monetary Fund (IMF) growth rates through 2024 (IMF, 2024). Interannual variability in I_{FOS} is the largest source of uncertainty in the GDP-based emissions projections. We thus use the standard deviation of the annual I_{FOS} for the last decade as a measure of uncertainty, reflecting a $\pm 1\sigma$ as in the rest of the carbon budget.

World: The global total is the sum of each of the countries and regions.

S.1.6 Carbon Monitor projection

We use a time series forecasting model based on an additive decomposition framework to predict the full-year CO_2 emissions in 2026. The model separates the emission dynamics into four structural components: $\gamma(t)=g(t)+s(t)+h(t)+\varepsilon$

Where $g(t)$ is the trend function, capturing long-term directional changes in emissions; $s(t)$ represents the temporal patterns, e.g. seasonality; $h(t)$ denotes the holiday effects, encoding country-specific public holidays and major events that disrupt normal activity (e.g., Spring Festival holidays in China, COVID-19 lockdowns); ε is the errors, representing stochastic variability not explained by the above components.

Historical daily CO_2 emissions data from Carbon Monitor, spanning January 1, 2019 to July 31, 2026, are used as input. Data are disaggregated by country and sector to capture heterogeneous emission patterns. Each country–sector series is modeled independently to preserve unique structural dynamics. The fitted models generate daily predictions for August 1 to December 31, 2026, which are then aggregated to produce annual projections at both the national and global levels. To quantify predictive uncertainty, we generate 68% confidence intervals using repeated parameter sampling and residual bootstrapping. These intervals reflect both model uncertainty and unexplained variability in historical emissions.

S.2 Methodology CO_2 fluxes from land-use change and land management (E_{LUC})

The net CO_2 flux from land-use change and land management (E_{LUC}, hereafter referred to as net land-use change emissions) includes CO_2 fluxes from deforestation and clearing of other natural vegetation, afforestation and reforestation, logging and forest degradation (including harvest activity), shifting cultivation (cycle of cutting forest for agriculture, then abandoning), regrowth of forests and other natural vegetation following wood harvest or abandonment of agriculture, peat burning and peat drainage, and transitions between cropland, pasture and

urban areas. Land-management activities are only partly included in our land-use change emissions estimates (Table S1). Some land-use change and land-management activities cause emissions of CO_2 to the atmosphere, while others remove CO_2 from the atmosphere. E_{LUC} is the net sum of emissions and removals due to all anthropogenic activities considered. Our annual estimates for 1959-2024 are provided as the average of results from three bookkeeping models (Supplement S.2.2): the Bookkeeping of Land Use Emissions model (BLUE; Hansis et al., 2015), the compact Earth system model OSCAR (Gasser et al., 2020), and the Land-Use Change Emissions model (LUCE; Qin et al., 2024). Peat emissions are added from external datasets (Supplement S.2.2). BLUE and OSCAR are updated with new land-use forcing data covering the time period until 2024 (Supplement S.2.1). E_{LUC} data are extrapolated to provide a projection for 2026 (Supplement S.2.6). In addition, we use results from Dynamic Global Vegetation Models (DGVMs; see Supplement S.2.3 and Table 4) to help quantify the uncertainty in E_{LUC} (Supplement S.2.5), and thus better characterise the robustness of annual estimates and trends. In this budget, we follow the E_{LUC} definition as used by global carbon cycle models, which counts fluxes due to environmental changes on managed land towards S_{LAND}, as opposed to the national greenhouse gas inventories (NGHGIs) under the UNFCCC, most of which include them in their estimate of fluxes from land use, land-use change and forestry (LULUCF) and thus often report smaller net land-use emissions (Grassi et al., 2023). Following the translation methodology of Grassi et al. (2023), we provide reconciled estimates of the two approaches further below (Supplement S.2.4).

S.2.1 Land-Use and Land Use Change Datasets

Bookkeeping models and DGVMs use the harmonised land-use change data LUH2-GCB2026 covering the period 850-2025 as input to estimate E_{LUC} (an update to the previously released LUH2 v2h dataset; Hurtt et al., 2017; Hurtt et al., 2020). LUH2-GCB2026 provides land-use change data at 0.25° spatial resolution based on data from the Food and Agriculture Organization of the United Nations (FAO, 2025) as well as the HYDE365 dataset (Klein Goldewijk et al., 2017a, 2017b), considering subgrid-scale transitions between primary forest, secondary forest, primary non-forest, secondary non-forest, cropland, pasture, rangeland, and urban land (Hurtt et al., 2020; Chini et al., 2021).

S.2.1.1 HYDE3.6

The HYDE3.6 cropland/grazing/urban land dataset is constrained by FAO country-level statistics (FAO, 2025; bulk download February 2025) for the years 1961-2023. HYDE uses satellite imagery from ESA-CCI from 1992-2018 for more detailed yearly allocation of cropland and grazing land, with the ESA-CCI area data scaled to match the FAO annual totals at country-level. The 2018 map is also used for the 2019-2025 period. The original 300 metre spatial resolution data from ESA is aggregated to a 5 arc minute resolution according to the classification scheme as described in Klein Goldewijk et al. (2017a).

Similar to GCB2025 we replace the FAO timeseries for China, based on province-level area totals from Yu et al. (2022) for the 1900-2024 period. For Brazil and Indonesia, we replace the full FAO time series with time series based on MapBiomas state-level area totals (available for 1985-2024 for Brazil and 2000-2024 for Indonesia) (MapBiomas Brasil, Souza et al., 2020, MapBiomas Indonesia). For Indonesia, MapBiomas replaces cropland only, which includes oil palm plantations as does FAO, while grazing land is taken from FAO. For the

pre-1985 period, the per-capita cropland area in 1985 is calculated for each state of Brazil (based on MapBiomas) and scaled with the historical population development for each state of Brazil. A similar methodology is adopted for land cover change information from MapBiomas for Indonesia.

S.2.1.2 LUH2-GCB2026

LUH2-GCB2026 is an update of the comprehensive harmonised land-use data set version 2 (Hurtt et al., 2020), which includes fractional data on primary and secondary forest vegetation, as well as all underlying transitions between land-use states (Hurtt et al., 2011, 2017, 2020; Chini et al., 2021; Table S1). LUH2-GCB2026 covers the period 850-2025 and consists of 0.25° fractional areas of land-use states and all transitions between those states, including an updated wood harvest reconstruction and updated representation of shifting cultivation, crop rotation, and management information including irrigation and fertiliser application. The land-use states include five different crop types in addition to splitting grazing land into managed pasture and rangeland. Wood harvest patterns are constrained with Landsat-based tree cover loss data (Hansen et al. 2013).

The complete LUH2-GCB2026 forcing timeseries is updated to use the new HYDE3.6 land-use and population data. LUH2-GCB2026 uses the FAO national wood harvest production data for 1961-2024 along with the new HYDE3.6 population data to reconstruct the historical wood harvest time-series. Wood production data is linearly extended to the year 2025. In addition, the land-use time series is extended beyond the years that are directly informed by data in HYDE (e.g., beyond 2023 for those countries based on FAO country-level statistics) to include land-use states up to and including the year 2026 (and land-use transitions during the year 2025). A simple extension of the previous 5-year trend for each gridcell is applied. Updates in the land-use forcing are shown in Figure S1 in comparison to LUH2-GCB2024 and LUH2-GCB2025.

LUH2-GCB2026 provides a distinction between rangelands and pasture, based on inputs from HYDE. DGVM and bookkeeping modelling groups in the past have requested more information on whether natural vegetation is lost in conversion to pasture or rangelands. LUH2 guidelines suggest that rangelands are established after clearing of forests and managed pastures are established after clearing of all other natural vegetation. Therefore, (1) rangeland establishment in forests is assumed to transform forests to grasslands, (2) rangeland establishment in non-forest primary vegetation degrades primary to secondary vegetation, and (3) rangeland establishment in non-forest secondary vegetation has no effect (e.g., browsing on shrubland; Ma et al., 2020). In the bookkeeping model BLUE, this case distinction is implemented based on a forest mask provided with LUH2-GCB2021.

S.2.2 Bookkeeping models

CO_2 emissions and removals from land-use change are calculated by three bookkeeping models. These are based on the original bookkeeping approach of Houghton (2003), which keeps track of the carbon stored in vegetation and soils before and after a land-use change event (transitions between various natural vegetation types, croplands, and pastures). Literature-based response curves describe the decay of vegetation and soil carbon, including carbon transfer to product pools of different lifetimes, as well as carbon uptake due to regrowth. In addition, the bookkeeping models represent long-term degradation of primary forest as lowered standing vegetation and soil carbon stocks in secondary forests and include forest management practices such as wood harvests.

All three GCB2026 bookkeepings models use transient carbon densities to estimate E_{LUC}, i.e., they consider the effects of environmental changes, such as atmospheric CO_2 increase and impacts of climate change, on vegetation and soil carbon densities. The consideration of environmental changes to estimate E_{LUC} does not interfere with S_{LAND} estimates. In fact, the consideration of environmental effects on E_{LUC} and the updated methodology to estimate S_{LAND} (see Supplement S.4.1) delivers a conceptually consistent terrestrial carbon budget (Pongratz et al. 2014; Dorgeist et al., 2024). OSCAR already includes the transient response in its E_{LUC} estimates (Gasser and Ciais, 2013; Gasser et al., 2020). The static carbon densities of BLUE and LUCE were both updated using time-varying DGVM data from TRENDYv14-GCB2025 following the method described in Dorgeist et al. (2024). Vegetation and soil carbon densities were used to derive scaling factors, benchmarked to their 1980 values. These scaling factors are applied to the original carbon densities of BLUE and LUCE. The updated carbon densities maintain the original spatial resolution but with temporal changes following DGVMs. Scaling factors for vegetation carbon densities were derived from the DGVMs CABLE-POP, CLM, IBIS, ISAM, JSBACH, JULES-ES, LPJ-GUESS, LPJml, LPX-Bern, ORCHIDEE, and iMAPLE, and scaling factors for soil carbon densities were derived from the DGVMs CABLE-POP, IBIS, ISAM, JSBACH, ORCHIDEE, iMAPLE.

The bookkeeping models differ in (1) computational units (spatially explicit treatment of land-use change at 0.25° resolution for BLUE and LUCE, country-level for OSCAR), (2) processes represented (see Table S1), and (3) carbon densities assigned to vegetation and soils for different types of vegetation (literature-based for BLUE, calibrated to DGVMs for OSCAR, mainly literature-based but additionally considering the impact of land cohort age on secondary land carbon stocks for LUCE). All three bookkeeping models include subgrid-scale transitions between all vegetation types, and they allocate pasture transitions proportionally to all natural vegetation that exists in a grid cell.

The three bookkeeping estimates used in this study also differ with respect to the land-use change data used to drive the models. BLUE and LUCE use the harmonised land-use change data LUH2-GCB2026. OSCAR was run with both LUH2-GCB2026 and data from the Forest Resource Assessment (FRA) of FAO (using data from FAO, 2020), which provides statistics on forest-area change and management at intervals of five years. The data is based on country reporting to FAO and may include remote-sensing information in more recent assessments. Changes in land use other than forests are based on annual, national changes in cropland and pasture areas reported by FAO (FAO, 2021). FAO/FRA data were linearly extrapolated to 2025 using their 2015-2020 trends. The best-guess OSCAR estimate used in our study is a combination of results for LUH2-GCB2026 and FAO/FRA land-use data and a large number of perturbed parameter simulations weighted against a constraint (the cumulative S_{LAND} over 1960-2024 of last year's GCB).

Bookkeeping models do not directly capture carbon emissions from the organic layers of drained peat soils nor from peat fires. Particularly the latter can create large emissions and interannual variability due to synergies of land-use and climate variability in equatorial Southeast Asia, especially during El-Niño events. We add peat fire emissions in equatorial Southeast Asia based on the Global Fire Emission Database (GFED5.1; van der Werf et al., 2025) to the bookkeeping models' output. Peat fire emissions are calculated by multiplying the mass of dry matter emitted by peat fires with the carbon emission factor for peat fires (considering CO_2 and CO emissions) indicated in the GFED5.1 database. Emissions from tropical deforestation and degradation fires used to derive

the 2026 E_{LUC} projection (Supplement S.2.6) are calculated analogously. The satellite-derived GFED5.1 estimates of peat fire emissions start in 1997. For the previous years, we follow the approach by Houghton and Nassikas (2017), which linearly ramps up from zero emissions in 1980 to 0.07 GtC yr^{-1} in 1996, reflecting the onset of major clearing of peatlands in equatorial Southeast Asia in the 1980s.

We also add peat drainage emissions, combining estimates from three spatially explicit datasets. We employ peat drainage emissions 1990–2025 from croplands and grasslands provided by FAO (Conchedda and Tubiello, 2020; FAO, 2026a), peat drainage emissions 1700–2010 from simulations with the DGVM ORCHIDEE-PEAT (Qiu et al., 2021), and peat drainage emissions 1701–2025 from simulations with the DGVM LPX-Bern v1.5 (Lienert and Joos, 2018; Müller and Joos, 2021), the latter applying the updated LUH2-GCB2026 forcing as also used by BLUE, OSCAR, LUCE, and the DGVMs. The LPX-Bern simulations start from a transient run over the last deglaciation (-20,050 to 1700 AD) following Müller and Joos (2020) and are forced by changes in climate, atmospheric CO_2, nitrogen deposition/input, and land-use changes. Simulations were done with and without prescribing land-use changes since 1700 AD. The difference between the simulations represents anthropogenic peat drainage emissions. To account for internal variability, we used the median peat drainage emissions from a 20-member ensemble. In LPX-Bern, peat carbon is stored in (i) active peatlands, (ii) former peatlands ("natural"), and (iii) former peatlands under anthropogenic use. We average the two CO_2 emission cases from Müller and Joos (2021), assuming that half the peat carbon is lost immediately to the atmosphere after transformation from active to former peatland, while the rest decays slowly, depending on local temperature and soil moisture. The LPX-Bern peat drainage emissions show a very high emission peak in Russia in 1959 followed by very low emissions in 1960. This peak can be attributed to an artefact in the HYDE dataset, which was corrected for Brazil and the Democratic Republic of the Congo in GCB2022 (Friedlingstein et al. 2022b) but remains for Russia where it strongly impacts the LPX-Bern peat drainage estimates in 1959 and 1960. To correct for this unrealistic peak, we replace the LPX-Bern peat drainage emissions in Russia in 1959 and 1960 by the average of the estimates in 1958 and 1961. The FAO peat drainage emissions are extrapolated to 1850-2025 by linearly increasing tropical peat drainage emissions between 1980 and 1990 starting from 0 GtC yr^{-1} in 1980 (consistent with Houghton and Nassikas, 2017), and by keeping pre-1990 emissions from the often old, drained areas of the extra-tropics constant at 1990 emission levels. The ORCHIDEE-PEAT data are extrapolated to 2011-2025 by replicating the average emissions in 2000-2010 (pers. comm. C. Qiu). Further, ORCHIDEE-PEAT only provides peat drainage emissions north of 30°N, and thus we fill the regions south of 30°N by the average peat drainage emissions from FAO and LPX-Bern. The final peat drainage emissions are calculated as the average of the estimates from the three different peat drainage datasets.

We provide a split of net E_{LUC} into component fluxes to give more insight into the drivers of net E_{LUC} and to better identify reasons for divergence between bookkeeping estimates. This split distinguishes between total emissions from deforestation and clearing of other vegetation (including due to shifting cultivation), total removals from (re-)growth of forest and other vegetation (including regrowth in shifting cultivation cycles), fluxes from wood harvest and other forest management (including emissions from slash decay in forests, emissions from product decay following wood harvesting, and removals from regrowth after wood harvesting), emissions from peat drainage and peat fires, and emissions and removals from transitions between cropland, pasture, and urban areas. Additionally, we split emissions from deforestation and clearing of other vegetation into emissions from permanent deforestation, emissions from permanent clearing of shrub and herbaceous

vegetation, emissions from deforestation in shifting cultivation cycles, and emissions from clearing of shrub and herbaceous vegetation in shifting cultivation cycles. Similarly, we split removals from (re-)growth of forest and other vegetation into permanent forest (re-)growth due to re/afforestation, permanent (re-)growth of shrub and herbaceous vegetation, forest regrowth in shifting cultivation cycles, and regrowth of shrub and herbaceous vegetation in shifting cultivation cycles. This distinction is insightful with regard to the levers on the reduction of net emissions: as deforestation and clearing of other vegetation for shifting cultivation is only temporary, the associated CO_2 emissions cannot easily be avoided without compromising the CO_2 removals from regrowth in shifting cultivation cycles. By contrast, permanent deforestation is typically not directly related to re/afforestation. Stopping deforestation for permanent agricultural expansion and increasing the forest area provide two independent levers for net emissions reduction.

E_{LUC} data are provided as global sums, as spatially explicit estimates at 0.25° spatial resolution (i.e., the native LUH2-GCB2026 resolution), and for 199 countries (based on the list of UNFCCC parties). Spatially explicit E_{LUC} estimates for BLUE and LUCE are directly available at 0.25°. For OSCAR, the country-level estimates were scaled to 0.25° based on the patterns of gross emissions and gross removals in BLUE (following the methodology of Schwingshackl et al., 2022). The global net E_{LUC} values indicated in the manuscript are the sum of E_{LUC} estimates from bookkeeping models, peat drainage emissions (average of FAO, LPX-Bern, and ORCHIDEE-PEAT), and peat fire emissions (from GFED5.1). Annual E_{LUC} estimates from 1850 onwards are calculated as the average of the estimates from BLUE, OSCAR, and LUCE plus emissions from peat fires and peat drainage. For the cumulative numbers starting in 1750, emission estimates between 1750-1850 are added based on the average of four earlier publications (30 ± 20 GtC 1750-1850, rounded to nearest 5; Le Quéré et al., 2016). The gridded net E_{LUC} estimates of BLUE, LUCE, and OSCAR are averaged, and the gridded estimates of peat drainage emissions and of peat fire emissions are added. Country-level estimates for the gridded datasets (BLUE, LUCE, LPX-Bern, ORCHIDEE-PEAT, GFED5.1) are calculated based on a country map from Eurostat (Eurostat, 2024), which was remapped to 0.25°. In case multiple countries are present in a 0.25° grid cell, the E_{LUC} estimates are allocated proportional to each country's land fraction in that grid cell.

S.2.3 Dynamic Global Vegetation Models (DGVMs)

All DGVMs represent processes of vegetation growth and mortality, as well as decomposition of dead organic matter associated with natural cycles, and include the vegetation and soil carbon response to increasing atmospheric CO_2 concentration, to climate variability and to climate change. Most models explicitly simulate the coupling of carbon and nitrogen cycles and account for atmospheric N deposition and N fertilisers (Table S1). The DGVMs are independent from the other budget terms except for their use of atmospheric CO_2 concentration to calculate the fertilisation effect of CO_2 on plant photosynthesis. Land-use change CO_2 emissions are also estimated by an ensemble of 23 DGVMs. The DGVMs account for deforestation and regrowth, the most important components of E_{LUC}, but they do not represent all processes resulting directly from human activities on land (Table S1).

All DGVMs use the LUH2-GCB2026 dataset as input to estimate the land use change CO_2 fluxes. which includes the HYDE cropland/grazing land dataset (Klein Goldewijk et al., 2017a, 2017b), and some additional information on land-use transitions, land-use management activities and wood harvest. DGVMs that do not

simulate subgrid-scale transitions (i.e., those estimating net land-use emissions; see Table S1) use the HYDE information on agricultural area change. DGVMs implement land-use change in different ways (e.g., an increased cropland fraction in a grid cell can either be at the expense of grassland, shrubs, or forest, the latter resulting in deforestation; land cover fractions of non-agricultural land differ between models). Similarly, model-specific assumptions are applied to convert deforested biomass or deforested area, and other forest product pools into carbon, and different choices are made regarding the allocation of rangelands as natural vegetation or pastures.

As a criterion for inclusion in this carbon budget, we only retain models that simulate a positive E_{LUC} during the 1990s, as assessed in the IPCC AR4 (Denman et al., 2007) and AR5 (Ciais et al., 2013). All DGVMs met this criterion.

This year, DGVM estimates of E_{LUC} are calculated as the difference between simulation S4, with time-varying land-use change but pre-industrial atmospheric CO_2 and climate, and the control simulation S0, with all forcings held constant (see section S.4.1). Because CO_2 and climate are held at pre-industrial levels, S0-S4 does not capture how environmental change has altered the carbon densities of land affected by land-use change (δL). For example, vegetation grown under elevated CO_2 holds more carbon, so clearing it releases more. To account for this missing term, we add the δL component estimated from the mean of the bookkeeping models to the DGVM S0-S4 E_{LUC}.

S.2.4 Translation between NGHGI and bookkeeping estimates

Net land-use emissions estimates from bookkeeping models and from national GHG Inventories (NGHGIs) show a large gap (Figure 8 and Table S11). This gap is due to different approaches for calculating anthropogenic CO_2 fluxes related to land-use change and land management (Grassi et al. 2018). Land sinks due to environmental changes on managed land are treated as non-anthropogenic in the GCB assessments, while they are generally considered as anthropogenic in NGHGIs ("indirect anthropogenic fluxes"; IPCC, 2006). Building on previous studies (Grassi et al. 2023, Melo et al. 2026a), we implement a translation approach that adds the DGVM estimates of CO_2 fluxes due to environmental change in managed forest areas (part of S_{LAND}) to the E_{LUC} estimate from bookkeeping models. The translated E_{LUC} values are expected to be conceptually more comparable to the LULUCF flux estimates from NGHGIs.

LULUCF data from NGHGIs are those in the LULUCF data hub V4.1.0 (Melo et al., 2026b). They are collected and processed based on country data submitted to the UNFCCC, as described in detail by Melo et al. (2026a). While Annex I countries report a complete time series 1990-2024, gap-filling was applied for many Non-Annex I countries through linear interpolation between two points and/or through extrapolation backward (till 2000) and forward (till 2024) using the single closest available data. For this assessment, the NGHGI estimates of the year 2025 are assumed to be equal to those of 2024. NGHGI data include all CO_2 fluxes from land considered managed (forest land, cropland, grassland, wetlands, settlements, and other land), changes among these land categories, and emissions from organic soils (i.e., from peat drainage), from harvested wood products and from fires. Almost all Annex I countries report all land uses, whereas many non-Annex I countries report only on deforestation and forest land, and only few countries report on other land uses. Similarly, Annex I countries

typically report most carbon pools (biomass, dead organic matter, soil), whereas non-biomass pools are reported less frequently by non-Annex I countries.

In most cases, NGHGIs include most of the natural response to recent environmental changes because they use direct observations (e.g., national forest inventories) that do not allow separating direct and indirect anthropogenic effects (IPCC, 2006; Grassi et al., 2018). These effects are considered to be particularly relevant in forests (Grassi et al., 2023). To improve comparability with NGHGIs, the natural land sink (S_{LAND}) in managed forests (only including carbon fluxes due to environmental change and excluding land-use change fluxes) is added to the results from bookkeeping models to make them comparable to LULUCF estimates from NGHGIs (Figure 8).

The calculation of S_{LAND} in managed forests broadly follows the methodology described in Grassi et al. (2023). However, we use the corrected S_{LAND} estimates from DGVMs in the TRENDYv15-GCB2026 dataset (see Supplement S.4.1), thereby eliminating the need for certain processing steps. Specifically, the S2 simulation is no longer used, and the earlier correction of forest NBP by the ratio between observed and prescribed forest cover (see Friedlingstein et al., 2026a) is no longer applied. For DGVMs that disaggregate NBP by plant functional type (PFT), we use forest PFTs only. For all other DGVMs, the total grid-cell NBP is used for all grid cells containing forest. Results are then masked using a proxy map of managed forest (Rossi et al., 2024) for different years (2000, 2010 and 2020). This map is based on global Earth observation-derived tree cover data (Hansen et al., 2013) and country-based information on managed and unmanaged forests. Several countries indicate that all forest is managed (e.g. China, India, Australia, most European countries), and a few provide geospatial polygons of managed forest areas (Brazil, Canada, USA). Some countries report only the total extent of managed and unmanaged forest without maps (e.g. Russia), or provide no specific information on managed land (most developing countries). In these cases, maps of intact and non-intact forest areas (Potapov et al., 2017) are used as proxies for unmanaged and managed forests in NGHGIs, respectively (Grassi et al., 2023). The detailed DGVM processing steps are explained in Alkama (2022). Figure 8 and Table S11 show the resulting translation of global carbon cycle models' land flux definitions to that of the NGHGIs (discussed in Section 3.2.2).

We also use gridded net land flux estimates from 16 atmospheric inversion systems (Table S4) to get an additional estimate of land-use fluxes on managed land for 2000-2025. The number of inversion systems providing estimates increases over this period. We apply a correction for riverine transport (see Supplement S.5.1.) and multiply the resulting values with the fraction of managed land in each grid cell for each inversion system. For this purpose, we use masks of managed land from Grassi et al. (2023) available for the years 1994, 2002, 2010, and 2016. We linearly interpolate the masks in time and replicate the 2016 mask in the years 2017-2025. Subsequently, we apply another correction for lateral transport due to international wood and crop trade from the Lateral Accounting of Transport in Terrestrial Ecosystems (LATTE) dataset version 6.1 (Ciais et al., 2026). As data for 2025 are not available, we replicate the 2024 value in 2025. The obtained inversion-based estimates of the net land flux in managed land are summed globally and compared to the LULUCF flux estimates from NGHGIs and the translated net E_{LUC} estimates.

Additionally, we use FAO estimates of CO_2 land fluxes (FAO, 2026b). FAO reports emissions from the net conversion between forest and agricultural land (proxy of deforestation) and removals on forest land based on

carbon stock changes (Tubiello et al., 2026) as well as emissions from peat drainage (Conchedda and Tubiello, 2020) and peat fires (Prosperi et al., 2020) based on IPCC Tier 1 emission factors. The FAO forest estimates are computed as carbon stock changes on a country's total forest area, based on FRA 2025 data for living biomass, litter, dead wood and soil carbon pools. Losses from harvested wood products are assumed to occur instantly and are part of the carbon stock change calculations.

S.2.5 Uncertainty assessment for E_{LUC}

Differences between the bookkeeping models and DGVMs originate from three main sources: different methodologies, different underlying land-use/land-cover datasets, and different processes represented (Table S1). We examine both the results from bookkeeping models and from DGVMs and use the resulting variations to characterise the uncertainty in E_{LUC}.

Despite the existing differences, the E_{LUC} estimate from the DGVM multi-model mean is consistent with the average of the emissions from the bookkeeping models (Table 5). However, there are substantial differences among individual DGVMs (standard deviation at ~0.3 GtC yr^{-1}; Table 5) and between the bookkeeping estimates (0.3 GtC yr^{-1} difference between lowest and highest net E_{LUC} estimate in 2016-2025). A factorial analysis of differences between BLUE and the bookkeeping model H&N2017 (Houghton & Nassikas, 2017), which was part of the bookkeeping ensemble in previous GCBs, attributed them particularly to differences in carbon densities between primary and secondary vegetation (Bastos et al., 2021). Earlier studies additionally showed the relevance of the different land-use forcing as applied (in updated versions) also in the current study (Gasser et al., 2020). Ganzenmüller et al. (2022) showed that E_{LUC} estimates from BLUE are substantially smaller when the model is driven by a high-resolution land-use dataset (HILDA+). They identified shifting cultivation and the way it is implemented in LUH2 as a main reason for this divergence. They further showed that a higher spatial resolution reduces the estimates of both gross emissions and gross removals because successive transitions are not adequately represented at coarser resolution, which has the effect that—despite capturing the same extent of transition areas—overall less area remains pristine at the coarser compared to the higher resolution.

The uncertainty in E_{LUC} of ±0.7 GtC yr^{-1} reflects our best value judgement that there is at least 68% chance (±1σ) that the true land-use change emissions lie within the given range, for the range of processes considered here. Prior to the year 1959, the uncertainty in E_{LUC} is taken from the standard deviation of the DGVMs. We assign low confidence to the annual estimates of E_{LUC} because of the inconsistencies among estimates and because of the difficulties to quantify some of the processes with DGVMs.

S.3 Methodology Ocean CO_2 sink S_{OCEAN}

S.3.1 Observation-based estimates

***f*CO_2-products** - We use ten estimates of the ocean CO_2 sink and its variability based on surface ocean fCO_2 maps obtained by the interpolation of surface ocean fCO_2 measurements. Eight of the methods cover a period from 1990 onwards due to severe restriction in data availability prior to 1990 (Figure 11), whereas two span the

period from 1957 and 1959 onwards. These estimates differ in many respects: they use different maps of surface fCO_2, different atmospheric CO_2 concentrations, different wind products and different gas-exchange formulations as specified in Table S3. We refer to them as fCO_2-products. The methods include a data-driven diagnostic method combined with a multi-linear regression approach to extend back to 1957 (Rödenbeck et al., 2022; referred to here as Jena-MLS), six neural network models (Landschützer et al., 2014; referred to as VLIZ-SOMFFN; Chau et al., 2022; Copernicus Marine Environment Monitoring Service, referred to here as CMEMS-LSCE-FFNN; Zeng et al., 2022; referred to as NIES-ML3;, Ford et al., 2024; referred to as UExP-FNN-UGregor et al., 2024; referred to as OceanSODA-ETHZv2, Wanninkhof et al 2025a, referred to as AOML-ET), a multi-linear regression method (Iida et al., 2021; referred to as JMA-MLR), and two methods that relates the fCO_2 observations either between GOBMs and SOCAT to environmental predictors using the extreme gradient boosting method extending back to 1959 (Gloege et al., 2022, referred to as LDEO-HTP)) or between CMIP6 models and SOCAT observations via a vision transformer method (Zhang et al 2025, referred to as SJTU-AVIT). The ensemble mean of the fCO_2-based flux estimates is calculated from these ten mapping methods. In v2026, 3 fCO_2 products (JMA-MLR,UExP-FNN-U and AOML-ET) adjust the SOCAT fCO_2 to account for differences in temperature between the depth of the ship intake and the relevant depth right near the surface using the dataset provided by Ford et al. (2026a,b). Furthermore, UExP-FNN-U includes an additional adjustment to account for the cool surface skin temperature effect in the air-sea CO_2 flux.
Following the approach of Friedlingstein et al. (2025b), we add 0.18 PgC yr^{-1} (multiplied by 7/10 as 3 products already include the cool skin/warm layer temperature effect). This correction is only done on the fCO_2-products average, at the global scale, for the estimate of S_{OCEAN}.

The impact of the cool skin and warm layer effect on air-sea CO_2 flux is based on established understanding of temperature gradients (as discussed by Goddijn-Murphy et al., 2015 and Woolf et al., 2016), and laboratory observations (Jähne and Haussecker, 1998; Jähne, 2019), however in situ field observational evidence is still sparse (Dong et al., 2022, Ford et al., 2024). While the cool skin and warm ocean layers are mechanistically well understood, temperature differences between the ship inlet and the sea surface microlayer due to variable sampling depth as well as potential artificial warm biases also have been suggested in the literature (Dong et al., 2022, Watson et al., 2020, Ford et al 2026a,b). These are, however, not considered in the above correction factor due to their uncertainty.
Historically, fCO_2-products do not cover the entire ocean due to missing coastal oceans and sea-ice cover, however, coverage has significantly improved in recent years. The CO_2 flux from the fCO_2-based products is already at or above 99% coverage of the ice-free ocean surface area in several products this year (UExP-FNN-U, JMA-MLR, VLIZ-SOMFFN, Jena-MLS, OceanSODA-ETHZv2, CMEMS-LSCE-FFNN, either due to complete coverage or a posteriori filling). The products that remained below 99% coverage of the ice-free ocean (NIES-ML3, LDEO-HPD, SJTU-AVIT) were scaled by the following procedure.
Since v2022 of the GCB we now scale fluxes globally and regionally (North, Tropics, South) to match the ice-free area (using the HadISST sea surface temperature and sea ice cover; Rayner et al., 2003):

$$FCO_2^{reg-scaled} = \frac{A_{(1-ice)}^{region}}{A_{FCO_2}^{region}} \cdot FCO_2^{region} \quad \text{(S4)}$$

In Eq. (S4), A represents area, (1 – ice) represents the ice-free ocean, A_{FCO2}^{region} represents the coverage of the fCO_2-product for a region, and FCO_2^{region} is the integrated flux for a region.

For the regional estimates of S_{OCEAN} based on the fCO_2-products, we subtract the preindustrial mean state from the fCO_2-products. For this, we use the preindustrial mean flux from the GOBMs' simulation B averaged over 1958-2025 from six models that do not account for riverine outgassing, i.e. their simulation B represents the natural steady state fluxes ($F_{nat,ss}$) and that have a simulation B CO_2 flux within ± 0.2 GtC yr^{-1} (NEMO-PlankTOM12, NorESM-OCv1.2, FESOM-2.7-REcoM3.1, CESM-ETHZ, MRI-ESM2-4, ACCESS). The regional preindustrial mean fluxes are: 0.71±0.14 GtC yr^{-1} (North), -1.07±0.25 GtC yr^{-1} (Tropics), 0.38±0.22 GtC yr^{-1} (South), 0.05±0.10 GtC yr^{-1} (Atlantic), -0.30±0.18 GtC yr^{-1} (Pacific), 0.02±0.14 GtC yr^{-1} (Indian), 0.07±0.01 GtC yr^{-1} (Arctic), 0.15±0.22 GtC yr^{-1} (Southern Ocean, Figure S4).

SOCAT - The measurements underlying the surface fCO_2-products are from the Surface Ocean CO_2 Atlas version 2026 (SOCAT v2026; Bakker et al., 2026), which is an update of version 3 (Bakker et al., 2016) and the subsequent annual updates used in previous versions of the global carbon budget. SOCAT updated its quality control cookbook for SOCATv2025 and v2026 (Gkritzalis et al., 2024), partly in response to the results of the 2021 fCO_2 intercomparison experiment (Steinhoff et al., 2025). These changes have been implemented going forwards, i.e., for new and updated data submissions to SOCATv2025 and v2026. Two important changes in the cookbook are: Membrane-based fCO_2 sensor data can at best receive a flag of E (uncertainty of less than 10 µatm), such that new and updated membrane-based data sets are not part of the synthesis and gridded SOCAT products used for the global carbon budget. Complete metadata is now required for all new and updated data sets (except for historic data sets). SOCAT v2026 has an additional 2.6 million fCO_2 measurements with an estimated accuracy of better than 5 µatm relative to v2025. Of these, 2.1 million are from 2025 in a total of 298 data sets (Table S7), while the largest addition from earlier years is from 2024 with 75data sets new to SOCAT. No data sets that were included in earlier SOCAT versions have been suspended or excluded from SOCATv2026. For 2024, the one but final year in SOCATv2026 (with more data sets than the final year as a result of delays in data submission), there are a total of 279 data sets with measurements in the Northern hemisphere, while there are 106 data sets from the Southern hemisphere. For the Southern Ocean, there are only 16 data sets from 2024 south of 50°S, and none from Austral winter (June-August). The coverage of monthly gridded SOCAT observations in 2024 is only about 65% of that in 2016 (Fig. 11), mainly as a result of a large reduction in sampling in the Northern hemisphere (from 391 to 279 data sets), while the Southern hemisphere data collection effort showed little change (from 109 to 106 data sets). Each of the data-based estimates uses a different method to map the SOCAT v2026 data to the global ocean.

Prior to 1959 - We further use results from two diagnostic ocean models, Khatiwala et al. (2013) and DeVries (2014), to estimate the anthropogenic carbon accumulated in the ocean prior to 1959. The two approaches assume constant ocean circulation and biological fluxes, with S_{OCEAN} estimated as a response to the change in atmospheric CO_2 concentration calibrated to observations. The uncertainty in cumulative uptake of ±20 GtC (converted to ±1σ) is taken directly from the IPCC's review of the literature (Rhein et al., 2013), or about ±30% for the annual values (Khatiwala et al., 2009).

Additional data - We use the observational constraints assessed by IPCC of a mean ocean CO_2 sink of 2.2 ± 0.7 GtC yr^{-1} for the 1990s (90% confidence interval; Ciais et al., 2013) to verify that the GOBMs and fCO_2-products provide a realistic assessment of S_{OCEAN}. This is based on indirect observations with seven different methodologies and their uncertainties, and further using three of these methods that are deemed most reliable for the assessment of this quantity (Denman et al., 2007; Ciais et al., 2013). The observation-based estimates use the ocean/land CO_2 sink partitioning from observed atmospheric CO_2 and O_2/N_2 concentration trends (Manning and Keeling, 2006; Keeling and Manning, 2014), an oceanic inversion method constrained by ocean biogeochemistry data (Mikaloff Fletcher et al., 2006), and a method based on penetration time scale for chlorofluorocarbons (McNeil et al., 2003). The IPCC estimate of 2.2 GtC yr^{-1} for the 1990s is consistent with a range of methods (Wanninkhof et al., 2013). We refrain from using the IPCC estimates for the 2000s (2.3 ± 0.7 GtC yr^{-1}), and the period 2002-2011 (2.4 ± 0.7 GtC yr^{-1}, Ciais et al., 2013) as these are based on trends derived mainly from models and one data-product (Ciais et al., 2013). Additional constraints summarised in AR6 (Canadell et al., 2021) are the interior ocean anthropogenic carbon change (Gruber et al., 2019) and ocean sink estimate from atmospheric CO_2 and O_2/N_2 (Tohjima et al., 2019), of which we already use updated data sets for model evaluation and discussion, respectively.

S.3.2 Global Ocean Biogeochemistry Models (GOBMs)

The ocean CO_2 sink for 1959-2024 is estimated using ten GOBMs (Table S2). The GOBMs represent the physical, chemical, and biological processes that influence the surface ocean concentration of CO_2 and thus the air-sea CO_2 flux. The GOBMs are forced by meteorological reanalysis and atmospheric CO_2 concentration data available for the entire time period. They mostly differ in the source of the atmospheric forcing data (meteorological reanalysis), spin up strategies, and in their horizontal and vertical resolutions (Table S2). All GOBMs except one (CESM-ETHZ) do not include the effects of anthropogenic changes in nutrient supply (Duce et al., 2008). They also do not include the perturbation associated with changes in riverine organic carbon (see Section 2.10 and Supplement S.6.3). Four sets of simulations were performed with each of the GOBMs. Simulation A applied historical changes in climate and atmospheric CO_2 concentration. Simulation B is a control simulation with constant atmospheric forcing (normal year or repeated year forcing) and constant pre-industrial atmospheric CO_2 concentration. Simulation C is forced with historical changes in atmospheric CO_2 concentration, but repeated year or normal year atmospheric climate forcing. Simulation D is forced by historical changes in climate and constant pre-industrial atmospheric CO_2 concentration.

To derive S_{OCEAN} from the model simulations, we subtracted a linear fit to the annual time series of the control simulation B from the annual time series of simulation A. Assuming that drift and bias are the same in simulations A and B, we thereby correct for any model drift. Further, this difference also removes the natural steady state flux (assumed to be 0 GtC yr^{-1} globally without rivers), which is often a major source of biases. Note, however, that Gürses et al. (2023) questioned the assumption of comparable bias and drift in simulations A and B as they compared two versions of FESOM-REcoM, and found a very similar air-sea CO_2 flux in simulation A despite a different bias as derived from simulation B. This approach works for all model set-ups, including CNRM, IPSL and Princeton, where simulation B was forced with variable historical climate changes

(looping over a certain repeated period for atmospheric forcing). This approach assures that the interannual variability is not removed from CNRM, IPSL and Princeton simulation A. The absolute correction for bias and drift per model in the 1990s varied between <0.01 GtC yr^{-1} and 0.47 GtC yr^{-1}, with four models having positive biases, five having negative biases and one model has essentially no bias (NorESM $\leq$ 0.02 GtC yr^{-1}). Three models use riverine inputs that are not balanced by burial (Table S2) and these three models simulate outgassing in simulation B. By subtracting a linear fit of simulation B, also the ocean carbon sink of these models follows the definition of S_{OCEAN}. This correction increases the model mean ocean carbon sink by 0.04 GtC yr^{-1} in the 1990s.

The ocean models cover 99% to 101% of the total ocean area, so that area-scaling is not necessary.

Finally, we conceptually keep the scaling factor as proposed in Friedlingstein et al. (2025b) to account for the known biases by the GOBMs (section 2.5 and Friedlingstein et al., 2025b). However, we now base the value of the scaling factor on new quantitative process-based evaluation of the current GOBM ensemble, where we target the previously identified potential causes for an underestimation of the sink, namely biases in ocean carbon transport and mixing from the surface mixed layer to the ocean interior (Goris et al., 2018, Terhaar et al., 2021, Bourgeois et al., 2022, Terhaar et al., 2022), and biases in the chemical buffer capacity (Revelle factor) of the ocean (Vaittinada Ayar et al., 2022; Terhaar et al., 2022) (see next section S.3.3). Based on this analysis, we set the scaling factor for this year's GOBM ensemble to 1.0 (0% correction). This correction is only done on the GOBMs average, at the global scale, for the estimate of S_{OCEAN}.

S.3.3 GOBM evaluation

IPCC estimate - The ocean CO_2 sink for all GOBMs and the ensemble mean falls within 90% confidence of the observed range, or 1.5 to 2.9 GtC yr^{-1} for the 1990s (Ciais et al., 2013) before and after subtracting simulation B.

International Ocean Model Benchmarking - We evaluate the GOBMs using the IOMB framework (Collier et al., 2018, Fu et al., 2022). Building upon the benchmarking principles established by these studies, IOMB provides a systematic approach for assessing model performance against a range of observational datasets. Model skill is quantified using several statistical metrics, including bias, root mean square error (RMSE), annual cycle phase, and spatial distribution. These metrics are combined into an overall performance score (refer to equation 7 in Fu et al., 2022), which enables objective comparison across models. The IOMB framework has been further expanded and refined to address uncertainties in the estimation of the ocean carbon sink (IOMB-GCBv1).

For GCB2026, the benchmarking framework has been extended to include additional diagnostics relevant to the evaluation of ocean carbon uptake and its physical and carbonate system controls for the surface and subsurface ocean. In this updated version of IOMBv3-GCBv1, several new diagnostics were introduced, namely anthropogenic carbon inventories and tracer inventories of chlorofluorocarbons (CFC11, CFC12) and sulfur hexafluoride (SF6). In addition, vertical gradient diagnostics of upper and subsurface ocean variables are also included to assess the model representation of vertical structure of the ocean. Previously introduced diagnostics include the Revelle factor, Southern Ocean subpolar seasonally stratified biome (SPSS) surface salinity, Southern Ocean stratification index, Atlantic Meridional Overturning Circulation (AMOC), and CO_2 fugacity.

These metrics broaden the system's ability to evaluate model skill in reproducing critical physical and biogeochemical processes that influence the global ocean carbon sink. For the time-series analysis the overall model score is computed as a combination of the bias score and the Taylor score (depends on the normalized standard deviation and correlation). The final benchmark visualization presents Z-score normalized results, enabling fair comparison of model performance relative to each other across multiple variables and metrics. Figure S5 illustrates the evaluation results from IOMBv3-GCBv1, where key variables of interest are assessed against state-of-the-art observational datasets. The model climatology for the period 2000–2025 is compared with corresponding observational climatologies to evaluate model performance in simulating upper-ocean physics and biogeochemistry.

To assess upper-ocean physical processes, the variables sea surface temperature (SST), sea surface salinity (SSS), mixed layer depth (MLD), Southern Ocean stratification index (SO-SI), Southern Ocean SPSS biome salinity (SO-SPSS-SSS), Atlantic Meridional Overturning Circulation (AMOC) and the vertical gradients of temperature and salinity for upper (0-300 m) and subsurface (300-800 m) were analyzed. For temperature and salinity, individual performance scores are computed relative to WOA2023 (20222-2022, Locarnini et al., 2023, Reagan et al., 2023), GLODAPv2-2023 (2000-2021, Lauvset et al., 2024) and UExP-FNN-U v2026-pre1 (2000-2025, Ford et al., 2026c) datasets, and an overall score is derived by combining the evaluation against these reference datasets. The mixed layer depth, a key indicator of upper and interior ocean exchange, is evaluated using multiple observational products, including Sallée et al. (2021) and de Boyer Montégut (2023). The RAPID 26°N AMOC observational record (2005– 2023) is used to assess the modeled AMOC strength (Moat et al., 2025). The EN4.2.2 dataset (2005–2025, Good et al., 2013) provides the basis for evaluating both the Southern Ocean stratification index and SPSS biome salinity. In addition, CFC11, CFC12 and SF6 inventories are evaluated against OCIM-48L datasets (DeVries, 2022).

To evaluate carbonate chemistry, model-simulated surface total alkalinity (TALK) and dissolved inorganic carbon (DIC) are compared against GLODAPv2-2023 observations. For the Revelle factor, we use GLODAPv2-2023 (derived using PyCO2SYS v1.8 package, Humphreys et al., 2022) and the OceanSODA-ETHZ-v2023 observation-based data set (Gregor and Gruber, 2021). In addition, the vertical profiles of DIC and TALK for upper (0-300 m) and subsurface (300-800 m) were evaluated using GLODAP observations using vertical gradient analysis in the IOMB-GCBv1. Finally, CO_2 fugacity from the models is compared against SOCATv2026 (Bakker et al., 2026). For benchmarking the changes in oceanic inventory of anthropogenic carbon (dCant), we used observation-based estimates covering different time periods. For the period 1994–2007, we used the estimates of Gruber et al. (2019), derived from repeat hydrographic observations using the extended multiple linear regression (eMLR(C*)) method (Clement and Gruber, 2018), and the OCIM-based estimates of DeVries (2014). The OCIMv2014 were derived using a global Ocean Circulation Inverse Model (OCIM) constrained by observations of potential temperature, salinity, radiocarbon, and chlorofluorocarbon-11 (CFC-11). In addition, we used the estimates based on eMLR (C*) regression method of Müller et al. (2023) for 1994–2004 and 2004–2014 to benchmark anthropogenic carbon inventory changes over these respective periods. These comparisons help for consistent benchmarking among independent estimates of oceanic anthropogenic carbon storage across overlapping and consecutive time intervals.

Transient tracers - We evaluate the simulation of uptake and storage of transient tracers (CFC11, CFC12, SF6) in the GOBMs. For the model simulations, we use the protocol of Orr et al. (2017) and force the models with hemispheric atmospheric concentrations. These data are taken from Bullister et al. (2017, updated) for the period 1921-2022. Linear trends were applied to approximate the data for 2023-2025. The simulated CFC11, CFC12 and SF6 inventories in the ocean of simulation A are evaluated against the observation-derived global CFC11 inventory for the year 1994 ($5.5 \pm 1.2 \times 10^8$ moles, Willey et al., 2004, Matsumoto et al., 2004). As a second evaluation dataset, the full time-series was also compared to the simulated inventory of OCIM that assimilates ocean CFC11, CFC12 and SF6 observations to derive an optimized mean state circulation (DeVries, 2022). OCIM performs constant climate simulations ("simulation C"), so that any climate-induced changes in the tracer inventories would not be accounted for. These differences are acknowledged, available GOBM simulations of transient tracer simulations suggest that the differences in inventories between simulations A and C are less than 4.2%.

Emergent constraint - We apply the multi-predictor emergent constraint of Terhaar et al. (2022), with the uncertainty estimate of Terhaar et al. (2026), to the ten GOBMs of GCB2026. The target is S_{OCEAN} estimated from the GOBMs averaged over 2016-2025. The analysis is repeated for each decade since 1960, for 1990-2025 (Table S13), and for each individual year (Figure S7). Three predictors are calculated from simulation A of each model and compared with observation-based estimates over the periods for which observations are available.

(i) The surface salinity averaged over the inter-frontal region of the Southern Ocean between the Subtropical Front and the Polar Front (Terhaar et al., 2021), 2005-2022. The observed value of 34.04 ± 0.01 psu is the mean of the World Ocean Atlas 2023 (Reagan et al., 2024; Locarnini et al., 2024), EN4 (Good et al., 2013) and IAP (Cheng et al., 2020, 2024). The uncertainty is estimated as in Terhaar et al. (2026) and combines the spread across the three products ($\pm$ 0.002 psu) with their sampling uncertainties.

(ii) The strength of the AMOC at 26.5°N, 2005-2023. The observed value of 16.9 ± 0.8 Sv comes from the RAPID array (Cunningham et al., 2007; McCarthy et al., 2015; Moat et al., 2025), with an uncertainty that combines sampling and measurement errors (Terhaar et al., 2026).

(iii) The global mean surface ocean carbon uptake capacity, 1997-2007. Because the observation-based products do not cover the entire ocean, it is computed only over grid cells where all models and all four products provide data. The observed value of 0.546 ± 0.003 mmol m^{-3} ppm^{-1} is the mean of the gridded GLODAPv2 (Lauvset et al., 2016) and three fCO_2-based products: OceanSODA-ETHZ-v2023 (Gregor and Gruber, 2021), and the RECCAP2 versions of CMEMS-LSCE-FFNN (v20210709; Chau et al., 2022) and JMA-MLR (v20211208; Iida et al., 2021). The uncertainty is half the range across the four products.

Across the models, the simulated sink is regressed on the three predictors with ordinary least squares. The constrained sink is the value of this regression at the observed predictor values. Following Terhaar et al. (2026), its uncertainty combines two independent terms in quadrature. The first is the observational uncertainty of the predictors, propagated through the regression coefficients. The second is the prediction interval of the regression at the observed predictor

values, which uses the unbiased residual standard error ($N - p - 1$ degrees of freedom) and a leverage term that increases the further the observations lie from the model ensemble. This is more conservative than the residual standard deviation used in Terhaar et al. (2022). The unconstrained estimate is the multi-model mean ± one standard deviation. For 2016–2025, the regression explains 70% of the spread between models ($R^2 = 0.70$).

The constrained estimate is robust to the choice of models. Leaving out any single model changes the 2016–2025 estimate by between −0.13 and +0.04 GtC yr^{-1}. The largest change occurs when NorESM-OC1.2, the model with the strongest AMOC, is removed, which indicates that the AMOC contribution to the constraint relies mainly on this model. While leaving out a single model does not change the result beyond its uncertainty, one model is an actual outlier. To test whether individual models deviate from the relationship, each model was excluded from the regression in turn, and its sink was predicted from the remaining nine. The difference between simulated and predicted sink, divided by its standard error, follows a Student's t distribution with five degrees of freedom. ACCESS is the only model that deviates significantly: it takes up 0.53 GtC yr^{-1} (about 20%) more carbon than predicted from the other nine models for 2016–2025 ($t = 4.5$, $p = 0.007$), and between 4.1 and 8.5 in all other periods since 1990, while no other model exceeds $|t| = 1.5$ in these periods. Half of the excess uptake of ACCESS (0.27 of 0.56 GtC yr^{-1}, based on the gridded fluxes) occurs north of 30°N, the only region where the deviation is significant. In the North Atlantic, ACCESS mixes 265×10^{12} m^3 of water below 1000 m, compared with $15 \pm 35 \times 10^{12}$ m^3 expected from its AMOC based on the other nine models, and $1.5 \pm 0.6 \times 10^{12}$ m^3 in EN4 for 2005–2024, using the same mixed-layer criterion as for the models.

Additional evaluation - We further report mean values of process-based metrics that are related to ocean carbon uptake that are now also mostly covered by IOMB or the emergent constraint (Table S11). These are the Atlantic Meridional Overturning Circulation (Goris et al., 2018, Terhaar et al., 2022, 2024), the Southern Ocean sea surface salinity (Terhaar et al., 2021, 2022, 2024, Hauck et al., 2023b), the Southern Ocean stratification index (Bourgeois et al., 2022) and the surface ocean Revelle factor (Terhaar et al., 2022, 2024).

The Atlantic Meridional Overturning Circulation from the GOBMs is here defined as the maximum of the Atlantic meridional overturning streamfunction at 26.5°N, below 500 m. This is compared to data from the RAPID array at 26.5°N (Moat et al., 2025). The uncertainty of 0.8 Sv was again taken from Terhaar et al.,

2026). We use the years 2005-2023, which are all complete calendar years available from the RAPID data set, and report the temporal standard deviation over that period.

The Southern Ocean sea surface salinity is reported for the subpolar seasonally stratified biome (SPSS) and for the area covering both the SPSS and subtropical seasonally stratified (STSS) biomes. Biome definitions are taken from Fay and McKinley (2014, as provided for the RECCAP2 project). The sea surface salinity was first used as an emergent constraint for the Southern Ocean CO_2 uptake with Earth System Models (Terhaar et al. 2021, 2022) using the interfrontal salinity between the polar and subtropical fronts with dynamic fronts. As the GOBMs are forced with reanalysis data, the fronts do not vary as much as in the ESMs, and thus the use of fixed biomes is justified (Hauck et al., 2023b, Terhaar et al., 2024). We use the time period 2005-2025. The observational sea surface salinity values are calculated from the EN4 data set (Good et al., 2013; using the objective analyses – Gouretski and Reseghetti (2010) XBT corrections and Gouretski and Cheng (2020) MBT corrections) with the aid of the Fay and McKinley (2014) mask.

The Southern Ocean stratification index is a simplified version of the metric used in Bourgeois et al. (2022). It is defined as the difference between in situ density at the surface and at 1000 m depth in the latitudinal band of 30°S to 55°S. Each model provider calculated this metric based on their native model mesh. We use the period of 2005-2025. The same metric was calculated from the EN4 data set mentioned above (Good et al., 2013).

Finally, the global surface ocean Revelle factor is reported. Monthly 1°x1° gridded fields were provided by the modelling groups, based on standard carbonate chemistry routines (e.g., mocsy, Orr & Epitalon, 2015; PyCO2SYS, Humphreys et al., 2022a,b). The observational metrics come from two sources, firstly the gridded GLODAP data set v2.2016 (Lauvset et al., 2016), which is a climatology centered around the year 2002. For comparison with GLODAP, the models were subsampled to GLODAP data coverage and to a comparable time window also centred around 2002 (1997-2007). Secondly, the OceanSODA_v2023 data set (Gregor and Gruber, 2021) was used, which has all input data available to calculate the surface ocean Revelle factor. OceanSODA covers a slightly smaller surface area (between 97.2% and 99.6% depending on the month) but provides data until 2022. The period 2005-2022 was used due to data availability, and the models and the OceanSODA dataset were subsampled monthly to the common available open ocean grid cells between all models and OceanSODA.

S3.4 fCO_2-product evaluation

To benchmark the performance of 9 fCO_2-products included this year, we compare the suite of 10 fCO_2 products to independent observations that have not been included in any training/regression step of the methods, i.e. direct fCO_2 measurements from the Surface Ocean CO_2 Atlas (Bakker et al., 2016) that received a quality flag E (uncertainty less than 10 µatm) and calculated fCO_2 from surface ocean measurements of dissolved inorganic carbon and total alkalinity with quality flag of at least 2 from the Global Ocean Data Analysis Project (GLODAP, Lauvset et al. 2024) of the top 10 meters, via the CO2sys carbonate system calculation software (Sharp et al., 2020), using the dissociation constants of Lueker et al. (2000). Additionally, we use temperature-corrected SOCAT flag E fCO_2 measurements (from Ford et al., 2026a,b) for comparisons with JMA-

MLR,UExP-FNN-U and AOML-ET for consistency. Both sets of measurements carry inherent larger uncertainty than the SOCAT measurements the fCO_2-products are based on, however, their independent nature and spatial extent allows us to further investigate regional biases in fCO_2-products.

Interestingly, Figure S8 reveals overall close to zero or negative biases in all products, with the exception of the GLODAP comparison in the region north of 30°N, highlighting a tendency of the fCO_2-products to underestimate the sea surface fugacity of the observations. We find the smallest errors in the Southern Hemisphere south of 30°S in all fCO_2-products, i.e. a region that has substantially less seasonal data coverage compared to the northern hemisphere and where we find the largest trend divergence between GOBMs and fCO_2-products (see main text and below). Overall, fCO_2 products perform better against calculated GLODAP measurements compared to SOCAT flag E data, but with biases within the expected measurement uncertainty (up to 10 µatm). There are only 4 exceptions where biases are beyond the expected uncertainty range of the measurements, i.e. in the Northern Hemisphere, where UExP-FNN-U (-26.03 µatm), Jena-MLS (20.68 µatm) and OceanSODA-ETHv2 (24.90 µatm) show larger biases and in the tropics where OceanSODA-ETHZv2 (10.03 µatm) falls just outside the 10 µatm range. Larger spreads, represented by the RMSE exist in the north compared to SOCAT flag E data in the same products that illustrated the largest bias (with RMSE exceeding 100 µatm), however, the impact on the resulting global bias and RMSE remains small due to the very limited number of measurements in this region, explaining the larger bias and local spread. The global comparison reveals a better agreement with GLODAP measurements (mean bias of -1.72 µatm) compared to SOCAT flag E data (mean of -6.25 µatm), however, for all products within the estimated measurement uncertainty.

This benchmarking exercise is broadly consistent with a recent study by McKinley et al (2026), that is built on an ensemble of 10 *f*CO2-products, of which 8 contributed to this year's GCB. The main difference is that this study focuses on 5 large scale biome regions instead of the regions defined here in the GCB2026. Additionally, the study by McKinley et al (2026) uses independent CO2 observations from the Lamont Doherty Earth Observatory (LDEO) database in addition to SOCAT flag E and GLODAP data used here. Despite these differences, global results are consistent with the benchmarking conducted here for the mean biases against all independent measurements combined (± 5µatm reported in McKinley et al 2026 compared to ± 4µatm here) and their root mean square errors (19-37µatm reported in McKinley et al 2026 compared to ± 19-41 µatm here)

Additionally, as part of the Surface Ocean CO2 mapping (SOCOM) program, method benchmarking experiments are conducted and many of them are underway. One already conducted experiment (Roobaert et al 2026) extends on the previously conducted benchmarking exercise presented in the GCB2024 and GCB2025. Using a set of 5 GOBM´s, namely CESM-ETHZ, FESOM2.1-REcoM, MRI-ESM2, IPSL and NorESM, that were submitted to the GCB2023 (Friedlingstein et al., 2023), Roobaert et al 2026 performed a model testbed experiment, following the approach of Hauck et al. (2023a). A total of 9 fCO_2-products conducted the benchmark test, of which 7 have submitted to this year's carbon budget (VLIZ-SOMFFN, NIES-ML3, Jena-MLS, OceanSODA-ETHZv2, JMA-MLR and UExP-FNN-U, CMEMS-LSCE-FFNNv2). The GOBMs serve as known truth and are subsampled according to the real-world observation tracks. The fCO_2-products then reconstruct the true model field, based on the subsampled information provided. Roobaert et al 2026 then compare mean biases and trends for the period 2001-2021, i.e. the period where we see the divergence between fCO_2-products and models. Results of Roobaert et al 2026 show that ensemble mean biases averaged over 2001-

2021 and across the 5 subsampled GOBMs are +0.09 µatm for the mean, with larger biases when individual methods are considered, ranging from -1.81 to +1.38 µatm, and -0.13µatm yr decade-1 for the trends. This results in an estimated mean trend bias of -0.04 Pg C yr-1 decade-1 (range -0.14 to +0.13 Pg C yr-1 decade-1). The numbers, however, indicate biases in the model testbed framework and are not representative for their true uncertainties that are e.g. derived from the benchmarking with independent data above.

S3.5 Uncertainty assessment for S_{OCEAN}

We quantify the 1-σ uncertainty around the mean ocean sink of anthropogenic CO_2 by combining random and systematic uncertainties for the GOBMs and fCO_2-products with a Gaussian mixture model. In this approach, GOBMs and products are treated as two separate estimates, each with its own biases and structural uncertainty, and S_{OCEAN} as an equally weighted mixture of two Gaussians. Its variance is

$$\sigma(S_{OCEAN}) = \mathrm{sqrt}(0.5 * (\sigma_GOBM^2 + \sigma_products^2) + 0.25 * (S_{OCEAN}_GOBM - S_{OCEAN}_products)^2) \quad (S5)$$

The first term in this equation is the average variance of the two estimates and the second term grows as the means of the GOBMs and fCO_2 products diverge. For each ensemble, a random and a systematic term are added in quadrature, for every year.

The random uncertainties are taken from the ensemble standard deviation for every year. We derive the GOBMs systematic uncertainty by the mean deviation from the observation-based carbon inventory changes (Müller et al., 2023; DeVries, 2022; Keppler et al. 2023) over the 1990s, 2000s and 2010s, reported in Section 3.6.5 (0.3 GtC yr^{-1}). For the fCO_2-products, we consider systematic uncertainties stemming from uncertainty in fCO_2 observations (0.2 GtC yr^{-1} , Takahashi et al., 2009; Wanninkhof et al., 2013), gas-transfer velocity (0.2 GtC yr^{-1} , Ho et al., 2011; Wanninkhof et al., 2013; Roobaert et al., 2018), wind product (0.1 GtC yr^{-1}, Fay et al., 2021), river flux adjustment (0.3 GtC yr^{-1}, Regnier et al., 2022, formally 2-σ uncertainty), and fCO_2 mapping (0.2 GtC yr^{-1}, Landschützer et al., 2014).

The resulting uncertainty terms for the decade 2016-2025 are σ(GOBM random): 0.30 PgC yr^{-1}, σ(GOBM structural): 0.33 PgC yr^{-1}, σ(GOBMs combined): 0.45 PgC yr^{-1}, σ(fCO_2 products random): 0.37 PgC yr^{-1}, σ(fCO_2 products structural): 0.47 PgC yr^{-1}, σ(fCO_2 products combined): 0.60 PgC yr^{-1}, resulting in the first term of Equation S5 (σ^2) to amount to 0.28 (PgC yr^{-1})^2 and the second term (σ^2) to amount to 0.13 (PgC yr^{-1})^2 with the square root of their sum resulting in 0.64 PgCyr^{-1}. In 2025 this number increases to 0.68 PgC yr^{-1} attributable to the larger standard deviation of the products in that year.

The uncertainty estimate for the fCO_2 products is comparable to a recent estimate by Ford et al. (2024), who estimate an uncertainty of 0.76 GtC yr^{-1} [range 0.60 to 0.85 Pg C yr^{-1}] based on propagating different sources of uncertainty in fCO_2-products.

We examine the consistency between the variability of the GOBMs and the fCO_2-products to assess confidence in S_{OCEAN}. Individual estimates (both GOBMs and fCO_2products) generally produce a higher ocean CO_2 sink during strong El Niño events. There is emerging agreement between GOBMs and fCO_2-products on the patterns of decadal variability of S_{OCEAN} with a global stagnation in the 1990s and an extra-tropical strengthening in the 2000s (McKinley et al., 2020, Hauck et al., 2020). More recently, a fast growth of the sink is simulated by both methods between 2001 and 2016, and a stagnation period since then. A stagnation or even decline of S_{OCEAN}

occurred during the triple La Niña years 2020-2023. The central estimates of the annual flux from the GOBMs and the fCO_2-products have a correlation r of 0.98 (1990-2025). The agreement between the models and the fCO_2-products reflects some consistency in their representation of underlying variability since there is little overlap in their methodology or use of observations.

S3.6 Observation-based estimates of carbon storage changes in the ocean interior

We rely on three observation-based methods to quantify temporal changes in dissolved inorganic carbon (DIC) in the ocean interior, differing in their underlying observations, gap-filling approach, temporal resolution and the type of carbon fluxes they resolve.

The extended multiple linear regression (eMLR) method (Müller et al., 2023) applied to the tracer C* builds on observations of DIC, total alkalinity, phosphate, oxygen and other physical and biogeochemical variables from GLODAPv2 (Lauvset et al., 2022) collected during repeat surveys. The method calculates a quasi-conservative tracer C*, separating biological from anthropogenic carbon variability, and fits regional multiple regressions of C* against temperature, salinity, oxygen, and nutrients for individual water masses separated along neutral density surfaces. Finally, these regional MLR regressions are applied to global climatological fields to map the decadal change in anthropogenic carbon as the differences between survey periods.

The Ocean Circulation Inverse Model (OCIM; DeVries, 2022, Table S2) uses an observation-constrained steady-state ocean circulation model that assimilates temperature, salinity, CFCs, and radiocarbon to reconstruct the large-scale transport field. An abiotic carbon cycle module is then forced with the evolving atmospheric pCO_2 (partial pressure of CO_2) to simulate air–sea CO_2 fluxes and interior carbon storage. Because biological and internal biogeochemical feedbacks are excluded, OCIM isolates the anthropogenic component of the ocean carbon sink.

The Mapped Observation-Based Oceanic DIC (MOBO-DIC; Keppler et al., 2023) approach employs a two-step approach of self-organizing maps and feed-forward neural networks trained on ship-based DIC measurements from GLODAPv2 and corresponding environmental predictors such as temperature, salinity, nutrients, oxygen for the upper ocean and atmospheric pCO_2. The trained models reconstruct monthly global ocean interior DIC fields at 1° resolution for 2004–2019. As MOBO-DIC is based on total DIC observations without separating the anthropogenic component, it resolves the combined anthropogenic plus natural DIC changes.

To facilitate the comparison of S_{OCEAN} estimates from GOBMs and fCO_2 products to an observation-based composite estimate for full decades, two of the individual ocean interior products need to be scaled in time and/or adjusted for missing carbon flux components. To scale eMLR(C*)-based estimates to full decades (1990s, 2000s, 2010s) reported in Table 6, the cumulative ocean carbon storage change over the original base periods (1994-2004-2014) was divided by the corresponding atmospheric CO_2 increase (NOAA/GML global mean CO_2) to obtain a sink efficiency (Pg C ppm^{-1}), following Müller et al. (2023). These efficiencies were then multiplied by the observed atmospheric CO_2 change over the closest target decade. While this scaling approach assumes proportionality between atmospheric CO_2 growth and oceanic CO_2 uptake, the observational

reconstructions themselves already suggest that the sink efficiency varies over time, which implies that the scaled ocean interior estimates do not perfectly match the corresponding GOBM estimates in time. OCIM and eMLR(C*) estimates were further adjusted for non-steady changes in natural DIC storage, obtained from the ensemble of GOBMs (Sim D - Sim B), and OCIM estimates were further adjusted for non-steady changes in anthropogenic DIC storage, obtained from the ensemble of GOBMs (Sim A - Sim D - Sim C + Sim B), to obtain estimates formally consistent with the definition of S_{OCEAN}. While the observation-based estimates of S_{OCEAN} obtained with this approach contain GOBM-derived carbon flux components, the actual comparison of GOBM- and observation-based ocean interior estimates is numerically identical, irrespective of whether the observation-based estimates are adjusted to match the definition of S_{OCEAN} or if the flux components that are resolved by each of the observation-based reconstructions was directly computed from the GOBMs. In Table 6, the mean and range are provided for all members of the ensemble of three ocean interior estimates (OCIM, eMLR(C*), MOBO-DIC) that cover the full reported decade.

S.4 Methodology Land CO_2 sink S_{LAND}

S.4.1 DGVM simulations

The DGVMs model runs were forced by either the merged monthly Climatic Research Unit gridded Terrestrial Series (CRU-TS) and 6-hourly Japanese Reanalysis for Three Quarters of a Century (JRA-3Q) data set (CRU-JRA) or by the monthly CRU-TS data set, both providing observation-based temperature, precipitation, and incoming surface radiation on a 0.5°x0.5° grid and updated to 2025 (Harris et al., 2014, 2020).

The combination of CRU-TS monthly data with 6-hourly forcing from JRA-3Q (Kobayashi et al., 2015) in CRU-JRA is performed with a methodology used in previous years (Viovy, 2016) adapted to the specifics of the JRA-3Q output. Introduced in GCB2021 (Friedlingstein et al., 2022a), incoming short-wave radiation fields take into account aerosol impacts and the division of total radiation into direct and diffuse components as summarised below.

The diffuse fraction dataset offers 6-hourly distributions of the diffuse fraction of surface shortwave fluxes over the period 1901-2025. Radiative transfer calculations are based on monthly-averaged distributions of tropospheric and stratospheric aerosol optical depth, and 6-hourly distributions of cloud fraction. Methods follow those described in the Methods section of Mercado et al. (2009), but with updated input datasets.

The time series of speciated tropospheric aerosol optical depth is taken from the historical and RCP8.5 simulations by the HadGEM2-ES climate model (Bellouin et al., 2011). To correct for biases in HadGEM2-ES, tropospheric aerosol optical depths are scaled over the whole period to match the global and monthly averages obtained over the period 2003-2020 by the CAMS Reanalysis of atmospheric composition (Inness et al., 2019), which assimilates satellite retrievals of aerosol optical depth.

The time series of stratospheric aerosol optical depth is taken from the by Sato et al. (1993) climatology, which has been updated to 2012. Years 2013-2020 are assumed to be background years so replicate the background year 2010. That assumption is supported by the Global Space-based Stratospheric Aerosol Climatology time series (1979-2016; Thomason et al., 2018). The time series of cloud fraction is obtained by scaling the 6-hourly distributions simulated in the Japanese Reanalysis (Kobayashi et al., 2015) to match the monthly-averaged cloud cover in the CRU TS v4.06 dataset (Harris et al., 2020). Surface radiative fluxes account for aerosol-radiation

interactions from both tropospheric and stratospheric aerosols, and for aerosol-cloud interactions from tropospheric aerosols, except mineral dust. Tropospheric aerosols are also assumed to exert interactions with clouds. The radiative effects of those aerosol-cloud interactions are assumed to scale with the radiative effects of aerosol-radiation interactions of tropospheric aerosols, using regional scaling factors derived from HadGEM2-ES. Diffuse fraction is assumed to be 1 in cloudy sky. Atmospheric constituents other than aerosols and clouds are set to a constant standard mid-latitude summer atmosphere, but their variations do not affect the diffuse fraction of surface shortwave fluxes.

In addition to the climate forcing, the DGVMs forcing also include the global atmospheric CO_2 time series, same as for the GOBMs and described in Section S.3.2 (Lan et al. (2023), the gridded land cover changes (see Supplement S.2.2), and the gridded nitrogen deposition and fertilisers (see Table S1 for specific models details).

Seven simulations are performed with the DGVMs; S4-S6 are new for GCB2026.

- Simulation 0 (S0) is a control simulation which uses fixed pre-industrial (year 1700) atmospheric CO_2 concentrations, cycles early 20th century (1901-1920) climate and applies a time-invariant pre-industrial land cover distribution, pre-industrial wood harvest rates and pre-industrial N inputs.
- Simulation 1 (S1) differs from S0 by applying historical changes in atmospheric CO_2 concentration and N deposition, while applying time invariant pre-industrial land cover distribution, pre-industrial wood harvest rates, and pre-industrial climate.
- Simulation 2 (S2) applies historical changes in atmospheric CO_2 concentration, N deposition, and climate, while applying time-invariant pre-industrial land cover distribution and pre-industrial wood harvest rates.
- Simulation 3 (S3) applies historical changes in atmospheric CO_2 concentration, N deposition, climate, and land cover distribution, wood harvest rates and N fertilizer.
- Simulation 4 (S4) applies historical changes in land cover distribution, wood harvest rates, and N fertilizer, while applying time invariant pre-industrial atmospheric CO_2 concentration, pre-industrial N deposition and pre-industrial climate.
- Simulation 5 (S5) applies historical changes in atmospheric CO_2 concentration, N deposition, and land cover distribution and wood harvest rates, and N fertilizer, while applying time invariant pre-industrial climate.
- Simulation 6 (S6) applies historical changes in climate, land cover distribution, wood harvest rates, and N fertilizer, while applying time invariant pre-industrial atmospheric CO_2 concentration and N deposition.

Simulation	CO2 / Ndep.	Climate	Land-Use / NFert.
S0	F	F	F
S1	T	F	F
S2	T	T	F
S3	T	T	T
S4	F	F	T
S5	T	F	T

S6	F	T	T

In previous budgets, SLAND was estimated from simulation S2, which uses time-invariant pre-industrial land cover. S2 therefore includes sinks (and sources) on land that has since been converted to other uses, such as forest that has been cleared for agriculture. In GCB2025, we corrected for these replaced sinks and sources (RSS) by combining per-area S2 fluxes on PFT level with the transient S3 land cover, using the subset of seven DGVMs that provided the required output (O'Sullivan et al. 2026). This correction relies on a small subset of the ensemble. It is also difficult to apply to models with explicit vegetation demography: forests in S2 do not have the age structure created by historical land use and land management, so they respond differently to environmental change than forests in S3. For GCB2026, we therefore introduce three new simulations (S4-S6), so that SLAND and its attribution to CO2 and climate are calculated only from simulations with transient land cover. The one term these simulations do not resolve, the environmental effect on land-use fluxes (δL), is taken from the bookkeeping models (see below).

New for GCB2026, S_{LAND} is calculated as:

$$S_{LAND} = S3 - (S4 - S0) + \delta L$$

where δL represents the transient environmental effects on E_{LUC} (Dorgeist et al. 2024), as estimated from bookkeeping models (see Supplement S.2.2). These effects arise because land-use change and land management generally cause larger CO2 emissions and removals under transient and present-day environmental conditions than under pre-industrial conditions, largely due to increased forest biomass and enhanced tree growth at higher atmospheric CO2 concentrations. δL is quantified by bookkeeping models as the difference in E_{LUC} of a simulation under transient and one under pre-industrial environmental conditions (CO2 and climate). δL has the E_{LUC} sign convention where a positive value is an emission from the land to the atmosphere. For 2016-2025, global SLAND from the new approach is very close to the GCB2025 RSS-based approach (both 2.5 GtC yr-1).

S3 is used to estimate the total land flux. We further separate S_{LAND} into contributions from CO_2 and N deposition (=S3-S6+δL) and climate (=S3-S5+S0). We do not attempt to calculate the individual contributions of CO_2 and climate on the δL term and for simplicity/visualisation in Figure 12 we add the δL term to the CO_2 effect (Figure 12a), although we recognise there also long-term climate change effects on carbon stocks that are subsequently impacted by land-use change.

S.4.2 DGVM evaluation

We apply three criteria for minimum DGVMs realism by including only those DGVMs with (1) steady state after spin up, (2) global net land flux ($S_{LAND} - E_{LUC}$) that is an atmosphere-to-land carbon flux over the 1990s ranging between -0.3 and 2.3 GtC yr^{-1}, within 90% confidence of constraints by global atmospheric and oceanic observations (Keeling and Manning, 2014; Wanninkhof et al., 2013), and (3) global E_{LUC} that is a carbon source

to the atmosphere over the 1990s, as already mentioned in Supplement S.2.2. All DGVMs meet these three criteria.

The International LAnd Model Benchmarking (ILAMB) system (Collier et al. 2018; version 2.7.2 (2024): https://github.com/rubisco-sfa/ILAMB/releases/tag/v2.7.2) is used to compare the 24 models (23 DGVMs and CARDAMOM) to observational benchmarks for a number of different variables related to the land surface: live biomass carbon, gross primary productivity (GPP), leaf area index (LAI), ecosystem respiration (heterotrophic + autotrophic), soil carbon, evapotranspiration, runoff, burned areas, fire CO_2 emissions, and soil respiration. Each row for each variable in Figure S10 is clickable in the full website version (https://gws-access.jasmin.ac.uk/public/landsurf_rdg/pmcguire/ILAMB_output_TRENDYv15/TRENDYv15_latest/) and gives access to geographic plots for such quantities as bias relative to observational benchmark, temporal RMSE from the observational benchmark, and difference in max month from the observational benchmark. The full website version also gives a spatial Taylor diagram for all the models, as well as time series comparisons of the regional mean time-series and the regional mean annual cycle.

Like in GCB2025, we include Biomass Carbon in the ILAMB analysis, wherein we add a time-dependent annual dataset, ESACCI6.0 (Santoro et al. 2024), for the years 2015-2022, and a time-dependent annual dataset XuSaatchi (Xu et al., 2021), for the years 2000-2019. This year, for Biomass Carbon, we also include GEDI_L4B (Dubayah et al., 2022) as a time-averaged dataset, for the dates April 2019 to March 2023. For the ESACCI dataset, the ESACCI6.0 dataset, the XuSaatchi dataset, and the GEDI_L4B dataset, we use an approximate, global, linearized, allometric root-to-shoot ratio (RSR) of 0.275 to convert above-ground biomass to total above-ground + below-ground biomass (multiplying by 1.0 + RSR).

In the ILAMB setup for TRENDYv13 (GCB2024), we added three extra variables (annual-averaged Burned Area, Fire Emissions, and Soil Respiration). In addition for TRENDY-GCB2025 the following changes are made:

1) Modified the Koven et al., (2017) analysis slightly for the Soil Carbon variable, when masking out arid regions;
2) Added annually-averaged observational data sets for GFED5.1 for both Burned Area and Fire Emissions (Chen et al. 2023);
3) Enabled a pre-existing ILAMB variable for Carbon Dioxide, which uses Net Biome Production (NBP) over land as an emulator for Carbon Dioxide that is subsequently transported by atmospheric circulation to the observation sites, as in Liptak et al. (2017).

The ILAMB setup for TRENDYv15 (GCB2026) has not been significantly changed from the ILAMB setup for TRENDYv14 (GCB2025), except for the addition of the GEDI_L4B variable for Biomass Carbon. The new variables in GCB2024/25 are assigned into the category, 'Ecosystem and Carbon Cycle Extended'. Variables in this category do not affect the overall scores for the category 'Ecosystem and Carbon Cycle'. For TRENDY-GCB2025, Burned Area from two models (EDv3 and SDGVM) were corrected in post-processing to mask out fuel limited regions (i.e. grid cells with no vegetation or with no carbon emissions due to fire). For TRENDY-

GCB2026, Burned Area for SDGVM is not included, and no post-processing was done for Burned Area for EDv3.

For TRENDY-GCB2026, we determined that the observational benchmark data sets for Soil Carbon (HWSD, Fischer et al., 2008, and NCSCDv2.2, Hugelius et al., 2013) are set for depths down to 1-meter. Three of our models (CLM6.0, E3SM, and LPJmL) previously reported Soil Carbon down to deeper depths, and they had poor ILAMB subscores for Soil Carbon. Therefore, for only these three models, we updated their model outputs to only be for depths down to 1-meter, and the Soil Carbon subscores for these models improved.

For TRENDY-GCB2026, for weighting the global sums, we have provided the fractional land-fractions for those models that do not use binary-only land-fractions. This affects the ILAMB global sums for those models, but the ILAMB relative scores are unaffected.

Like in TRENDY-GCB2025, a row for the total score is added to the ILAMB summary page, and this total score is called 'Hydrology and Carbon Cycles'. The total score is the weighted average of the 'Hydrology Cycle' (weight of 2, since there are 2 variables under Hydrology Cycle) and the 'Ecosystem and Carbon Cycle' (weight of 5 , since there are 5 variables under the Ecosystem and Carbon Cycle).

The TRENDY-GCB2025 version of the updated ILAMB version 2.7.2 GitHub code fork/branch is available at: https://github.com/mcguirepatr/ILAMB/tree/master

New to GCB2026, we use the ILAMB Carbon Dioxide emulation described above to evaluate the DGVM net land flux in more detail against atmospheric CO2 at 38 NOAA Global Monitoring Laboratory stations: 9 in the North (north of 30°N), 20 in the Tropics (30°S-30°N) and 9 in the South (south of 30°S). The emulation needs monthly NBP, so it is applied to the 21 DGVMs that provide monthly output; LPJ-GUESS and LPJmL are thus not included, as they calculate respiration on an annual timescale. In ILAMB, the land contribution to CO2 at each station is obtained by convolving each model's monthly NBP with precomputed atmospheric pulse-response functions. The fossil fuel and ocean contributions are removed from the observed records. The comparison covers 1983-2013. At each station, the seasonal cycle is the mean annual cycle. Interannual variability (IAV) is extracted with the NOAA CCGCRV curve-fitting filter (Thoning et al., 1989), as the smoothed record minus its long-term trend and harmonics. For each latitude band, we compute the root-mean-square error (RMSE) of the simulated seasonal cycle and IAV against the observations - and show the median across stations (Figure S11). Results suggest agreement across models for IAV with a wider spread across DGVMs and general poorer performance for the seasonal cycle at northern stations. For the northern stations, we also compute the trend in seasonal amplitude from a linear fit to annual amplitudes. We calculate the absolute difference from the observed trend and plot the median (and interquartile range) error across the stations (Figure S12).

S.4.3 Uncertainty assessment for S_{LAND}

For the uncertainty for S_{LAND}, we use the standard deviation of the annual CO_2 sink across the DGVMs combined with the δL uncertainty from the BKMs, averaging to ±0.7 GtC yr^{-1} for the period 1959 to 2025. We attach a medium confidence level to the annual land CO_2 sink and its uncertainty because the estimates from the residual budget and averaged DGVMs match well within their respective uncertainties (Table 5).

S.5 Methodology Atmospheric Inversions

S.5.1 Inversion System Simulations

Fourteen atmospheric inversions (details of each in Table S4) were used to infer the spatio-temporal distribution of the CO_2 flux exchanged between the atmosphere and the land or oceans. These inversions are based on Bayesian inversion principles with prior information on fluxes and their uncertainties. They use very similar sets of surface measurements of CO_2 time series (or subsets thereof) from various flask and in situ networks. Six inversion systems used surface observations, and eight inversion systems used satellite XCO_2 retrievals from GOSAT and/or OCO-2, of which three systems used a combination of satellite and surface observations. Each inversion system uses different methodologies and input data but is rooted in Bayesian inversion principles. These differences mainly concern the selection of atmospheric CO_2 data and prior fluxes, as well as the spatial resolution, assumed correlation structures, and mathematical approach of the models. Each system uses a different transport model, which was demonstrated to be a driving factor behind differences in atmospheric inversion-based flux estimates, and specifically their distribution across latitudinal bands (Gaubert et al., 2019; Schuh et al., 2019).

Most of the fourteen inversion systems prescribe similar global fossil fuel emissions for E_{FOS}; specifically, the GCP's Gridded Fossil Emissions Dataset version 2025.1 (GCP-GridFEDv2025.1; Jones et al., 2025), which is an update through 2024 of the first version of GCP-GridFED presented by Jones et al. (2021b) (Table S4). All GCP-GridFED versions scale gridded estimates of CO_2 emissions from EDGARv4.3.2 (Janssens-Maenhout et al., 2019) within national territories to match national emissions estimates provided by the GCP for the years 1959-2024, which are compiled following the methodology described in Supplement S.1. GCP-GridFEDv2025.1 adopts the seasonality of emissions (the monthly distribution of annual emissions) from the Carbon Monitor (Liu et al., 2020a,b; Dou et al., 2022) for Brazil, China, all EU27 countries, the United Kingdom, the USA and shipping and aviation bunker emissions. The seasonality present in Carbon Monitor is used directly for years 2019-2024, while for years 1959-2018 the average seasonality of 2019, and 2021 and 2022 are applied (avoiding the year 2020 during which emissions were most impacted by the COVID-19 pandemic). For all other countries, seasonality of emissions is taken from EDGAR (Janssens-Maenhout et al., 2019; Jones et al., 2023), with small annual correction to the seasonality present in 2010 based on heating or cooling degree days to account for the effects of inter-annual climate variability on the seasonality of emissions (Jones et al., 2021b).

Small remaining differences between regridding of the GridFED inputs, or the use of different fossil fuel emission priors are corrected for by scaling the resulting inverse fluxes to GridFEDv2025.1. The consistent use of E_{FOS} ensures a close alignment with the estimate of E_{FOS} used in this budget assessment, enhancing the comparability of the inversion-based estimate with the flux estimates deriving from DGVMs, GOBMs and fCO_2-based methods. The fossil fuel adjustment (including emissions from cement production and cement carbonation CO_2 sink) ensures that the estimated uptake of atmospheric CO_2 by the land and oceans was fully consistent within the inversion ensemble.

The land and ocean CO_2 fluxes from atmospheric inversions contain anthropogenic perturbation and natural pre-industrial CO_2 fluxes. On annual time scales, natural pre-industrial fluxes are primarily land CO_2 sinks and

ocean CO_2 sources corresponding to carbon taken up on land, transported by rivers from land to ocean, and outgassed by the ocean. These pre-industrial land CO_2 sinks are thus compensated over the globe by ocean CO_2 sources corresponding to the outgassing of riverine carbon inputs to the ocean, using the exact same numbers and distribution as described for the ocean in Section 2.5. To facilitate the comparison, we adjusted the inverse estimates of the land and ocean fluxes per latitude band with these numbers to produce historical perturbation CO_2 fluxes from inversions.

S.5.2 Inversion System Evaluation

All participating atmospheric inversions are checked for consistency with the annual global growth rate, as both are derived from the global surface network of atmospheric CO_2 observations. In this exercise, we use the conversion factor of 2.086 GtC ppm^{-1} to convert the inverted carbon fluxes to mole fractions, as suggested by Prather (2012). This number is specifically suited for the comparison to surface observations that do not respond uniformly, nor immediately, to each year's summed sources and sinks. This factor is therefore slightly smaller than the GCB conversion factor in Table 1 (2.142 GtC ppm^{-1}, Ballantyne et al., 2012). Overall, the inversions agree with the growth rate with biases between 0.003-0.04 ppm yr^{-1} (0.006-0.08 GtC yr^{-1}) for the period 2015-2024.

The atmospheric inversions are also evaluated using vertical profiles of atmospheric CO_2 concentrations (Figure S14). More than 50 aircraft programs over the globe, either regular programs or repeated surveys over at least 9 months (except on the SH), have been used to draw a robust picture of the system performance (with space-time data coverage irregular and denser in the 0-45°N latitude band; Table S9 and lower panel in Figure S14). The fourteen systems are compared to these independent aircraft CO_2 observations between 2 and 7 km above sea level between 2001 and 2024. Results are shown in Figure S14, where the inversions generally match the atmospheric mole fractions to within 0.6 ppm at all latitudes.

S.6 Methodology Earth System Models (ESMs)

The decadal prediction systems based on ESMs used here consist of three sets of simulations: (i) uninitialized freely evolving historical simulations (1850-2014); (ii) assimilation reconstruction incorporating observational data into the ESMsmodel (1960-2025); (iii) initialised prediction simulations for the 1981-2026 period, starting every year from initial states obtained from the above assimilation simulations. The assimilations are designed to reconstruct the actual evolution of the Earth system by assimilating essential fields from data products. The assimilations' states, which are expected to be close to observations, are used to start the initialised prediction simulations used for the current year (2026) global carbon budget. Similar initialised prediction simulations starting every year (Nov. 1st or Jan. 1st) over the 1981-2025 period (i.e., hindcasts) are also performed for predictive skill quantification and for bias correction. More details on the illustration of a decadal prediction system based on an ESM can refer to Figure 1 of Li et al. (2023).

Six ESMs, i.e., CanESM5 (Swart et al., 2019; Sospedra-Alfonso et al., 2021), EC-Earth3-CC (Döscher et al. 2021; Bilbao et al., 2021; Bernardello et al., 2024), IPSL-CM6A-CO2-LR (Boucher et al., 2020), MIROC-ES2L (Watanabe et al., 2020), MPI-ESM1-2-LR (Mauritsen et al., 2019; Li et al., 2023), and NorCPM-CC (Tjiputra et

al. 2020; Bethke et al. 2021) have performed 10-ensemble members of prediction simulations. Each ESM uses a different assimilation method and combination of data products incorporated into the model. More details on the models' configuration can be found in Table 4 and Supplement Table S5. The ESMs use external forcings from the Coupled Model Intercomparison Project Phase 6 (CMIP6) historical (1960-2014) plus SSP2-4.5 baseline and CovidMIP two-year blip scenario (2015-2026) (Eyring et al., 2016; Lamboll et al., 2021). The CO_2 emissions forcing from 2015-2024 are substituted by GCB-GridFED (v2025.0, Jones et al., 2025) to provide a consistent CO_2 forcing, the CO_2 emissions forcing for year 2025 is an extension with the same emission of the year 2024. The CO_2 emissions forcing for year 2026 use the 2025 emissions adding on top the increment of 2026 emissions in CMIP6 SSP2-4.5 scenario.

S.7 Atmospheric CO_2 time series

The 1750-2024 atmospheric CO_2 concentration times series is produced as follows.

Since January 1980, we use the CO_2 global growth rate reported by NOAA/GML (Lan et al., 2024). In the period March 1958-December 1979, we use bias-adjusted values of the global growth rate based on measurements of atmospheric CO_2 made by the Scripps Institution of Oceanography at the Mauna Loa Observatory, Hawaii (Keeling et al., 1976; full period of coverage 1758-2024). Bias adjustment of the Scripps data was performed in three sequential stages as follows:

- First, to correct for differences in the mean atmospheric concentration of CO_2 at Mauna Loa versus the globally averaged value, a constant of -0.231 ppm was added to all Scripps data to improve alignment of the "CO_2[trend]" values from the Scripps data with the "CO_2[trend]" values from the global NOAA data. The value of -0.231 ppm is the mean offset of "CO_2[trend]" at Mauna Loa from the global "CO_2[trend]" value during 1980-2000.
- Second, to correct for differences in the seasonality of atmospheric CO_2 concentrations at Mauna Loa versus globally, we shifted monthly anomalies between CO_2 concentration data and "trend" values backward in time by one month in the Scripps data. This specifically corrects for the fact that peaks/troughs in the climatology of "CO_2[monthly_observation] - CO_2[trend]" at Mauna Loa occur 1 month earlier than peaks/troughs in the climatology of "CO_2[monthly_observation] - CO_2[trend]" in the global data from NOAA. A one-month shift to the Scripps data was found to optimally align the climatologies of "CO_2[monthly_observation] - CO_2[trend]" in the Scripps and global data.
- Third, to correct for the greater amplitude of seasonal anomalies at Mauna Loa from Scripps than the global data from NOAA, we apply a monthly multiplier that dampens the magnitude of monthly anomalies from "trend" values in the Scripps data. The monthly multiplier reduces values of "CO_2[monthly_observation] - CO_2[trend]" in the Scripps data to more closely match values of "CO_2[monthly_observation] - CO_2[trend]" in the NOAA global data.

For the period Jan 1750 to February 1958, we use bias-adjusted values of the global growth rate based on measurements of atmospheric CO_2 from air trapped in ice at Law Dome (Joos and Spahni, 2008; full period of coverage 1750-2004). Bias adjustments were made to improve alignment with the post-1980 time series of data from Scripps and NOAA, and were performed in two sequential stages as follows:

- First, a constant of 0.973 was added to all data from Law Dome to improve alignment with the Scripps data (which had already been bias-corrected as described above). The constant of 0.973 is the mean offset of CO_2 annual values (annual mean in the case of the Scripps data) in the period 1958-1979.
- Second, the climatology of "CO_2[monthly_observation] - CO_2[trend]" from the period 1958-2000 was superimposed on the data from Law Dome (note that the 1958-2000 data includes both Scripps and NOAA data, combined as described above). To achieve this, a spline interpolation was fitted to downscale annual observations from CO_2 concentration from Law Dome to monthly values of "CO_2[trend]" and the climatological seasonality of "CO_2[monthly_observation] - CO_2[trend]" from 1958-2000) was then added to the interpolated values of "CO_2[trend]".

S.8 Processes not included in the global carbon budget

S.8.1 Contribution of anthropogenic CO and CH_4 to the global carbon budget

Equation (1) includes only partly the net input of CO_2 to the atmosphere from the chemical oxidation of reactive carbon-containing gases from sources other than the combustion of fossil fuels, such as: (1) cement process emissions, since these do not come from combustion of fossil fuels, (2) the oxidation of fossil fuels, (3) the assumption of immediate oxidation of vented methane in oil production. However, it omits any other anthropogenic carbon-containing gases that are eventually oxidised in the atmosphere, forming a diffuse source of CO_2, such as anthropogenic emissions of CO and CH_4. An attempt is made in this section to estimate their magnitude and identify the sources of uncertainty. Anthropogenic CO emissions are from incomplete fossil fuel and biofuel burning and deforestation fires. The main anthropogenic emissions of fossil CH_4 that matter for the global (anthropogenic) carbon budget are the fugitive emissions of coal, oil and gas sectors (see below). These emissions of CO and CH_4 contribute a net addition of fossil carbon to the atmosphere.

In our estimate of E_{FOS} we assumed (Section 2.1.1) that all the fuel burned is emitted as CO_2, thus CO anthropogenic emissions associated with incomplete fossil fuel combustion and its atmospheric oxidation into CO_2 within a few months are already counted implicitly in E_{FOS} and should not be counted twice (same for E_{LUC} and anthropogenic CO emissions by deforestation fires). The diffuse atmospheric source of CO_2 deriving from anthropogenic emissions of fossil CH_4 is not included in E_{FOS}. In reality, the diffuse source of CO_2 from CH_4 oxidation contributes to the annual CO_2 growth. Emissions of fossil CH_4 represent 30% of total anthropogenic CH_4 emissions (Saunois et al. 2020; their top-down estimate is used because it is consistent with the observed CH_4 growth rate), that is 0.083 GtC yr^{-1} for the decade 2008-2017. Assuming steady state, an amount equal to this fossil CH_4 emission is all converted to CO_2 by OH oxidation, and thus explain 0.083 GtC yr^{-1} of the global CO_2 growth rate with an uncertainty range of 0.061 to 0.098 GtC yr^{-1} taken from the min-max of top-down estimates in Saunois et al. (2020). If this min-max range is assumed to be 2 σ because Saunois et al. (2020) did not account for the internal uncertainty of their minimum and maximum top-down estimates, it translates into a 1-σ uncertainty of 0.019 GtC yr^{-1}.

Other anthropogenic changes in the sources of CO and CH_4 from wildfires, vegetation biomass, wetlands, ruminants, or permafrost changes are similarly assumed to have a small effect on the CO_2 growth rate. The CH_4 and CO emissions and sinks are published and analysed separately in the Global Methane Budget and Global

Carbon Monoxide Budget publications, which follow a similar approach to that presented here (Saunois et al., 2020; Zheng et al., 2019).

S.8.2 Contribution of other carbonates to CO_2 emissions

Although we do account for cement carbonation (a carbon sink), the contribution of emissions of fossil carbonates (carbon sources) other than cement production is not systematically included in estimates of $E_{FOS,}$ except for Annex I countries and lime production in China (Andrew and Peters, 2025). The missing processes include CO_2 emissions associated with the calcination of lime and limestone outside of cement production. Carbonates are also used in various industries, including in iron and steel manufacture and in agriculture. They are found naturally in some coals. CO_2 emissions from fossil carbonates other than cement not included in our dataset are estimated to amount to less than 0.5% of E_{FOS} (estimated based on Crippa et al., 2019).

S.8.3 Anthropogenic carbon fluxes in the land-to-ocean aquatic continuum

The approach used to determine the global carbon budget refers to the mean, variations, and trends in the perturbation of CO_2 in the atmosphere, referenced to the pre-industrial era. Carbon is continuously displaced from the land to the ocean through the land-ocean aquatic continuum (LOAC) comprising freshwaters, estuaries, and coastal areas (Bauer et al., 2013; Regnier et al., 2013). A substantial fraction of this lateral carbon flux is entirely 'natural' and is thus a steady state component of the pre-industrial carbon cycle. We account for this pre-industrial flux where appropriate in our study (see Supplement S.3). However, changes in environmental conditions and land-use change have caused an increase in the lateral transport of carbon into the LOAC – a perturbation that is relevant for the global carbon budget presented here.

The results of the analysis of Regnier et al. (2013) can be summarised in two points of relevance for the anthropogenic CO_2 budget. First, the anthropogenic perturbation of the LOAC has increased the organic carbon export from terrestrial ecosystems to the hydrosphere by as much as 1.0 ± 0.5 GtC yr^{-1} since pre-industrial times, mainly owing to enhanced carbon export from soils. Second, this exported anthropogenic carbon is partly respired through the LOAC, partly sequestered in sediments along the LOAC and to a lesser extent, transferred to the open ocean where it may accumulate or be outgassed. The anthropogenic CO_2 outgassing from the LOAC was recently estimated at 0.34 ± 0.26 GtC yr^{-1} (Regnier et al., 2022; Tian et al., 2023), a significant fraction originating from the lateral displacement of CO_2 produced by soil heterotrophic respiration to the aquatic system. The inclusion of LOAC related anthropogenic CO_2 fluxes should affect estimates of S_{LAND} and S_{OCEAN} in Eq. (1) but does not affect the other terms. The GOBMs and DGVMs used in the global carbon budget do not include a representation of the anthropogenic perturbation of LOAC CO_2 fluxes. Here we apply a posteriori correction of -0.07 GtC yr^{-1} to the S_{LAND} estimate as assessed in Friedlingstein et al. (2025b).

1284 **Supplementary Tables**

1285
1286

Table S1. Comparison of the processes included in the bookkeeping method and DGVMs in their estimates of ELUC and SLAND. See Table 4 for model references. All models include deforestation and forest regrowth after abandonment of agriculture (or from afforestation activities on agricultural land). Processes relevant for ELUC are only described for the DGVMs used with land-cover change in this study.

	Bookkeeping models			**DGVMs**																						
	BLUE	OSCAR	LUCE	CABLE-POP	CLASSIC	CLM-FATES	CLM 6.0	DLEM	E3SM	EDv3	GDSTEM	IBIS	iMAPLE	IQJ	ISAM	ISBA-CTRIP	JSBACH	JULES	LPJ-EOSIM	LPJ-GUESS	LPJmL	LPX-Bern	ORCHIDEv4.3.1	SDGVM	VISIT	VISIT-UT	CARDAMOM
Processes relevant for ELUC																										
Wood harvest and forest degradation (a)	yes	yes	yes	yes	no	yes	yes	yes	yes	yes	yes	yes	no	yes	yes	no	yes	no	yes	yes (d)	no	no (c)	yes	no	yes	yes	yes (R+L)
Shifting cultivation / Subgrid scale transitions	yes	yes	yes	yes	no	yes	yes	yes	yes	yes	yes	yes	no	no	no	no	yes	no	yes	yes	no	no (c)	no	no	yes	no	no
Cropland harvest (removed, R, or added to litter, L)	yes (R) (i)	yes (R)	yes (R) (i)	yes (R)	yes (L)	no	yes (R+L)	yes	yes (k)	yes (R+L)	yes (R+L)	yes (R)	yes (k)	yes (R+L)	yes	yes(R+L)	yes (R+L)	yes (R)	yes (k)	yes (R)	yes (R+L)	yes (R)	yes (R)	yes (R)	yes (R)	yse (R)	yes (R)	no
Peat fires	yes (j)	yes (j)	yes (j)	no	no	no	yes	yes	no	no	no	no	no	no	no	no	no	no	no	no	no	no	no	no	no	no	yes (l)

fire as a management tool	yes (i)	yes (g)	yes(i)	no	no	no	no	yes	no	no	no	no	no	no	no	no	no	no	no	no	no	no	no	no	no	yes (l)
N fertilisation	yes (i)	yes (g)	yes(i)	no	yes	no	yes	yes	no	no	yes	yes	no	yes	yes	no	no	yes(h)	no	yes	yes	yes	yes	no	no	yes	no
tillage	yes (i)	yes (g)	yes(i)	no	yes (f)	no	yes	yes	no	no	no (c)	no	no	no	no	no	no	no	no	yes	yes	no	yes (f)	no	no	no	no
irrigation	yes (i)	yes (g)	yes(i)	no	no	no	yes	yes	no	no	yes	no	no	no	yes	no	no	no	no	yes	yes	no	no	no	no	no	no
wetland drainage	yes (i)	yes (g)	yes(i)	no	no	no	no	no	no	no	no	no	no	no	yes	no	no	no	no	no	no	no	no	no	no	no	no
erosion	yes (i)	yes (g)	yes(i)	no	no	no	no	yes	no	no	no	yes	no	no	no	no	no	no	no	no	no	no	no	no	yes	yes	no
peat drainage	yes (j)	yes (j)	yes (j)	no	no	no	no	no	no	no	no	no	no	no	no	no	no	no	no	no	no	no	no	no	no	no	no
Grazing and mowing Harvest (removed, R, or added to litter, L)	yes (R) (i)	yes (R)	yes (R) (i)	yes (R)	no	yes (R)	no	no	no	yes (R+L)	yes (R+L)	no	no	yes (L)	yes (R, L)	no	yes (R+L)	no	yes (k)	yes (R)	yes (R+L)	no	no	no	no	no	no
Processes also relevant for SLAND (in addition to CO2 fertilisation and climate)																											
ecosystem demography (ED) / vegetation competition (VC)				yes (ED), No (VC)	no	yes(ED)	no	no	no	yes	no	yes ED, no VC	no	VC	no ED, yes VC	no	no (VC (c))	No ED, Yes VC	yes	yes	no ED, yes VC	no ED, yes VC	yes ED, no VC	yes (ED), No (VC)	no	no	no

Fire simulation and/or suppression	N.A.	N.A.	N.A.	no	yes	yes	yes	no	yes	yes	no	no	no	no	no	yes	yes	yes	yes	yes	yes	yes	no	yes	yes	yes	yes (l)
Carbon-nitrogen interactions, including N deposition	N.A.	N.A.	N.A.	yes	yes	no	yes	yes	yes	no	yes	no	no (e)	yes	yes	no (b)	yes	yes	no	yes	yes	yes	yes	yes (b)	no	no	no
Separate treatment of direct and diffuse solar radiation	N.A	N.A	N.A	yes	no	yes	yes	no	yes	no	no	yes	yes	yes	no	yes	no	yes	no	no	no	no	no	yes (k)	yes (k)	yes (k)	no

(a) Refers to the routine harvest of established managed forests rather than pools of harvested products.

(b) Limited. Nitrogen uptake is simulated as a function of soil C, and Vcmax is an empirical function of canopy N. Does not consider N deposition.

(c) Available but not active.

(d) without the LUH2 secondary mature, young, and non-forest harvest fractions

(f) Tillage is represented over croplands by increased soil carbon decomposition rate and reduced humification of litter to soil carbon.

(g) as far as the DGVMs that OSCAR is calibrated to include it

(h) perfect fertilisation assumed, i.e. crops are not nitrogen limited and the implied fertiliser diagnosed

(i) Process captured implicitly by use of observed carbon densities.
(j) Emissions added from external datasets.
(k) Diffuse fraction calculated internally, not from external dataset
(l) Fire occurrence added from external dataset, but C impact simulated.

1287

1288
1289
1290

Table S2. Comparison of the processes and model set up for the Global Ocean Biogeochemistry Models for their estimates of SOCEAN. See Table 4 for model references. The table also lists details of the ocean inverse model OCIM, which contributes an ocean interior estimate in Table 6.

	NEMO-PlankTOM12	NEMO4.2-PISCES (IPSL)	MICOM-HAMOCC (NorESM-OCv1.2)	MPIOM-HAMOCC6	FESOM-2.7-REcoM3.1	NEMO4.2.3-PISCESv2-gas (CNRM)	MOM6-COBALTv3 (Princeton)	CESM-ETHZ	MRI-ESM2-4	ACCESS (CSIRO)	OCIM2-48L
Model specifics											
Physical ocean model	NEMOv5-ORCA2	NEMOv4.2-eORCA1L75	MICOM (NorESM-OCv1.2)	MPIOM	FESOM-2.7	NEMOv4.2.3-SI3-eORCA1L75	MOM6-SIS2	CESMv1.3 (ocean model based on POP2)	MRI.COMv5	MOM5	OCIM2-48L
Biogeochemistry model	PlankTOM12	PISCESv2	HAMOCC (NorESM-OCv1.2)	HAMOCC6	REcoM-3.1	PISCESv2-gas	COBALTv3	BEC (modified & extended)	NPZD+Fe	WOMBAT	None (abiotic)
Horizontal resolution	2° lon, 0.3 to 1.5° lat	1° lon, 0.3 to 1° lat	1° lon, 0.17 to 0.25 lat	1.5°	unstructured mesh, 20-120 km resolution (CORE mesh)	1° lon, 0.3 to 1° lat	nominally 0.5 grid spacing (720x576)	1.125° lon, 0.53° to 0.27° lat	1.0° lon, 0.3 to 0.5° lat	1°x1° with enhanced latitudinal resolution in the tropics and high-lat Southern Ocean	2° lon, 1.98° lat
Vertical resolution	31 levels	75 levels, 1m at the surface	51 isopycnic layers + 2 layers representing a bulk mixed layer	40 levels	46 levels, 10 m spacing in the top 100 m	75 levels, 1m at surface	75 levels hybrid coordinates, 2m at surface	60 levels	60 levels with 1-level bottom boundary layer	50 levels, 20 in the top 200m	48 levels, 10 m near the surface to 300 m in the deep ocean
Total ocean area on native grid (km2)	3.6080E+08	3.6360E+08	3.6006E+08	3.6598E+08	3.6435E+08	3.6270E+08	3.6111E+08	3.5926E+08	3.6094E+08	3.6134E+08	3.5635E+08
Gas-exchange parameteriza	Wanninkhof et al (1992)	Orr et al., 2017	Orr et al., 2017, but with a=0.337	Orr et al., 2017	Orr et al., 2017	Orr et al., 2017; Wanninkhof et al. 2014	Deike et al., (2025) wind-wave-bubble formulation	Wanninkhof (1992, coefficient a scaled down to 0.31)	Orr et al., 2017	Wanninkhof et al (1992)	Wanninkhof (2014)

tion											
CO2 chemistry routines	OCMIP2 (Orr et al. 2017)	mocsy	Following Dickson et al. 2007	Ilyina et al. (2013) adapted to comply with OMIP protocol (Orr et al., 2017)	mocsy	mocsy	mocsy	OCMIP2 (Orr et al. 2017)	mocsy	OCMIP2 (Orr et al. 2017)	CO2SYS
River input (PgC/yr) (organic/inorganic DIC)	0.723 / -	0.9167 (0.2577 / 0.659)	0	0.77 / -	0 / 0	0.6743 / -	0.9309 (0.2149/0.7160)	0.33 / -	0 / 0	0/0	0/0
Net flux to sediment (PgC/yr) (organic/other)	0.723 / -	0.4114 (0.08856 / 0.3228)	around 0.54 / -	0.71/-	0 / 0	0.2411 (0.031/0.2411)	0.2995 (~0.156 / ~0.144 (CaCO3))	0.29/ -	0 / 0	0/0	0/0
SPIN-UP procedure											
Initialisation of carbon chemistry	GLODAPv2 (preindustrial DIC)	GLODAPv2 (preindustrial DIC)	GLODAPv1 (preindustrial DIC)	initialization from previous simulation	GLODAPv2 (preindustrial DIC)	GLODAPv2	GLODAPv2 (Alkalinity, DIC)	GLODAPv2 (preindustrial DIC)	GLODAPv2 (preindustrial DIC)	GLODAPv1 preindustrial DIC	Uniform DIC of 2100 umol/kg
Preindustrial spin-up prior to 1850	spin-up 1750-1940	~300 yrs with xCO2=278ppm	1000 year spin up (prior to 1762)	~2000 years	199 years	250 years with xCO2=278 ppm	Spin-up 600 years before the year 1766 with xCO2=278	500 years before year 1780 with xCO2 = 278	1925 years with xCO2 = 278	2000+ years	Spun up to seasonally-varying cyclostationary equilibrium using Newton's method (zero drift)
Atmospheric forcing fields and CO2											

Atmospheric forcing for (i) pre-industrial spin-up, (ii) spin-up 1850-1958 for simulation B, (iii) simulation B	looping ERA5 year 1990	(i) and (ii) looping first ten years (1958-1967) of JRA55-do-v1.4 (spin-up and 1750-1939) ; (iii) looping ten years (1958-1967) of ERA5 (1940-2025)	CORE-I (normal year) forcing (i, ii, iii)	OMIP climatology (i), NCEP year 1957 (ii,iii)	ERA5 repeated year 1961 (i, ii), ERA5 hourly (iii)	(i) preindustrial spin-up 1580-1829: 110 years of a 10-years loop (1958-1967) with JRA55-do-v1.5.0 full reanalysis + 150 years of a 10-years loop with ERA5 3H (1959-1968), (ii) spin-up 1830-1958: 10-years loop with ERA5 3H (1959-1968), (iii) simulation 1959-2025: 10-years loop with ERA5 3H (1959-1968)	ERA5 hourly loop over 1958-1969 (i, ii, iii)	(i, ii, iii): ERA5 NYF (mean of 1958-2024 with 2001 anomalies, with a temporal resolution of 3h)	JRA-3Q repeat year 1990/91 (01May1990 to 30Apr1991) (i, ii, iii)	(i) 800+ years CORE spinup. 750 years with JRA55-do 1990/1991 and 700+ years of cycling ERA5 1958, (ii) and (iii) cycling ERA5 1958.	JRA55 time-averaged wind, sea ice, and atmospheric pressure used for all of these
Atmospheric CO2 for control spin-up 1850-1958 for simulation B, and for simulation B	constant 278ppm; converted to pCO2 temperature formulation (Sarmiento et al., 1992)	xCO2 of 278ppm, converted to pCO2 with constant sea-level pressure and water vapour pressure	xCO2 of 278ppm, converted to pCO2 with sea-level pressure and water vapour pressure	xCO2 of 278ppm, no conversion to pCO2	xCO2 of 278ppm, converted to pCO2 with sea-level pressure and water vapour pressure	xCO2 of 278 ppm, converted to pCO2 with constant sea-level pressure and water vapour pressure	xCO2 of 278ppm, converted to pCO2 with sea-level pressure and water vapour pressure	xCO2 = 278 ppm, converted to pCO2 with atmospheric pressure, and water vapour pressure	xCO2 of 278ppm, converted to pCO2 with water vapour and sea-level pressure (JRA-3Q repeat year 1990/91)	xCO2 of 278ppm, converted to pCO2 with sea-level pressure	Spun up to equilibrium under atmospheric xCO2 of 277.5 ppm, corresponding to year 1700 in the GCB Atm_CO2_forcing.csv file, converted to sea level pCO2 with atmospheric pressure and water vapor pressure
Atmospheric forcing for historical spin-up 1850-1958 for simulation A (i) and for simulation A (ii)	1750-1947: looping ERA5 year 1990; 1948-2023: ERA5	(i) looping first ten years (1958-1967) of JRA55-do-v1.4 (1750-1939) ; (ii) full ERA5 reanalysis (1940-2025)	CORE-I (normal year) forcing; from 1948 onwards NCEP-R1 with CORE-II corrections	NCEP 6 hourly cyclic forcing (10 years starting from 1948, i), 1948-2021: transient NCEP forcing	ERA5 repeated year 1961 (i), ERA5 hourly (ii)	pre-industrial spin-up (1580-1829) then (i) spin-up 1830-1958: 10-years loop with ERA5 3H (1959-1968), (ii) simulation 1959-2025: full ERA5 3H reanalysis (1959-2025)	ERA5 hourly loop over 1958-1969 (i), ERA5 hourly ii)	(i, ii): ERA5 at 3h resolution, repeat cycle 1958-2024	1636-1947 and 1948-1958 (till 2025): repeated cycle JRA-3Q 1948-2025	(i) cycling ERA5 1958, (ii) ERA5 for 1958-2025.	No simulation A performed

Atmospheric CO2 for historical spin-up 1850-1958 for simulation A (i) and simulation A (ii)	xCO2 provided by the GCB; converted to pCO2 temperature formulation (Sarmiento et al., 1992), monthly resolution (i, ii)	xCO2 as provided by the GCB, global mean, annual resolution, converted to pCO2 with sea-level pressure and water vapour pressure (i, ii)	xCO2 as provided by the GCB, converted to pCO2 with sea level pressure (taken from the atmopheric forcing) and water vapor correction (i, ii)	transient monthly xCO2 provided by GCB, no conversion (i, ii)	xCO2 as provided by the GCB, converted to pCO2 with sea-level pressure and water vapour pressure, global mean, monthly resolution (i, ii)	From 1830: xCO2 as provided by the GCB, converted to pCO2 with constant sea-level pressure and water vapour pressure, global mean, yearly resolution (i, ii)	xCO2 as provided by GCB, converted to pCO2 with sea-level pressure and water vapour pressure, global mean, yearly resolution (i, ii)	xCO2 as provided by the GCB in 2025 (from 1780 onward), converted to pCO2 with locally determined atm. pressure, and water vapour pressure (i, ii)	xCO2 as provided by GCB, converted to pCO2 with water vapour and sea-level pressure (i, ii).	xCO2 as provided by the GCB, converted to pCO2 with sea-level pressure	No simulation A, but for simulation C the GCB xCO2 forcing file was used, converted to pCO2 with water vapor and sea level pressure

Table S3: Description of ocean *f*CO2-products used for assessment of S_{OCEAN}. See Table 4 for references.

	Jena-MLS	VLIZ-SOMFFN	CMEMS-LSCE-FFNN	UExP-FNN-U (previously Watson et al.)	NIES-ML3	JMA-MLR	OceanSODA-ETHZv2	LDEO HPD	AOML-ET	SJTU-AVIT

Method	Spatio-temporal interpolation (version oc_v2026). Spatio-temporal field of ocean-internal carbon sources/sinks is fit to the SOCATv2026 pCO2 data. Includes a multi-linear regression against environmental drivers to bridge data gaps,	A feed-forward neural network (FFN) determines non-linear relationship between SOCAT pCO2 measurements and environmental predictor data for 16 biogeochemical provinces (defined through a self-organizing map, SOM) and is used to fill the existing data gaps.	An ensemble of neural network models trained on 100 subsampled datasets from SOCAT and environmental predictors. The models are used to reconstruct sea surface fugacity of CO2 and convert to air-sea CO2 fluxes	A self-organising map feed forward neural network (SOM-FNN) implementation using SOCATv2026 recalculated to the subskin temperature (ESA CCI v3 bias corrected to surface drifter data following recommendations in Dong et al. 2022) of the ocean as measured by satellites (described in Ford et al. 2026). Flux calculation corrected for the cool and salty surface skin. Monthly skin temperature calculated from ESA CCI v3 (Embury et al. 2024) with the cool skin difference calculated using NOAA COARE 3.6. Flux calculations completed using FluxEngine v4.2.0 (Shutler et al., 2016; Holding et al., 2019).	The ensemble of a random forest, a gradient boost machine, and a feed forward neural network trained on SOCAT 2025 fCO2 and environmental predictor variables. The interannual trend of fCO2 was estimated first by the decadal trend of atmospheric CO2 and then corrected by a so-called leave-one-year-out validation method. The trend was used to normalize fCO2 to the mid year of 1982-2024 for model training. The monthly fCO2 maps were reconstructed using model prediction and the trend.	Fields of total alkalinity (TA) were estimated by using a multiple linear regressions (MLR) method based on GLODAPv3 and satellite observation data. SOCATv2026 recalculated fCO2 data were converted to dissolved inorganic carbon (DIC) with the TA. Fields of DIC were estimated by using a MLR method based on the DIC and satellite observation data	OceanSODA-ETHZv2 is a two-phase machine learning approach. In phase 1, we estimate the ΔfCO2 8-day seasonal cycle climatology with a Gradient Boosted Decision Tree which is used as a predictor in the next phase. In phase 2, we predict the non-thermal component of ΔfCO2 at a 8-day by 0.25° by 0.25° resolution with a two-layer fully-connected neural network using 35 ensemble members. The atmospheric CO2 and non-thermal component are added back to the result.	Based on fCO2-misfit between observed fCO2 and 10 global carbon budget GOBMs. The eXtreme Gradient Boosting method links this misfit to environmental observations to reconstruct the model misfit across all space and time, which is then added back to the model fCO2 estimate. The final reconstruction of surface fCO2 is the average across the 10 reconstructions. A climatology of the misfits calculated for the years 2000-2025 is used as an offset for years prior to 1982 when limited environmental observations are available to train the ML algorithm.	A hybrid machine-learning approach is used to reconstruct monthly surface-ocean fCO2. A generalized additive model (GAM) provides the large-scale spatial, temporal and environmental baseline, followed by two Extremely Randomized Trees (ET) stages that learn residual structure and refine the final estimate. The model is trained on SOCATv2026 recalculated fCO2 using SST, SSS, mixed-layer depth, chlorophyll, latitude/longitude and seasonal/time predictors, and is then applied globally on the 1° ocean grid.	Vision Transformer pretrained on seven CMIP6 models and fine-tuned with MOM6-COBALT2 and SOCATv2024. Predictors include SST, SSS, Chl-a, MLD, atmospheric CO2 and carbonate-system sensitivities to SST, SSS, DIC and alkalinity (Zhang et al., 2025).
Gas-exchange parameterization	Wanninkhof 1992. Transfer coefficient k scaled to match a global mean transfer rate of 16.5 cm/hr by (Naegler, 2009)	Wanninkhof 2014. Transfer coefficient k scaled to match a global mean transfer rate of 16.5 cm/hr (Naegler, 2009)	Wanninkhof 2014. Transfer coefficient k scaled to match a global mean transfer rate of 16.5 cm/hr (Naegler, 2009)	Nightingale et al 2000	Wanninkhof, 2014. Transfer coefficient k scaled to match a global mean transfer rate of 16.5 cm/hr in 1990-2019 (Fay et al., 2021)	Wanninkhof, 2014. Transfer coefficient k scaled to match a global mean transfer rate of 16.5 cm/hr (Naegler, 2009; Fay, Gregor et al. 2021)	Wanninkhof 1992, averaged and scaled for three reanalysis wind data, to a global mean 16.5 cm/hr (after Naegler 2009; Fay & Gregor et al. 2021)	Wanninkhof 1992 parameterization. Transfer coefficient k scaled to match a global mean transfer rate of 16.5 cm/hr (Naegler, 2009)	Wanninkhof (2014). Transfer coefficient k scaled to match a global mean transfer rate of 16.5 cm h^{-1} (Naegler, 2009; Fay et al., 2021).	Wanninkhof (2014), quadratic wind-speed dependence with coefficient 0.251 (global mean transfer velocity approximately 16 cm/hr).
Wind product	JMA55-do reanalysis	ERA 5	ERA5	CCMP3.1	ERA5	JRA3Q	ERA5	ERA5	ERA5	ERA5

Spatial resolution	2.5 degrees longitude x 2 degrees latitude regridded to 1x1 degree	1x1 degree	0.25x0.25 degree regridded to 1x1 degree	1x1 degree	1x1 degree	1x1 degree	0.25x0.25 degree regridded to 1x1 degree	1x1 degree	1x1 degree	1x1 degree
Temporal resolution	daily	monthly	monthly	monthly	monthly	monthly	8-daily regridded to monthly	monthly	monthly	monthly
Atmospheric CO2	Spatially and temporally varying field based on atmospheric CO2 data from 169 stations (Jena CarboScope atmospheric inversion)	Spatially varying 1x1 degree atmospheric pCO2_wet calculated from the NOAA ESRL marine boundary layer xCO2 and NCEP sea level pressure with the moisture correction by Dickson et al 2007.	Spatially and monthly varying fields of atmospheric pCO2 computed from CO2 mole fraction (CO2 atmospheric inversion from the Copernicus Atmosphere Monitoring Service), and atmospheric dry-air pressure which is derived from monthly surface pressure (ERA5) and water vapour pressure fitted by Weiss and Price 1980	Atmospheric fCO2 (wet) calculated from NOAA marine boundary layer XCO2(atm) and ERA5 sea level pressure, with pH2O calculated following Dickson et al. (2007). 2025 xCO2(atm) marine boundary values were not available at submission so we used preliminary values, estimated from 2024 values and increase at Mauna Loa.	NOAA Greenhouse Gas Marine Boundary Layer Reference. https://gml.noaa.gov/ccgg/mbl/mbl.html	Atmospheric xCO2 fields of JMA-GSAM inversion model (Maki et al. 2010) were converted to pCO2 by using JRA3Q sea level pressure. 2025 xCO2 fields were not available at this stage, and we used Cape Grim and Mauna Loa xCO2 increments from 2024 to 2025 for the southern and northern hemispheres, respectively.	NOAA's marine boundary layer (MBL) product (1980 - 2023) is used for atmospheric xCO2. For the year 2024, a linear regression is performed between deseasonalised Mauna Loa (1970 - 2025) and MBL data for each latitude of the latter. The mean seasonal cycle is added back to the interpolated data for 2024. The MBL xCO2 (now 1980 - 2024) is linearly interpolated onto a 0.25°x0.25° grid and resampled from weekly to 8-daily. xCO2 is multiplied by ERA5 mean sea level pressure, where the latter corrected for water vapour pressure using Dickson et al. (2007). These results are regridded to a monthly 1x1 degree pCO2atm.	NOAA's marine boundary layer (MBL) surface xCO2 product is linearly interpolated to a 1x1 degree monthly grid for years 1979 onward. Prior to 1979, calculating an offset between the MBL and Mauna Loa seasonal climatologic xCO2 values for a subset of common years (1979-1989) yields a mean seasonality difference which is then applied to the Mauna Loa time series pre-1979. This results in a latitudinal-varying xCO2 time series for years prior to 1979, based on the long term trajectory estimated at Mauna Loa. Monthly 1x1 degree xCO2 is multiplied by ERA5 mean sea level pressure, with the correction for water vapour pressure using Dickson et al. 2007, using ERA5 SST and EN4 SSS. FInally converted to fCO2 using ERA5 SST and SLP.	Spatially varying 1x1 degree atmospheric pCO2_wet calculated from the NOAA ESRL marine boundary layer xCO2 and NCEP sea level pressure with the moisture correction by Dickson et al 2007.	NOAA ESRL marine boundary layer xCO2, interpolated in latitude and replicated across longitude onto a 1 x 1 degree grid. Atmospheric pCO2 includes the water-vapour correction of Dickson et al. (2007).

Total ocean area on native grid (km2)	3.63E+08	3.63E+08	3.50E+08	361000000	329000000	303000000	354615000	3.586 E+8	3.63E+08	3.44 E+8
method to extend product to full global ocean coverage		Arctic and marginal seas added following Landschützer et al. (2020). No coastal cut.				Fay & Gregor et al. 2021	Coverage of the global ice free ocean (ice frac < 0.9)	Based on method in Fay & Gregor et al. 2021. Gaps were filled with monthly climatology (Landschützer et al. 2020) scaled for interannual variability based on the temporal evolution of this product for all years.	The trained model is applied directly to all available cells of the global 1° ice-free ocean grid.	Method has near full coverage

1313

1314

Table S4. Comparison of the inversion set up and input fields for the atmospheric inversions. Atmospheric inversions see the full CO2 fluxes, including the anthropogenic and pre-industrial fluxes. Hence they need to be adjusted for the pre-industrial flux of CO2 from the land to the ocean that is part of the natural carbon cycle before they can be compared with SOCEAN and SLAND from process models. See Table 4 for references.

Name	Carbon-Tracker Europe insitu (CTE-insitu)	Carbon-Tracker Europe satellite (CTE-satelite)	NISMON-CO2	CT-NOAA	CMS-Flux	Copernicus Atmosphere Monitoring Service (CAMS) SRF	Copernicus Atmosphere Monitoring Service (CAMS) SAT	GONGGA	CarboScope	COLA	GCASv2	UoE	NTFVAR	THU	NISMON-CO2_GOSAT	YanDong
Version number	V2026.1	V2026.1	v2026.1	CT2026	v2026	V25r1	FT26r1	v2026	r76nbetEXToc_v2026	v2026	v2026	v2026	v2026	v2026	v2026.1	v2026
QC-Flag Observations																
Atmospheric observations (a,b)	Obspack GLOBALVIEW plus v11.0 and NRT_v11.0	Obspack GLOBALVIEW plus v11.0 and NRT_v11.0 (continental sites excluded) +	Hourly resolution (well-mixed conditions) obspack GLOBALVIEW plus v11.0 and NRT_v11	Hourly resolution (well-mixed conditions) obspack GLOBALVIEW plus v11.0 and NRT_v11	OCO-2 V11.2 and v11.3 and obspack GLOBALVIEW plus v10.1 and NRT_v10.1	Obspack GLOBALVIEW plus v11.0 and NRT_v11.0	OCO-2 ACOS retrievals from NASA, v11.2 and v11.3	OCO-2 v11.2r and v11.3r data that were scaled to the WMO 2019 standard	Flasks and hourly from various institutions (outliers removed by 2σ criterion)	Hourly resolution (well-mixed conditions) obspack GLOBALVIEWplus v11.0 and NRT_v11.0. And OCO-2_b11.2_L	ACOS v11.2r and v11.3r OCO-2 XCO2 retrievals, scaled to the WMO 2019 standard	Hourly resolution (well-mixed conditions) obspack GLOBALVIEWplus v11.0 and NRT_v11.0	Hourly resolution (well-mixed conditions) obspack GLOBALVIEWplus v11.0 and NRT_v11.0 and GOSAT XCO2 data	OCO-2 v11.2r and v11.3r data that were scaled to the WMO 2019 standard	NIES GOSAT SWIR L2 Product ver03.05 that were taken only over land (GOSAT)	obspack GLOBALVIEWplus v11.0 and NRT_v11.0 and OCO-2 v11.2r and v11.3r data, scaled to

		OCO-2 ACOS retrievals from NASA, v11.2 and v11.3	.0	.0						NLG and OCO-2_b11.3_LNLG			NIES Level 2 product v03.05			WMO 2019 standard
Period covered Prior fluxes	2001-2025	2015-2025	1990-2025	2000-2025	2015-2025	1979-2025	2015-2025	2015-2025	1976-2025	2015-2025	2015-2025	2001-2025	2010-2025	2015-2025	2010-2025	2015-2025
Biosphere and fires	SiB4-MERRA and GFAS	SiB4-MERRA and GFAS	GPP and RE from the climatological mean of NISMON-CO2_SRF	MiCASA v1 (includes GFEDv3) and SiB4 (includes GFED4.1s)	CARDAMOM simulated fire emissions with GFED4.1 burned area before 2024,	ORCHIDEE, GFEDv4.1s	ORCHIDEE, GFEDv4.1s	ORCHIDEE-MICT and GFEDv4.1s	Zero	VEGAS + GFAS	BEPS and GFED4.1s	CASA v1.0, climatology after 2016, and GFED4.0	Zeng et al. 2020 and GFAS	SiB4.2 and GFEDv4.1s	GPP and RE from the climatological mean of NISMON-CO2_SRF ver2025.1. VISIT for LUC.	ORCHIDEE-MICT and GFEDv4.1s

Ocean	CarboScope v2025	CarboScope v2025	ver2025.1. VISIT for LUC. JMA global ocean mapping (Iida	AOML-Extra Trees surface ocean pCO2 and SOM-FFN	GFAS fire emissions in 2024 ECCO-Darwin and MOM6	CMEMS-LSCE-FFNN 2025	CMEMS-LSCE-FFNN 2025	Takahashi climatology with a trend	CarboScope oc_v2026	Jena OC-v2025	JMA Ocean CO2 Map v2025 (Global) and v2026 (regional)	Takahashi climatology with a trend	Zeng et al. 2014, 2022	Takahashi climatology, without trend	JMA global ocean mapping (Iida et al., 2021)	The Ocean Inversion Fluxes prior
Fossil fuels (c)	GridFED 2026.0	GridFED 2026.0	GridFED v2026.0	Miller and OCO-2 v2026.1	GridFED 2025.1 with an extrapolation to 2025-26 based on Carbonmonitor and NO2 retrievals	GridFED 2025.1 with an extrapolation to 2025-26 based on Carbonmonitor and NO2 retrievals	GridFED 2025.1 with an extrapolation to 2025-26 based on Carbonmonitor and NO2 retrievals	GridFED 2026.0	GridFED v2026.0	GridFEDv2024.0 and v2026.0	GridFEDv2026.0	GridFED 2026.0	GridFEDv2026.0	GridFEDv2026.0	GridFED v2026.0	GridFED v2026.0
Transport and optimization																
Transport model	TM5	TM5	NICAM-TM	TM5	GEOS-Chem	LMDZ v6	LMDZ v6	GEOS-Chem v12.9.3	TM3	GEOS-Chem v13.0.2	MOZART-4	GEOS-Chem	NIES-TM-FLEXPART	GEOS-Chem v12.2	NICAM-TM	GEOS-Chem v14.1.1

Weather forcing	ECMWF	ECMWF	JRA-3Q	ERA5	MERRA2	ECMWF	ECMWF	MERRA2	ERA5	MERRA-2	GEOS5	MERRA-2	ERA5(NIES-TM)/JRA-55(FLEXPART)	GEOS-FP	JRA-3Q	MERRA-2
Horizontal resolution	Global 3x2 in 1st step, Global 1x1 in 2nd step	Global 3x2 in 1st step, Global 1x1 in 2nd step	glevel-5 (~223 km)	Global 3x2 , North America 1x1	Global 4x5	global ~90 km in the horizontal (hexagons)	global ~90 km in the horizontal (hexagons)	Global 2x2.5	Global 4x6	2°×2.5°	2.5°×1.875°	Global 2°x2.5°	NIES-TM 3.75°x3.75° and FLEXPART 0.1°x0.1°	Global 4° x 5°	glevel-5 (~223 km)	Global 2°x2.5°
Optimization	26 year Ensemble Kalman filter followed by 3 day Ensemble Kalman filter	26 year Ensemble Kalman filter followed by 2x5 day Ensemble Kalman smoother	Variational	12-week ensemble Kalman smoother	Variational	Variational	Variational	Nonlinear least squares four-dimensional variation (NLS-4DVar)	Conjugate gradient (re-ortho-normalization)	Ensemble Kalman Filter (LETKF with CEnKF/AAPO)	Ensemble Kalman filter	Ensemble Kalman filter	Variational, M1QN3	Ensemble Kalman filter	Variational	Ensemble Kalman Filter

(a) Schuldt et al. 2025. Multi-laboratory compilation of atmospheric carbon dioxide data for the period 1957-2024; obspack_co2_1_GLOBALVIEWplus_v11.0_2026-01-12; NOAA Earth System Research Laboratory, Global Monitoring Laboratory. http://doi.org/10.25925/20250801.

(b) Schuldt et al. 2026. Multi-laboratory compilation of atmospheric carbon dioxide data for the period 2025-2026; obspack_co2_1_NRT_v11.0_2026-05-14; NOAA Earth System Research Laboratory, Global Monitoring Laboratory. http://doi.org/10.25925/20260430.

(c) GCP-GridFED v2026.0 and earlier (Jones et al., 2025) are updates of the GCP-GridFED dataset presented by Jones et al. (2021b).

1315

1316
1317

1318

Table S5: Overview of the Earth System Models (ESMs) and the simulations.						
Model	CanESM5	EC-Earth3-CC	IPSL-CM6A-CO2-LR	MIROC-ES2L	MPI-ESM1.2-LR	NorCPM-CC
Resolution Atmosphere	T63, 49 hybrid levels up to 1hPa	T255, 91 levels	2.5°x1.25°, 79 levels	T42, 40 levels	T63, 47 levels	2.5x1.875°, 32 levels
Resolution Ocean	1° refined meridionally to 1/3° near Equator, 45 levels	1°, 75 levels	1° (nominal), 75 levels	Tripolar (~1°), 62 levels	1.5°, 40 levels	1°, 53 sigma levels
Assimilation Atmosphere	ERA-Interim (Dee et al. 2011) from 1980 to 2018 and ERA5 (Hersbach et al. 2020) afterwards: full-field nudging of temperature, horizontal wind and specific humidity. Globally averaged atmospheric CO2 concentration at the lowest model level is constrained by prescribed values (Arora and Scinocca, 2016).	ERA5 (Hersbach et al. 2020) full-field	None	3D full field wind and T of JRA55 (Kobayashi et al. 2015) with the simplified IAU (Tatebe et al. 2012)	ERA-40 (Uppala et al. 2005) before 1979 and ERA5 (Hersbach et al. 2020) from 1980: Vorticity, divergence, log(p), T; full field with nudging	None

Assimilation Ocean	Nudging to 3D potential temperature and salinity from ORAS5 reanalysis (Zuo et al. 2019). Sea surface temperature relaxed to interpolated values from NOAA's OISSTv2 from Nov. 1981 to present, and NOAA's ERSSTv3 prior (Smith et al. 2008).	EN4 (Good et al. 2013) 3D nudging T and S with weaker nudging band around equator. SST and SSS restoring to ORAS5 (Zuo et al. 2019). Atmospheric forcing: DFS5.2 1958-1979 and ERA5 after 1980	Nudging towards SST (ERSSTv5) and SSS (EN4) using a restoring coefficient dependent on the mixed layer depth (Ortega et al. 2017)	3D full field T, S, and sea-ice concentration of an ocean objective analysis (Ishii and Kimoto 2009) with the simplified IAU (Tatebe et al. 2012)	EN4 (Good et al. 2013) 3D full field T and S with ensemble Kalmann filter (Brune et al. 2018)	ENKF anomaly assimilation of monthly T and S from EN4, monthly SST from HADISST during 1975-1981, and daily SST from OISSTv2 during 1982-2023
Assimilation Land	Indirectly through response of CLASS-CTEM to the data-constrained coupled ESM	LPJ-GUESS forced offline with ERA5 1979-2020 after preindustrial spinup+transient up to 1979	None	None	Indirectly initialized by atmospheric and oceanic data assimilation within the fully coupled ESM	None
Ensemble Size	10	10	10	10	10	10
Period of reconstruction	1960-2025	1980-2025	1960-2025	1960-2025	1960-2025	1975-2025
Hindcasts and forecasts	1 year starting from Jan. 1st 1980-2026	14 months starting from Nov.1st 1980-2025	1 year starting from Jan. 1st 1981-2026	14 months starting from Nov. 1st 1980-2025	14 months starting from Nov.1st 1980-2025	16 months starting from Nov. 1st 1980-2025
External forcings	The Coupled Model Intercomparison Project Phase 6 (CMIP6) historical (1960-2014) plus SSP2-4.5 baseline and CovidMIP two year blip scenario (after 2015) (Eyring et al. 2016; Lamboll et al. 2021). The CO2 emissions forcing from 2015 onward are substituted by GCP-GridFED (v2024.0, Jones et al., 2025), which is an update to Jones et al. (2021), for all the models except for IPSL-CM6A-CO2-LR. The CO2 emissions forcing for year 2025 is an extension with the same emission of the year 2024; and the CO2 emissions forcing for year 2026 use the 2025 emissions adding on top the increment of 2026 emissions in CMIP6 SSP2-4.5 scenario.					

	Note the difference in global integrated CO2 emissions between CMIP6 CovidMIP and GCP-GridFED in recent years is within the emission uncertainty.					
References	Swart et al. 2019; Sospedra-Alfonso et al. 2021	Döscher et al. 2021; Bilbao et al., 2021; Bernardello et al., 2024	Boucher et al. 2020	Watanabe et al. 2020	Mauritsen et al. 2019; Li et al. 2023	Tjiputra et al. 2020; Bethke et al. 2021

1319

1320

1321

Table S6. Comparison of the projection with realised fossil CO_2 emissions (EFOS). The 'Actual' values are first the estimate available using actual data (e.g., the actual 2020 value is from the 2021 budget), and the 'Projected' values refers to estimates made before the end of the year for each publication (e.g., the projected 2020 value is from the 2020 budget). Projections based on a different method from that described here during 2008-2014 are available in Le Quéré et al., (2016). All values are adjusted for leap years.

	World		China		USA		EU28 / EU27 (i)		India		Rest of World (ii)	
	Projected	Actual	Projected	Actual	Projected	Actual	Projected	Actual	Projected	Actual	Projected	Actual
2015 (a)	–0.6%	0.06%	–3.9%	–0.7%	–1.5%	–2.5%	–	–	–	–	1.2%	1.2%
	(–1.6 to 0.5)		(–4.6 to –1.1)		(–5.5 to 0.3)						(–0.2 to 2.6)	
2016 (b)	–0.2%	0.20%	–0.5%	–0.3%	–1.7%	–2.1%	–	–	–	–	1.0%	1.3%
	(–1.0 to +1.8)		(–3.8 to +1.3)		(–4.0 to +0.6)						(–0.4 to +2.5)	
2017 (c)	2.0%	1.6%	3.5%	1.5%	–0.4%	–0.5%	–	–	2.00%	3.9%	1.6%	1.9%
	(+0.8 to +3.0)		(+0.7 to +5.4)		(–2.7 to +1.0)				(+0.2 to +3.8)		(0.0 to +3.2)	

2018 (d)	2.7%	2.1%	4.7%	2.3%	2.5%	2.8%	-0.7%	-2.1%	6.3%	8.0%	1.8%	1.7%
	(+1.8 to +3.7)		(+2.0 to +7.4)		(+0.5 to +4.5)		(-2.6 to +1.3)		(+4.3 to +8.3)		(+0.5 to +3.0)	
2019 (e)	0.5%	0.1%	2.6%	2.2%	-2.4%	-2.6%	-1.7%	-4.3%	1.8%	1.0%	0.5%	0.5%
	(-0.3 to +1.4)		(+0.7 to +4.4)		(-4.7 to -0.1)		(-5.1% to +1.8%)		(-0.7 to +3.7)		(-0.8 to +1.8)	
2020 (f)	-6.7%	-5.4%	-1.7%	1.4%	-12.2%	-10.6%	-11.3% (EU27)	-10.9%	-9.1%	-7.3%	-7.4%	-7.0%
2021 (g)	4.8%	5.1%	4.3%	3.5%	6.8%	6.2%	6.3%	6.8%	11.2%	11.1%	3.2%	4.5%
	(4.2% to 5.4%)		(3.0% to 5.4%)		(6.6% to 7.0%)		(4.3% to 8.3%)		(10.7% to 11.7%)		(2.0% to 4.3%)	
2022 (h)	1.1%	0.9%	-1.5%	0.9%	1.6%	1.0%	-1.0%	-1.9%	5.6%	5.8%	2.5%	0.6%
	(0% to 1.7%)		(-3.0% to 0.1%)		(-0.9% to 4.1%)		(-2.9% to 1.0%)		(3.5% to 7.7%)		(0.1% to 2.3%)	

2023 (j)	1.1%	1.3%	4.0%	4.9%	-3.0%	-3.3%	-7.4%	-8.4%	8.2%	8.2%	0.4%	0.7%
	(0.0% to 2.1%)		(1.9% to 6.1%)		(-5% to -1%)		(-9.9% to -4.9%)		(6.7% to 9.7%)		(-1.4% to 2.3%)	
2024 (k) GCB	0.80%	1.1%	0.10%	0.70%	-0.90%	-0.60%	-2.80%	-2.60%	3.70%	4.00%	1.20%	1.90%
	(-0.2% to 1.7%)		(-1.7% to 1.9%)		(-2.1% to 0.3%)		(-5.2% to -0.3%)		(3.3% to 4.0%)		(0.7% to 3.2%)	
2024 (k) CM	0.80%		-0.80%		1.30%		-4.50%		5.00%		1.50%	
	(0.5% to 1.1%)		(-1.3% to -0.4%)		(1.1% to 1.6%)		(-5.4% to -3.6%)		(4.4% to 5.5%)		(-1.2% to 1.8%)	
2025 (l) GCB	1.0%	1.2%	0.4%	0.4%	2.5%	2.8%	-0.1%	0.0%	1.1%	1.2%	0.9%	0.5%
	(0.2% to 1.7%)		(-0.1% to 0.9%)		(2.2% to 2.8%)		(-2.6% to 2.3%)		n.a.		(-1.1% to 3.0%)	
2025 (l) CM	0.7%		-0.6%		1.4%		0.8%		0.7%		1.3%	
	n.a.		n.a.		n.a.		n.a.		n.a.		n.a.	

(a) Jackson et al. (2016) and Le Quéré et al. (2015a). (b) Le Quéré et al. (2016). (c) Le Quéré et al. (2018a). (d) Le Quéré et al. (2018b). (e) Friedlingstein et al., (2019), (f) Friedlingstein et al., (2020), (g) Friedlingstein et al., (2022a), (h) Friedlingstein et al., (2022b), (j) Friedlingstein et al., (2023), (k) Friedlingstein et al. (2025a), (l) Friedlingstein et al. (2026a).
(i) EU28 until 2019, EU27 from 2020
(ii) From 2023, the projection for Rest of World is composed of separate projections for aviation bunkers, maritime bunkers, and all other countries.
(iiI) The projection for the World includes the projection on cement carbonation

1322

1323

1324

Table S7 Comparison of the projected and assessed estimates of G_{ATM}, S_{LAND} and S_{OCEAN}. The 'actual' values refer to the estimates available using observations and comprehensive models/data streams (e.g., the actual 2025 value from the 2026 GCB budget publication) and the 'projected' values refer to the estimates made before the end of the year for each publication (e.g., the projected 2025 value from the 2025 GCB budget publication). All units in GtC/yr.

	G_{ATM}		S_{OCEAN}		S_{LAND}	
	Projected	Actual	Projected	Actual	Projected	Actual
2021	5.3 ± 0.1	5.2 ± 0.2	2.9 ± 0.4	2.9 ± 0.4	3.3 ± 1.0	3.5 ± 0.8
2022	5.3 ± 0.4	4.6 ± 0.2	2.9 ± 0.4	2.8 ± 0.4	3.4 ± 0.9	3.8 ± 0.8
2023	5.1 ± 0.4	5.9 ± 0.2	2.9 ± 0.6	2.9 ± 0.4	2.9 ± 1.2	2.3 ± 0.8
2024	6.1 ± 0.3	7.9 ± 0.2	3.0 ± 0.6	3.4 ± 0.6	3.2 ± 1.5	1.9 ± 0.8
2025	4.9 ± 0.2	4.4 ± 0.2	3.2 ± 0.4	3.2 ± 0.4	3.4 ± 1.0	3.6 ± 0.9

Note: the 2024 projections of S_{OCEAN} and S_{LAND} are not corrected as in the GCB2024, while the actual estimates are corrected, as in GCB2025. The uncorrected 2024 estimates of S_{OCEAN} and S_{LAND} are 3.2 ± 0.6 and 2.5 ± 0.9 GtC/yr respectively.

1345
1346

Table S8 Attribution of fCO_2 measurements for the year 2025 included in SOCATv2026 (Bakker et al., 2016, 2026) to inform ocean fCO_2-based data products.

Platform Name	Regions	Days of data	Dataset doi	Dataset citation
Allure of the Seas	Coas	26	https://doi.org/10.25921/8hkd-w728	Wanninkhof et al. (2025b)
Arni Fridriksson	Coas; NAtl; Arct	47	https://doi.org/10.25921/3s7j-5w56	Benoit-Cattin (2026)
Astrolabe	SOce	31	https://doi.org/10.25921/11qg-bz22	Tilbrook et al. (2026)
Atlantic Explorer	Coas; NAtl; TAtl	106	https://doi.org/10.25921/jzzh-vq02	Bates and Enright (2026a)
Bell M. Shimada	Coas; NPac; TPac	97	https://doi.org/10.25921/ezn3-q004	Alin et al. (2026a)
BlueFin	TPac; Coas; NPac	40	https://doi.org/10.25921/1e16-4t24	Alin et al. (2026e)
CB-06_125W_43N	Coas	85	https://doi.org/10.25921/rr8z-se53	Sutton et al. (2025a)
Celtic Explorer	Coas; NAtl; TAtl	99	N/A	N/A
Equinox	Coas; NAtl; TAtl	27	https://doi.org/10.25921/1q1z-tx93	Wanninkhof et al. (2025a)
ES-SOOP-CanOA	Coas	23	https://doi.org/10.18160/88C7-K7P9	Santana-Casiano et al. (2026)
F.G. Walton Smith	Coas	24	https://doi.org/10.25921/qzwf-se04	Barbero et al. (2026)
Finnmaid	Coas	317	https://doi.org/10.18160/NA24-25YF	Rehder et al. (2026)
G.O. Sars	Coas; NAtl; Arct	241	https://doi.org/10.18160/G60G-VQ58	Skjelvan et al. (2026)
GAKOA_149W_60N	Coas	63	https://doi.org/10.3334/cdiac/otg.tsm_gakoa_149w_60n	Monacci et al. (2025b)
Gordon Gunter	Coas; NAtl	59	https://doi.org/10.25921/ktst-qc70	Wanninkhof and Pierrot (2026a)
Healy	Coas; NPac; Arct	109	https://doi.org/10.25921/3syk-0t70	Sweeny et al. (2026c)

Henry B. Bigelow	Coas; NAtl	35	https://doi.org/10.25921/z2j3-x957	Wanninkhof and Pierrot (2026b)
Heron Island	Coas	145	https://doi.org/10.3334/cdiac/otg.tsm_heron_152e_23s	Tilbrook et al. (2012)
Holcim-PRB	Coas; NAtl; SOce; TAtl	21	https://doi.org/10.25921/h176-tz06	Olivier and Landschützer (2026)
Investigator	SOce	94	https://doi.org/10.25921/9qgr-pj77	Tilbrook et al. (2025)
James Cook	Coas; NAtl	24	https://doi.org/10.25921/9xqt-t091	Hartman et al. (2026)
Kangaroo Island	SOce	145	https://doi.org/10.25921/c2ry-gk21	Tilbrook et al. (2022)
KC_BUOY	Coas	262	https://doi.org/10.21966/hz11-3m59	Evans et al. (2025a)
Keifu Maru II	Coas; NPac; TPac	93	https://doi.org/10.25921/5z8d-2e87	Kadono and Enyo (2026)
KEO_145E_32N	NPac	101	https://doi.org/10.3334/cdiac/otg.tsm_keo_145e_32n	Sutton et al. (2026a)
Kronprins Haakon	Arct; Coas; NAtl	82	https://doi.org/10.18160/Y51V-HFE5	Fransson et al. (2026)
Le Commandant Charcot	Coas; NAtl; Arct; SOce	138	https://doi.org/10.25921/0qgc-0c52	Pierrot and Wanninkhof (2026)
M2_164W_57N	Coas	124	https://doi.org/10.3334/cdiac/otg.tsm_m2_164w_57n	Monacci et al. (2025a)
Maria Island	SOce	301	https://doi.org/10.7289/v5bv7dt6	Tilbrook et al. (2017)
Marion Dufresne	Indi; SOce	25	https://doi.org/10.25921/ztee-xr07	Lo Monaco and Metzl (2026)
MV Oleander	Coas; NAtl	134	https://doi.org/10.25921/jsff-wk47	Bates and Enright (2026b)
Nathaniel B. Palmer	SOce	92	https://doi.org/10.25921/4ez1-ck76	Sweeny et al. (2026a)
New Century 2	Coas; NPac; SOce; TPac; NAtl	245	https://doi.org/10.25921/c5kn-5a07	Nakaoka et al. (2026a)
Orford_BUOY	Coas	273	https://doi.org/10.21966/4jvz-bv44	Evans et al. (2026)

Oscar Dyson	Coas	69	https://doi.org/10.25921/k0fw-mv14	Alin et al. (2026c)
Oshoro Maru V	Coas; NPac	51	https://doi.org/10.25921/qtna-bn06	Aramaki et al. (2026)
Papa_145W_50N	NPac	150	https://doi.org/10.3334/cdiac/otg.tsm_papa_145w_50n	Sutton et al. (2025b)
Polaris II	SOce	7	https://doi.org/10.25921/32pw-2808	van de Velde (2026)
Polarstern	Coas; SOce; TAtl; NAtl; Arct	168	https://doi.org/10.25921/y6qs-j872	Olivier et al. (2026)
Quadra Island Field Station	Coas	336	https://doi.org/10.21966/ea8w-bf35	Evans et al. (2025b)
Ryofu Maru III	Coas; NPac; TPac	73	https://doi.org/10.25921/hfs8-k876	Enyo and Kadono (2026)
S.A. Agulhas II	SOce	24	https://doi.org/10.25921/2yd3-vv23	Hamnca et al. (2026)
Sarmiento de Gamboa	SOce; Coas; NAtl	37	https://doi.org/10.25921/406n-yb48	Padin et al. (2026)
Sea-Cargo Express	Coas	147	https://doi.org/10.18160/7PQC-P96W	Omar et al. (2026)
Sikuliaq	TPac; Coas; NPac; Arct; SOce	203	https://doi.org/10.25921/nhdc-3328	Sweeny et al. (2026b)
Simon Stevin	Coas	156	https://doi.org/10.18160/RJKN-RTFU	Gkritzalis et al. (2026)
SOFS_142E_46S	SOce	91	https://doi.org/10.3334/cdiac/otg.tsm_sofs_142w_46s	Sutton et al. (2026b)
Tangaroa	SOce	95	https://doi.org/10.25921/72p3-9k79	van de Velde and Marriner (2026)
Thomas G. Thompson	TPac; Coas; Indi; SOce	76	https://doi.org/10.25921/texj-fc86	Alin et al. (2026b)
Trans Future 5	Coas; NPac; SOce; TPac	172	https://doi.org/10.25921/h5rp-2r03	Nakaoka et al. (2026b)
Tukuma Arctica	Coas; NAtl	174	https://doi.org/10.18160/6exv-xdsk	Olsen and Ehmen (2026)
Tysla	Coas; NAtl; TAtl; TPac; SOce	47	https://doi.org/10.25921/hr6b-p951	Alin et al. (2026d)
Victor Angelescu	SOce	151	https://doi.org/10.25921/fr55-fp38	Berghoff et al. (2026)

1347

1348

Table S9. Aircraft measurement programs archived by Cooperative Global Atmospheric Data Integration Project (Schuldt et al. 2024 and 2025) that contribute to the evaluation of the atmospheric inversions (Figure S14).

Site code	Measurement program name in Obspack	Specific doi	Data providers
AAO	Airborne Aerosol Observatory, Bondville, Illinois	https://doi.org/10.15138/39HR-9N34	Sweeney, C.;
ABOVE	Carbon in Arctic Reservoirs Vulnerability Experiment (CARVE)	https://doi.org/10.3334/ORNLDAAC/1404	Sweeney, C.; McKain, K.; Karion, A.; Miller, J.B.; Miller, C.E.
ACG	Alaska Coast Guard	https://doi.org/10.15138/39HR-9N34	McKain, K.; Karion, A.; Sweeney, C.
ACT	Atmospheric Carbon and Transport - America	https://doi.org/10.3334/ORNLDAAC/1593	Davis, K.J; DiGangi, J.P; Martin, M.Y;
AIRCORE NOAA	NOAA AirCore	https://doi.org/10.15138/6AV0-MY81	Sweeney, C.; Baier, B.
AJAX	Alpha Jet Atmospheric eXperiment (AJAX)	https://doi.org/10.5194/essd-15-2375-2023	Emma L. Yates;Laura T. Iraci;Susan S. Kulawik;Ju-Mee Ryoo;Josette E. Marrero;Caroline L. Parworth;Jason M. St. Clair;Thomas F. Hanisco;Thao Paul V. Bui;Cecilia S. Chang;Jonathan M. Dean-Day;
ALF	Alta Floresta	https://doi.org/10.1594/PANGAEA.949643	Gatti, L.V.; Gloor, E.; Miller, J.B.; Peters, W.
AOA	Aircraft Observation of Atmospheric trace gases by JMA	doi:10.5194/amt-6-1257-2013	Shinya Takatsuji
BGI	Bradgate, Iowa	https://doi.org/10.15138/39HR-9N34	Sweeney, C.;
BNE	Beaver Crossing, Nebraska	https://doi.org/10.15138/39HR-9N34	Sweeney, C.;
BRZ	Berezorechka, Russia		Motoki Sasakawa, Toshinobu Machida
CAR	Briggsdale, Colorado	https://doi.org/10.15138/39HR-9N34	McKain, K.; Sweeney, C.
CMA	Cape May, New Jersey	doi:10.1002/2014JD022591	McKain, K.; Sweeney, C.
CON	CONTRAIL (Comprehensive Observation Network for TRace gases by AIrLiner)	http://dx.doi.org/10.17595/20180208.001	Toshinobu Machida (NIES) AND Hidekazu Matsueda (MRI) AND Yosuke Niwa (NIES) AND Motoki Sasakawa (NIES)
CRV	Carbon in Arctic Reservoirs Vulnerability Experiment (CARVE)	https://doi.org/10.3334/ORNLDAAC/1404	Sweeney, C.; Karion, A.; Miller, J.B.; Miller, C.E.
DND	Dahlen, North Dakota	https://doi.org/10.15138/39HR-9N34	McKain, K.; Sweeney, C.
ECO	East Coast Outflow	https://doi.org/10.1029/2019GL082635	Sweeney, C.; McKain, K.
ESP	Estevan Point, British Columbia	https://doi.org/10.15138/39HR-9N34	McKain, K.; Sweeney, C.
ETL	East Trout Lake, Saskatchewan	https://doi.org/10.15138/39HR-9N34	McKain, K.; Sweeney, C.
FAM	FAAM Aircraft, UK		Xin Lan
FWI	Fairchild, Wisconsin	https://doi.org/10.15138/39HR-9N34	Sweeney, C.;
GSFC	NASA Goddard Space Flight Center Aircraft Campaign		Kawa, S.R.; Abshire, J.B.; Riris, H.
HAA	Molokai Island, Hawaii	https://doi.org/10.15138/39HR-9N34	Sweeney, C.;
HFM	Harvard University Aircraft Campaign	doi:10.1002/2014JD022591	Sweeney, C.;

HIL	Homer, Illinois	https://doi.org/10.15138/39HR-9N34	McKain, K.; Sweeney, C.
HIP	HIPPO (HIAPER Pole-to-Pole Observations)	https://doi.org/10.3334/CDIAC/HIPPO_010	Wofsy, S.C.; Stephens, B.B.; Elkins, J.W.; Hintsa, E.J.; Moore, F.
IAGOS-CARIBIC	In-service Aircraft for a Global Observing System	https://doi.org/10.5281/zenodo.10495597	Obersteiner, F.; Boenisch., H; Gehrlein, T.; Zahn, A.; Gerbig, C.; Schuck, T.
IAGOS-CORE	In-service Aircraft for a Global Observing System		Christoph Gerbig (Max-Planck-Institut für Biogeochemie, Jena)
SONGNEX2015	Shale Oil and Natural Gas Nexus 2015 (air campaign)		Thomas Ryerson;Jeff Peischl;Ken Aikin
INX	INFLUX (Indianapolis Flux Experiment)	doi:10.1002/2014JD022591	Sweeney, C.; Shepson, P.B.; Turnbull, J.
LEF	Park Falls, Wisconsin	https://doi.org/10.15138/39HR-9N34	McKain, K.; Sweeney, C.
MAN	Manaus, Brazil		Miller, J.B.; Martins, G.A.; de Souza, R.A.F.
NHA	Offshore Portsmouth, New Hampshire (Isles of Shoals)	https://doi.org/10.15138/39HR-9N34	McKain, K.; Sweeney, C.
NSA	North Slope, Alaska	doi:10.1002/2014JD022591	McKain, K.; Sweeney, C.; Biraud, S.C.
OIL	Oglesby, Illinois	https://doi.org/10.15138/39HR-9N34	Sweeney, C.;
ORC	ORCAS (O2/N2 Ratio and CO2 Airborne Southern Ocean Study)	https://doi.org/10.5065/D6SB445X	Stephens, B.B, Sweeney, C., McKain, K., Kort, E.
PFA	Poker Flat, Alaska	https://doi.org/10.15138/39HR-9N34	McKain, K.; Sweeney, C.
RBA-B	Rio Branco	https://doi.org/10.1594/PANGAEA.949643	Gatti, L.V.; Gloor, E.; Miller, J.B.; Peters, W.
RTA	Rarotonga	https://doi.org/10.15138/39HR-9N34	McKain, K.; Sweeney, C.
TOM	Atmospheric Tomography Mission (ATom)	doi: 10.5067/Aircraft/ATom/TraceGas_Aerosol_Global_Distribution	Kathryn McKain (NOAA) AND Colm Sweeney (NOAA) AND Steven C. Wofsy (HU) AND Bruce Daube (HU) AND Roisin Commane (HU)
KORUS-AQ	LARC - NASA Langley Research Center Aircraft Campaign		Gao Chen (NASA LaRC) AND Joshua P. DiGangi (NASA-LaRC) AND Michael Shook (NASA LaRC)
SAN	Santarem, Brazil	https://doi.org/10.1594/PANGAEA.949643	Gatti, L.V.; Gloor, E.; Miller, J.B.; Peters, W.
SCA	Charleston, South Carolina	https://doi.org/10.15138/39HR-9N34	Sweeney, C.; McKain, K.
SGP	Southern Great Plains, Oklahoma	https://doi.org/10.15138/39HR-9N34	Sweeney, C.; McKain, K.; Biraud, S.
TAB	Tabatinga	https://doi.org/10.1594/PANGAEA.949643	Gatti, L.V.; Gloor, E.; Miller, J.B.
TEF	Tefe	https://doi.org/10.1594/PANGAEA.949643	Gatti, L.V.; Gloor, E.; Miller, J.B.; Peters, W.
TGC	Offshore Corpus Christi, Texas	https://doi.org/10.15138/39HR-9N34	McKain, K.; Sweeney, C.
THD	Trinidad Head, California	https://doi.org/10.15138/39HR-9N34	McKain, K.; Sweeney, C.
UGD	Kajjansi Airfield, Kampala, Uganda	https://doi.org/10.15138/515F-N008	McKain, K; Sweeney, C
ULB	Ulaanbaatar, Mongolia	https://doi.org/10.15138/39HR-9N34	Sweeney, C.;
WBI	West Branch, Iowa	https://doi.org/10.15138/39HR-9N34	McKain, K.; Sweeney, C.

(a) Schuldt et al. 2025. Multi-laboratory compilation of atmospheric carbon dioxide data for the period 1957-2024; obspack_co2_1_GLOBALVIEWplus_v11.0_2026-01-12; NOAA Earth System Research Laboratory, Global Monitoring Laboratory. http://doi.org/10.25925/20250801.

(b) Schuldt et al. 2026. Multi-laboratory compilation of atmospheric carbon dioxide data for the period 2025-2026; obspack_co2_1_NRT_v11.0_2026-05-14; NOAA Earth System Research Laboratory, Global Monitoring Laboratory. http://doi.org/10.25925/20260430.

1349

1350

1351

Table S10. Main methodological changes in the global carbon budget since first publication. Methodological changes introduced in one year are kept for the following years unless noted. Empty cells mean there were no methodological changes introduced that year.

Publication year	Fossil fuel emissions			LUC emissions	Reservoirs			Uncertainty & other changes
	Global	Country (territorial)	Country (consumption)		Atmosphere	Ocean	Land	
2006 (a)		Split in regions						
2007 (b)				ELUC based on FAO-FRA 2005; constant ELUC for 2006	1959-1979 data from Mauna Loa; data after 1980 from global average	Based on one ocean model tuned to reproduced observed 1990s sink		±1σ provided for all components
2008 (c)				Constant ELUC for 2007				
2009 (d)		Split between Annex B and non-Annex B	Results from an independent study discussed	Fire-based emission anomalies used for 2006-2008		Based on four ocean models normalised to observations with constant delta	First use of five DGVMs to compare with budget residual	

2010 (e)	Projection for current year based on GDP	Emissions for top emitters		ELUC updated with FAO-FRA 2010				
2011 (f)			Split between Annex B and non-Annex B					
2012 (g)		129 countries from 1959	129 countries and regions from 1990-2010 based on GTAP8.0	ELUC for 1997-2011 includes interannual anomalies from fire-based emissions	All years from global average	Based on 5 ocean models normalised to observations with ratio	Ten DGVMs available for SLAND; First use of four models to compare with ELUC	
2013 (h)		250 countriesb	134 countries and regions 1990-2011 based on GTAP8.1, with detailed estimates for years 1997, 2001, 2004, and 2007	ELUC for 2012 estimated from 2001-2010 average		Based on six models compared with two data-products to year 2011	Coordinated DGVM experiments for SLAND and ELUC	Confidence levels; cumulative emissions; budget from 1750

2014 (i)	Three years of BP data	Three years of BP data	Extended to 2012 with updated GDP data	ELUC for 1997-2013 includes interannual anomalies from fire-based emissions		Based on seven models	Based on ten models	Inclusion of breakdown of the sinks in three latitude bands and comparison with three atmospheric inversions
2015 (j)	Projection for current year based Jan-Aug data	National emissions from UNFCCC extended to 2014 also provided	Detailed estimates introduced for 2011 based on GTAP9			Based on eight models	Based on ten models with assessment of minimum realism	The decadal uncertainty for the DGVM ensemble mean now uses ±1σ of the decadal spread across models
2016 (k)	Two years of BP data	Added three small countries; China's emissions from 1990 from BP data (this release only)		Preliminary ELUC using FRA-2015 shown for comparison; use of five DGVMs		Based on seven models	Based on fourteen models	Discussion of projection for full budget for current year

2017 (l)	Projection includes India-specific data			Average of two bookkeeping models; use of 12 DGVMs		Based on eight models that match the observed sink for the 1990s; no longer normalised	Based on 15 models that meet observation-based criteria (see Sect. 2.5)	Land multi-model average now used in main carbon budget, with the carbon imbalance presented separately; new table of key uncertainties
2018 (m)	Revision in cement emissions; Projection includes EU-specific data	Aggregation of overseas territories into governing nations for total of 213 countries a		Average of two bookkeeping models; use of 16 DGVMs	Use of four atmospheric inversions	Based on seven models	Based on 16 models; revised atmospheric forcing from CRUNCEP to CRUJRA	Introduction of metrics for evaluation of individual models using observations
2019 (n)	Global emissions calculated as sum of all countries plus bunkers, rather than taken directly from CDIAC.			Average of two bookkeeping models; use of 15 DGVMs	Use of three atmospheric inversions	Based on nine models	Based on 16 models	

2020 (o)	Cement carbonation now included in the EFOS estimate, reducing EFOS by about 0.2GtC yr-1 for the last decade	India's emissions from Andrew (2020: India); Corrections to Netherland Antilles and Aruba and Soviet emissions before 1950 as per Andrew (2020: CO2); China's coal emissions in 2019 derived from official statistics, emissions now shown for EU27 instead of EU28. Projection for 2020 based on assessment of four approaches.		Average of three bookkeeping models; use of 17 DGVMs. Estimate of gross land use sources and sinks provided	Use of six atmospheric inversions	Based on nine models. River flux revised and partitioned NH, Tropics, SH	Based on 17 models	
2021 (p)	Projections are no longer an assessment of four approaches.	Official data included for a number of additional countries, new estimates for South Korea, added emissions from lime production in China.		ELUC estimate compared to the estimates adopted in national GHG inventories		Average of means of eight models and means of seven data-products. Current year prediction of SOCEAN using a feed-forward neural network method	Current year prediction of SLAND using a feed-forward neural network method	

2022 (q)				ELUC provided at country level. Revised components decomposition of ELUC fluxes. Revision of LUC maps for Brazil. New datasets for peat drainage.	Use of nine atmospheric inversions	Average of means of ten models and means of seven data-products	Based on 16 models. Revision of LUC maps for Brazil.	
2023 (r)				Refined components decomposition of ELUC. Revision of LUC maps for Indonesia. Use of updated peat drainage estimates.	Use of 14 atmospheric inversions. Additional use of 4 Earth System Models to estimate current year CO2	Additional use of 4 Earth System Models and atmospheric oxygen method to assess SOCEAN. Regional distribution of river flux adjustment revised.	Based on 20 models. Additional use of 4 Earth System Models and atmospheric oxygen method to assess the net atmosphere-land flux.	Inclusion of an estimate of Carbon Dioxide Removal

2024 (s)	Inclusion of 2024 projections from Carbon Monitor	Inclusion of 2024 projections from Carbon Monitor for China, USA, EU27, India, and Rest of the World		Fourth bookkeeping estimate (LUCE). Update in land-use data (HYDE3.4) including revision of LUC maps for China. Updated definition of forest (re-)growth fluxes (consistent with 2nd State of CDR Report).	Use of 14 atmospheric inversions models	Use of 10 GOBMs, 8 fCO2-products. Added evaluation for fCO2-products.	Use of 20 DGVMs	
2025 (t)		Projection available for Japan for the first time		Bookkeeping estimates derived from models that estimate ELUC based on transient carbon densities responding to environmental changes (BLUE, OSCAR, LUCE).	Include an assessment of satellite-derived growth rates	Adjustments applied for known underestimation of GOBMs and cool surface skin effect in fCO2-products. Suspension of 19 ocean data sets from SOCAT.	Include the RSS adjustment.	

e Friedlingstein et al. (2010)
f Peters et al. (2012a)
g Le Quéré et al. (2013), Peters et al. (2013)
h Le Quéré et al. (2014)
i Le Quéré et al. (2015a)
j Le Quéré et al. (2015b)
k Le Quéré et al. (2016)
l Le Quéré et al. (2018a)
m Le Quéré et al. (2018b)
n Friedlingstein et al. (2019)
o Friedlingstein et al. (2020
p Friedlingstein et al. (2022a)

q Friedlingstein et al. (2022b)
r Friedlingstein et al. (2023)
s Friedlingstein et al. (2025a)
t Friedlingstein et al. (2026a)

1352
1353

Table S11: Translation of global carbon cycle models' land-use flux definition to the LULUCF flux definition used in national greenhouse gas inventory (NGHGI) reports submitted to UNFCCC. The translation is based on adding the natural land sink (SLAND) in managed forests estimated by dynamic global vegetation models (DGVMs) to ELUC estimates from bookkeeping models (BMs). Managed forests are approximated by non-intact forests, unless country-specific maps of managed forests are available. The component 'forest (GCB)' includes removals from permanent afforestation/reforestation, net fluxes from shifting cultivation in forests, and net fluxes from wood harvest. The component 'other transitions' includes all transitions between non-forested land (e.g., shrub and herbaceous vegetation), cropland, pasture, and urban areas. For comparison, we provide FAO estimates of emissions from net forest conversion and removals on forest land (based on carbon stock change), plus emissions from peat drainage and peat fires (based on IPCC Tier 1 emission factors), as well as the net land flux on managed land from atmospheric inversions (see Section S.2.4 for more details). The FAO net LULUCF flux estimate excludes the component "other transitions". NGHGI data are from the LULUCF datahub v4.1.0 (missing years are gap-filled) and FAO data are from Tubiello et al. (2026) and FAOSTAT (FAO, 2026b). Values are averages for 2016-2025, expressed in GtC yr^{-1}; positive values indicate emissions to the atmosphere, and negative values indicate removals.

		Bookkeeping models (and DGVMs for S_{LAND})	NGHGIs	FAO	Atmospheric inversions
Forest-related fluxes	(1) permanent deforestation	1.0	0.9	1.0	-
	(2) forest (GCB)	0.0	-	-	-
	(3) SLAND in managed forest (from DGVMs)	-2.2	-	-	-
	(4) forest (LULUCF) [2+3 for BMs]	-2.3	-2.1	-1.7	-
Net forest fluxes	(5) permanent deforestation + forest (LULUCF) [1+4]	-1.2	-1.2	-0.6	-
Other fluxes	(6) other transitions	0.1	-0.2	-	-
	(7) peat fire & drainage	0.2	0.2	0.3	-
Total fluxes	(8) net E_{LUC} (GCB) [1+2+6+7]	1.3	-	-	-
	(9) net LULUCF flux [1+4+6+7]	-0.9	-1.2	-0.4	-0.9

1371

Table S12 - Evaluation of global ocean biogeochemistry models based on comparison with observation-based interior ocean carbon accumulation and process-based evaluation metrics for Atlantic Meridional Overturning Circulation (AMOC), Southern Ocean sea surface salinity and surface ocean Revelle factor (following the RECCAP2 ocean model evaluation chapter, Terhaar et al., 2024) and Southern Ocean stratification index (Bourgeois et al., 2022). "full coverage" refers to full model domain coverage and published dataset including scaling factors. "reduced coverage" refers to models subsampled to horizontal and vertical coverage of the data set (e.g., restricted to 3000 m depth). See supplementary text C3.3 for details of calculation and observational data sources.

		Global Ocean Biogeochemistry Models											
Metric	**Observations**	ACCESS (CSIRO)	CESM-ETHZ	FESOM 2.7-REcoM	MOM6-Cobalt (Princeton)	MPIOM-HAMOCC6	MRI-ESM2-3	NEMO-PISCES (IPSL)	NEMO-PlankTOM12	NEMO-PISCES v2-gas (CNRM)	NorESM-OC1.2	**ensemble average**	**ensemble standard deviation**
Interior ocean anthropogenic carbon accumulation in GtC													
Global (1994-2007, Gruber et al., 2019)	33.8 ± 4.0	34.9	26.9	25.6	30.2	19.9	27.9	32.6	26.8	28.4	33.4	28.7	4.4
Global, full coverage (1994-2004, Müller et al., 2023)	29.3 ± 2.5	25.5	19.2	18.4	22.1	15.3	20.5	24.1	20.2	20.7	24.7	21.1	3.1
Global, reduced coverage (1994-2004, Müller et al., 2023)	27.4	24.4	18.1	17.5	20.7	10.9	18.5	22.1	18.6	19.9	22.7	19.3	3.7
North, reduced coverage (1994-2004, Müller et al., 2023)	3.4	3.8	3.1	2.7	3.8	1.1	2.9	3.5	2.4	3.1	3.9	3.0	0.8
Tropics, reduced coverage (1994-2004, Müller et al., 2023)	13.4	11.1	9.0	8.9	10.2	5.5	8.9	11.1	9.7	10.3	9.5	9.4	1.6
South, reduced coverage (1994-2004, Müller et al., 2023)	10.6	9.5	6.1	5.8	6.7	4.3	6.8	7.5	6.6	6.5	9.3	6.9	1.6
Global, full coverage (2004-2014, Müller et al., 2023)	27.3 ± 2.5	30.2	23.3	22.0	26.2	18.5	24.0	28.1	23.8	24.8	28.4	24.9	3.4
Global, reduced coverage (2004-2014, Müller et al., 2023)	25.6	28.2	21	20.2	24.6	14.1	21.4	25.7	22.2	23.4	26.4	22.7	4.0
North, reduced coverage (2004-2014, Müller et al., 2023)	2.2	4.2	3.5	3.4	4.6	1.7	3.3	4.0	3.1	3.9	4.7	3.6	0.9
Tropics, reduced coverage (2004-2014, Müller et al., 2023)	14.4	12.8	10.2	10.1	11.4	6.2	10.3	12.6	11.1	11.7	11.0	10.7	1.8

South, reduced coverage (2004-2014, Müller et al., 2023)	9.1	11.2	7.2	6.8	8.7	6.3	7.8	9.0	8.0	7.8	10.6	8.3	1.6
Atlantic Meridional Overturning Circulation at 26°N, 2005-2023 in Sv (Moat et al., 2025)	*16.9 ± 0.8*	9.4	13.8	11.0	12.9	15.5	13.2	13.2	7.0	13.8	22.8	13.3	4.2
Southern Ocean sea surface salinity 2005-2025 in psu (Good et al., 2013)													
subpolar seasonally stratified biome (SPSS)	33.943	34.183	33.826	33.786	34.001	33.927	34.059	34.192	33.957	33.972	34.117	34.002	0.138
subpolar seasonally stratified and subtropical seasonally stratified biomes (SPSS+STSS)	34.309	34.512	34.265	34.068	34.394	34.394	34.393	34.545	34.321	34.277	34.478	34.365	0.140
Southern Ocean stratification index 2005-2025, in kg m-3 (Bourgeois et al., 2022, Good et al., 2013)	5.88	5.49	6.16	5.83	5.90	5.96	5.98	5.53	4.93	6.20	5.76	5.77	0.38
Surface ocean Revelle factor													
1997-2007, unitless (GLODAPv2.2016, Lauvset et al., 2016)	10.48	10.60	10.06	10.80	10.62	10.71	10.56	10.68	10.42	10.69	10.55	10.57	0.21
2005-2022, unitless (OceanSODA_v2023, updated from Gregor and Gruber, 2021)	10.80	10.78	10.20	10.99	10.79	10.88	10.74	10.84	10.56	10.85	10.73	10.74	0.22

1372
1373
1374
1375
1376
1377

Table S13. Global ocean sink of the ten GOBMs (GtC yr^{-1}) for different periods according to the emergent constraint: unconstrained multi-model mean ± one standard deviation, and constrained with the three-predictor emergent constraint using either all models or all models but ACCESS. R^2 is the fraction of the inter-model spread explained by the regression. The predictors are the same for all periods.

Period	Unconstrained	All models	R^2	Without ACCESS	R^2
1960-1969	1.06 ± 0.16	1.10 ± 0.13	0.62	1.11 ± 0.13	0.67
1970-1979	1.34 ± 0.19	1.38 ± 0.16	0.63	1.41 ± 0.13	0.79
1980-1989	1.73 ± 0.23	1.73 ± 0.19	0.65	1.76 ± 0.11	0.86
1990-1999	1.96 ± 0.23	1.93 ± 0.17	0.7	1.96 ± 0.09	0.9
2000-2009	2.17 ± 0.25	2.15 ± 0.23	0.58	2.19 ± 0.07	0.95
2010-2019	2.53 ± 0.27	2.48 ± 0.21	0.67	2.51 ± 0.08	0.94
2016-2025	2.67 ± 0.30	2.60 ± 0.22	0.7	2.64 ± 0.11	0.9
1990-2025	2.30 ± 0.26	2.26 ± 0.21	0.66	2.30 ± 0.08	0.93

Table S14 - Mean ocean CO_2 fluxes from surface ocean fCO_2-products and atmospheric inversions over the period 2016-2025, before (net air-sea flux) and after (S_{OCEAN}) applying corrections for pre-industrial riverine carbon fluxes (PI Rivers) and pre-industrial natural steady state ocean CO_2 fluxes that are regionally different from zero (PI natural steady state). The riverine correction and the PI natural steady state corrections are subtracted. The latter is applied only to regional estimates, as its global integral is zero. All values are expressed in GtC yr^{-1}, with positive values indicating ocean CO_2 uptake. Uncertainties represent ±1σ. For the reported estimates, uncertainties associated with the PI natural steady state correction are combined in quadrature with the original flux uncertainties. For atmospheric inversions, uncertainties are calculated as the standard deviation across the decadal means of individual inversion models. For fCO_2-based products, the global uncertainty includes both random (model ensemble spread) and systematic uncertainties, whereas regional uncertainties include only random uncertainties (see Supplement S3.5).

Region	Corrections		fCO_2-products		Atmospheric Inversions	
	PI Rivers	PI natural steady state	Net air-sea flux	S_{OCEAN}	Net air-sea flux	S_{OCEAN}
Global	-0.65	0	2.60 ± 0.58	3.25 ± 0.58	2.45 ± 0.25	3.10 ± 0.25
North	-0.14	0.71 ± 0.14	1.20 ± 0.11	0.63 ± 0.18	1.06 ± 0.11	0.49 ± 0.18
Tropics	-0.42	-1.07 ± 0.25	-0.18 ± 0.10	1.31 ± 0.27	−0.12 ± 0.12	1.37 ± 0.28
South	-0.09	0.38 ± 0.22	1.57 ± 0.22	1.28 ± 0.31	1.51 ± 0.20	1.22 ± 0.30

Supplementary figures

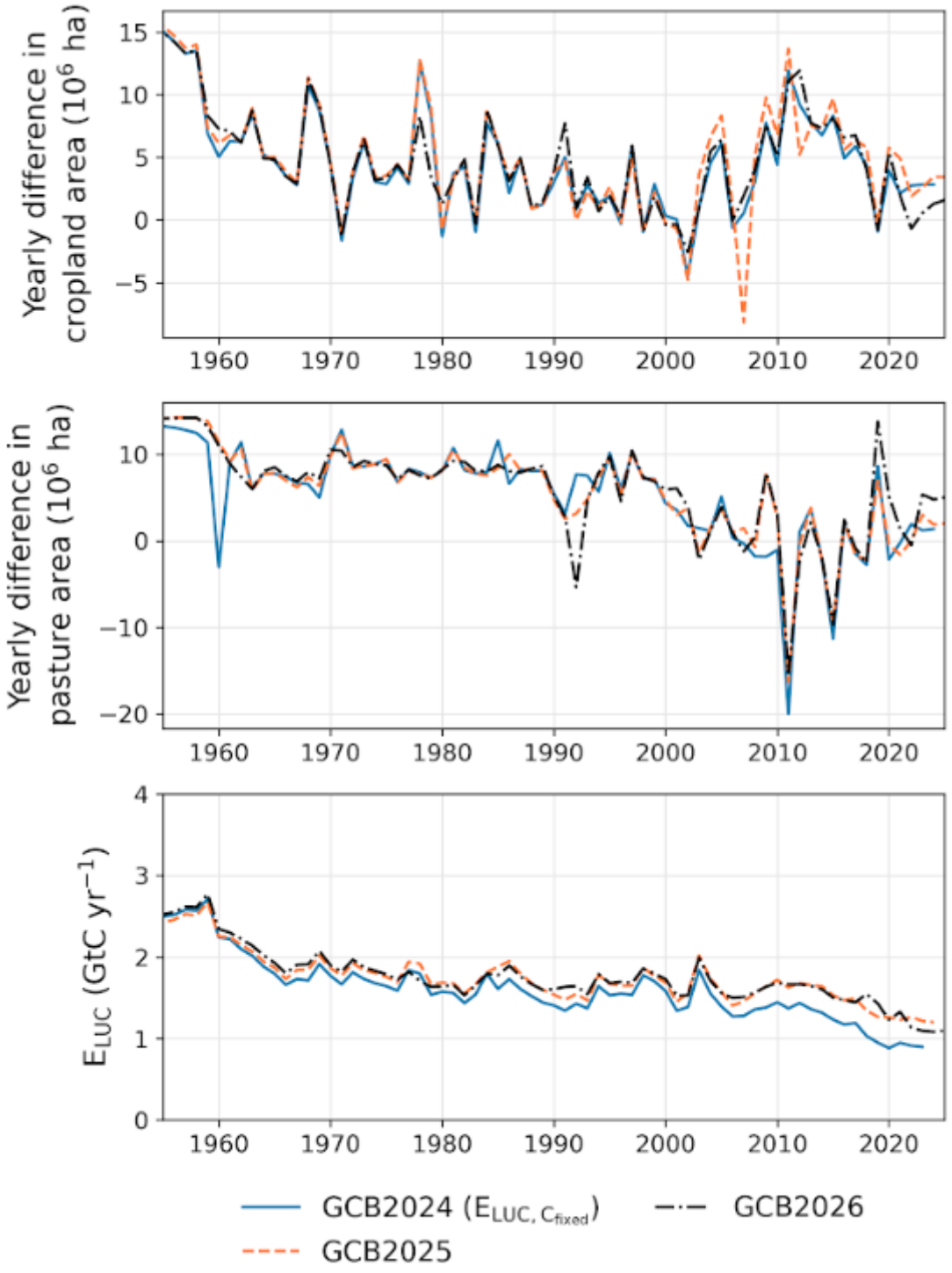


Figure S1. Differences in the HYDE/LUH2 land-use forcing used for the global carbon budgets GCB2024 (Friedlingstein et al., 2025a), GCB2025 (Friedlingstein et al., 2026a), and GCB2026 (this paper). Shown are year-to-year changes in cropland area (top panel) and pasture area (middle panel). To illustrate the relevance of the update in the land-use forcing for the recent trends in E_{LUC}, the bottom panel shows the land-use emission

estimate from the bookkeeping model BLUE (original model output, i.e., excluding emissions from peat fire and peat drainage). The inclusion of transient carbon densities in GCB2026 is also shown on the bottom panel.

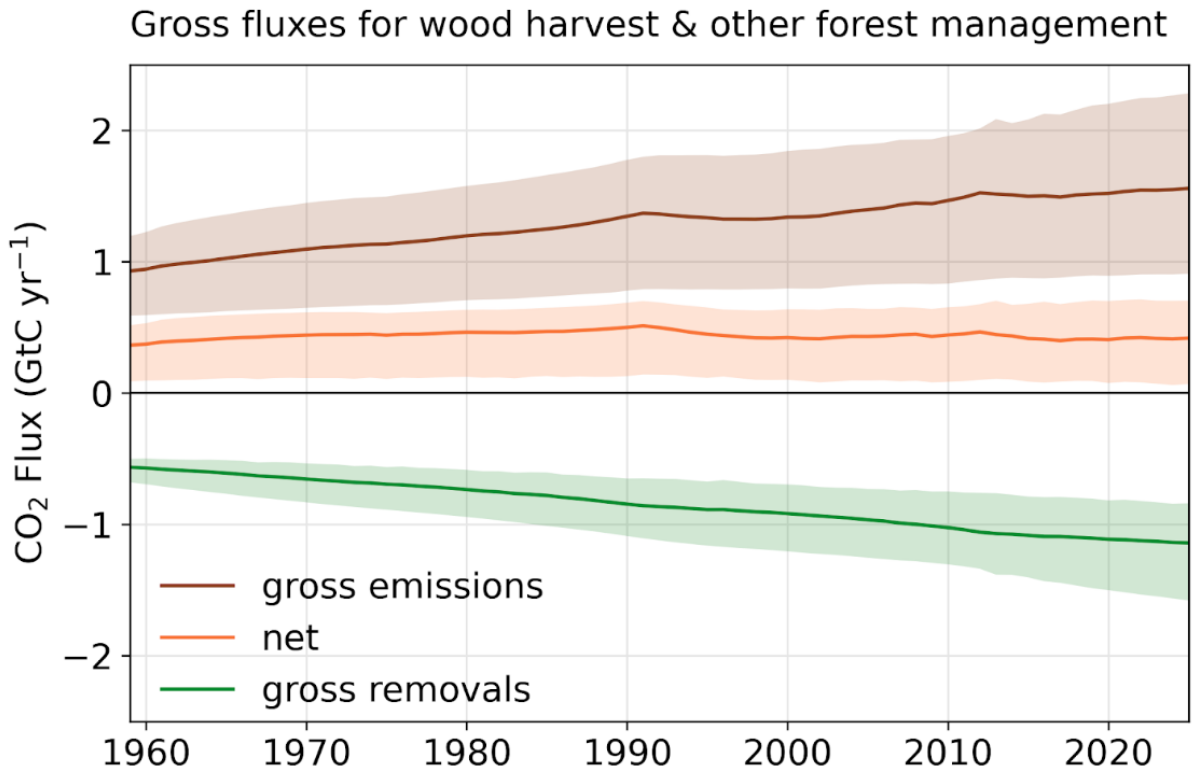


Figure S2. Split of net CO_2 fluxes from wood harvest and other forest management into gross emissions and gross removals. Solid lines denote the average of the three bookkeeping models and shaded areas the full range (min-max) of the bookkeeping model estimates. Gross wood harvest emissions amount to 1.5 [0.9, 2.2] GtC yr^{-1} in 2016–2025 resulting from the decomposition of slash and the decay of wood products. Gross removals amount to −1.1 [−1.5, −0.8] GtC yr^{-1} in 2016-2025 resulting from regrowth after wood harvesting.

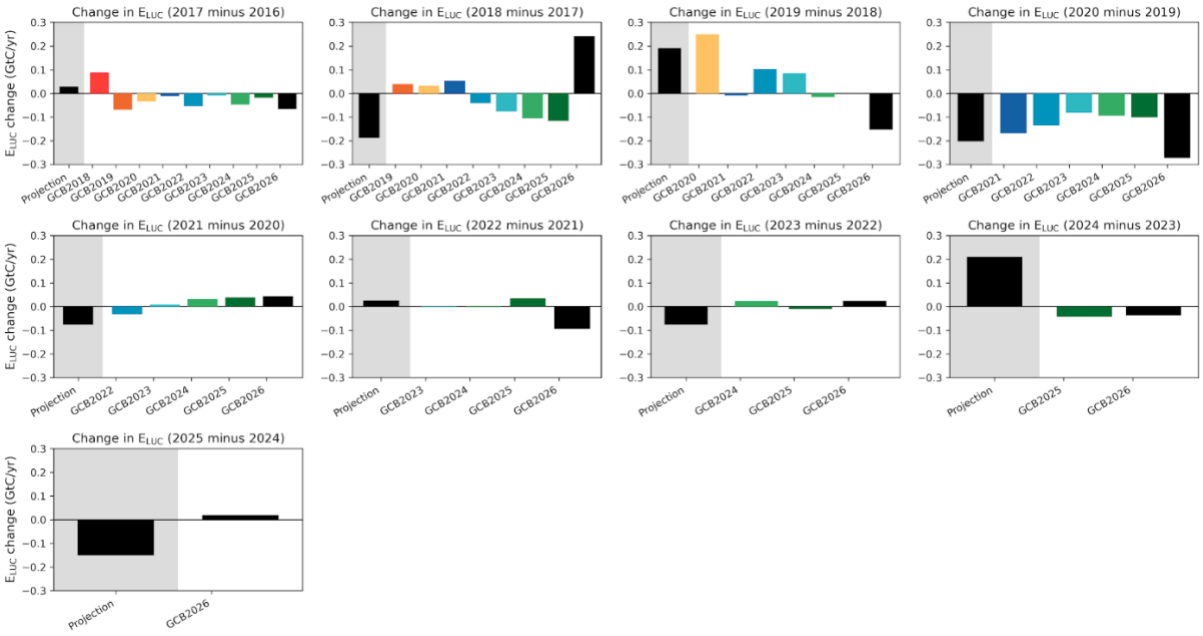


Figure S3. Comparison of initial E_{LUC} projections (E_{LUC} changes relative to the E_{LUC} estimate in the previous year) based on anomalies in peat fires in equatorial Asia and tropical deforestation and degradation fires with updated estimates in later global carbon budgets (GCBs) based on bookkeeping model simulations. Black bars on gray background indicate E_{LUC} projections; colored bars indicate bookkeeping E_{LUC} estimates from later GCB versions (with the GCB2026 bookkeeping E_{LUC} estimate in black).

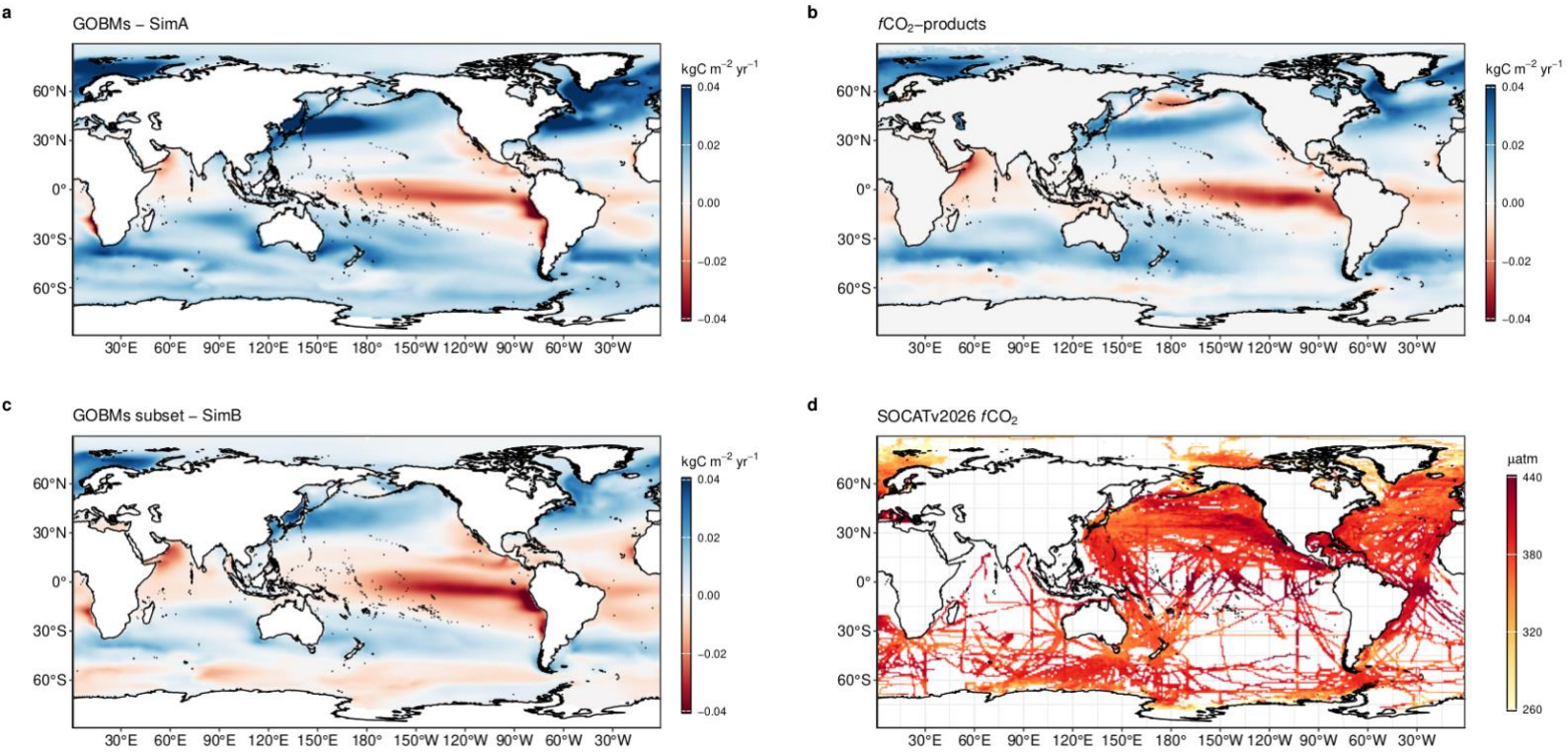
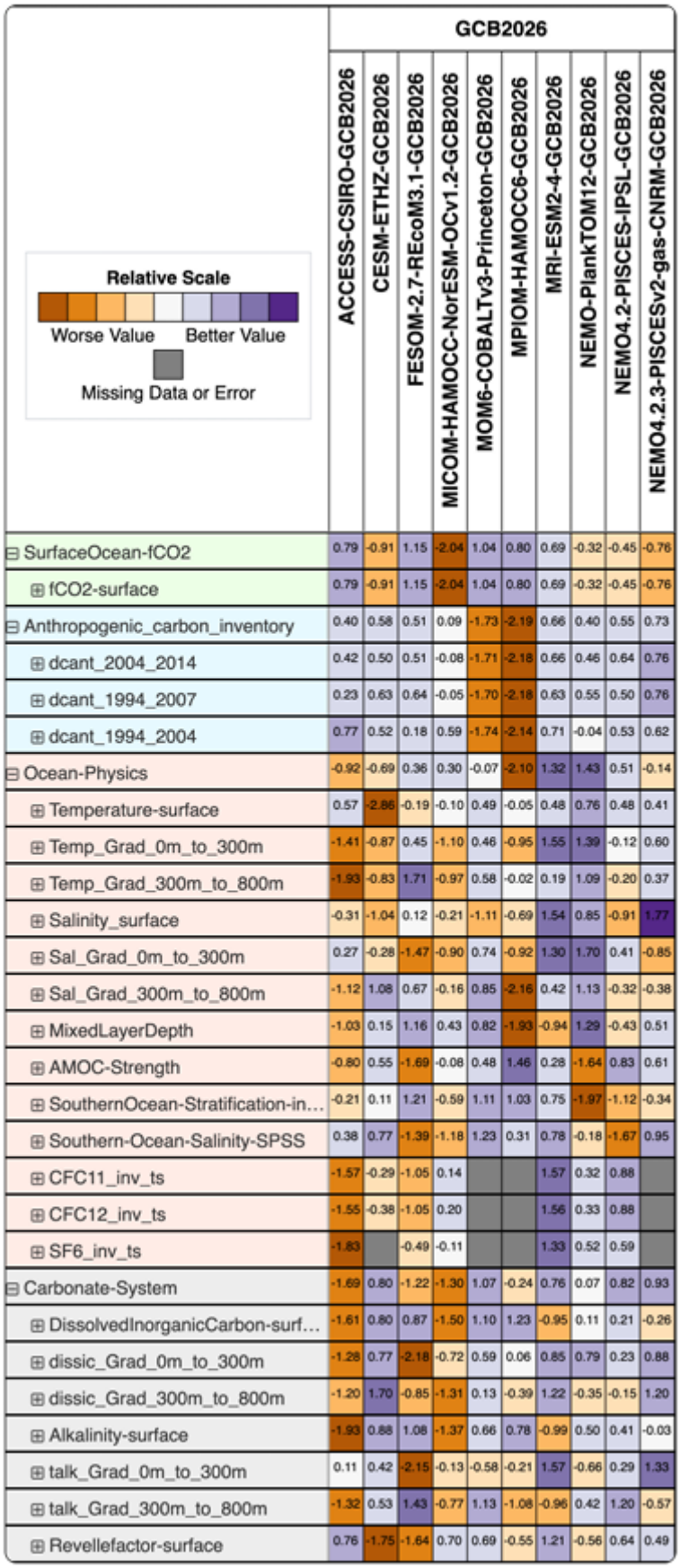


Figure S4. Ensemble mean air-sea CO_2 flux from a) global ocean biogeochemistry models (GOBMs) simulation A, b) fCO_2 based data products, and c) GOBMs simulation B, averaged over 2016-2025 period (kgC m^{-2} yr^{-1}). In panel c, only the six models that do not account for riverine outgassing (i.e. their simulation B represents the natural steady-state fluxes and that have a simulation B CO2 flux within ± 0.2 GtC yr-1) are shown (see section S.3.1). This map (along with river outgassing correction outlined in section 2.5.1 in the main manuscript) is used to calculate S_{OCEAN} estimates from the original net air-sea exchange for the $fCO2$-products and atmospheric inversions. Positive numbers indicate a flux into the ocean. d) gridded SOCATv2026 fCO_2 measurements, averaged over the 2016-2025 period (µatm). The fCO_2-products represent the contemporary flux, i.e. including outgassing of riverine carbon and natural steady-state fluxes.



	GCB2026									
	ACCESS-CSIRO-GCB2026	CESM-ETHZ-GCB2026	FESOM-2.7-REcoM3.1-GCB2026	MICOM-HAMOCC-NorESM-OCv1.2-GCB2026	MOM6-COBALTv3-Princeton-GCB2026	MPIOM-HAMOCC6-GCB2026	MRI-ESM2-4-GCB2026	NEMO-PlankTOM12-GCB2026	NEMO4.2-PISCES-IPSL-GCB2026	NEMO4.2.3-PISCESv2-gas-CNRM-GCB2026
⊟ SurfaceOcean-fCO2	0.79	-0.91	1.15	-2.04	1.04	0.80	0.69	-0.32	-0.45	-0.76
⊞ fCO2-surface	0.79	-0.91	1.15	-2.04	1.04	0.80	0.69	-0.32	-0.45	-0.76
⊟ Anthropogenic_carbon_inventory	0.40	0.58	0.51	0.09	-1.73	-2.19	0.66	0.40	0.55	0.73
⊞ dcant_2004_2014	0.42	0.50	0.51	-0.08	-1.71	-2.18	0.66	0.46	0.64	0.76
⊞ dcant_1994_2007	0.23	0.63	0.64	-0.05	-1.70	-2.18	0.63	0.55	0.50	0.76
⊞ dcant_1994_2004	0.77	0.52	0.18	0.59	-1.74	-2.14	0.71	-0.04	0.53	0.62
⊟ Ocean-Physics	-0.92	-0.69	0.36	0.30	-0.07	-2.10	1.32	1.43	0.51	-0.14
⊞ Temperature-surface	0.57	-2.86	-0.19	-0.10	0.49	-0.05	0.48	0.76	0.48	0.41
⊞ Temp_Grad_0m_to_300m	-1.41	-0.87	0.45	-1.10	0.46	-0.95	1.55	1.39	-0.12	0.60
⊞ Temp_Grad_300m_to_800m	-1.93	-0.83	1.71	-0.97	0.58	-0.02	0.19	1.09	-0.20	0.37
⊞ Salinity_surface	-0.31	-1.04	0.12	-0.21	-1.11	-0.69	1.54	0.85	-0.91	1.77
⊞ Sal_Grad_0m_to_300m	0.27	-0.28	-1.47	-0.90	0.74	-0.92	1.30	1.70	0.41	-0.85
⊞ Sal_Grad_300m_to_800m	-1.12	1.08	0.67	-0.16	0.85	-2.16	0.42	1.13	-0.32	-0.38
⊞ MixedLayerDepth	-1.03	0.15	1.16	0.43	0.82	-1.93	-0.94	1.29	-0.43	0.51
⊞ AMOC-Strength	-0.80	0.55	-1.69	-0.08	0.48	1.46	0.28	-1.64	0.83	0.61
⊞ SouthernOcean-Stratification-in…	-0.21	0.11	1.21	-0.59	1.11	1.03	0.75	-1.97	-1.12	-0.34
⊞ Southern-Ocean-Salinity-SPSS	0.38	0.77	-1.39	-1.18	1.23	0.31	0.78	-0.18	-1.67	0.95
⊞ CFC11_inv_ts	-1.57	-0.29	-1.05	0.14			1.57	0.32	0.88	
⊞ CFC12_inv_ts	-1.55	-0.38	-1.05	0.20			1.56	0.33	0.88	
⊞ SF6_inv_ts	-1.83		-0.49	-0.11			1.33	0.52	0.59	
⊟ Carbonate-System	-1.69	0.80	-1.22	-1.30	1.07	-0.24	0.76	0.07	0.82	0.93
⊞ DissolvedInorganicCarbon-surf…	-1.61	0.80	0.87	-1.50	1.10	1.23	-0.95	0.11	0.21	-0.26
⊞ dissic_Grad_0m_to_300m	-1.28	0.77	-2.18	-0.72	0.59	0.06	0.85	0.79	0.23	0.88
⊞ dissic_Grad_300m_to_800m	-1.20	1.70	-0.85	-1.31	0.13	-0.39	1.22	-0.35	-0.15	1.20
⊞ Alkalinity-surface	-1.93	0.88	1.08	-1.37	0.66	0.78	-0.99	0.50	0.41	-0.03
⊞ talk_Grad_0m_to_300m	0.11	0.42	-2.15	-0.13	-0.58	-0.21	1.57	-0.66	0.29	1.33
⊞ talk_Grad_300m_to_800m	-1.32	0.53	1.43	-0.77	1.13	-1.08	-0.96	0.42	1.20	-0.57
⊞ Revellefactor-surface	0.76	-1.75	-1.64	0.70	0.69	-0.55	1.21	-0.56	0.64	0.49

Figure S5. Evaluation of the GOBMs using the IOMB scheme considering physical (sea surface temperature, sea surface salinity, mixed layer depth, Southern Ocean stratification index, Southern Ocean subpolar biome surface salinity, and Atlantic Meridional Overturning Circulation (AMOC), transient tracers CFC-11, CFC-12, and SF6) and biogeochemical variables (surface dissolved inorganic carbon, alkalinity, Revelle factor and CO_2 fugacity (fCO_2), anthropogenic carbon inventory). See section S3.3 for observational data sets and statistical metrics included.

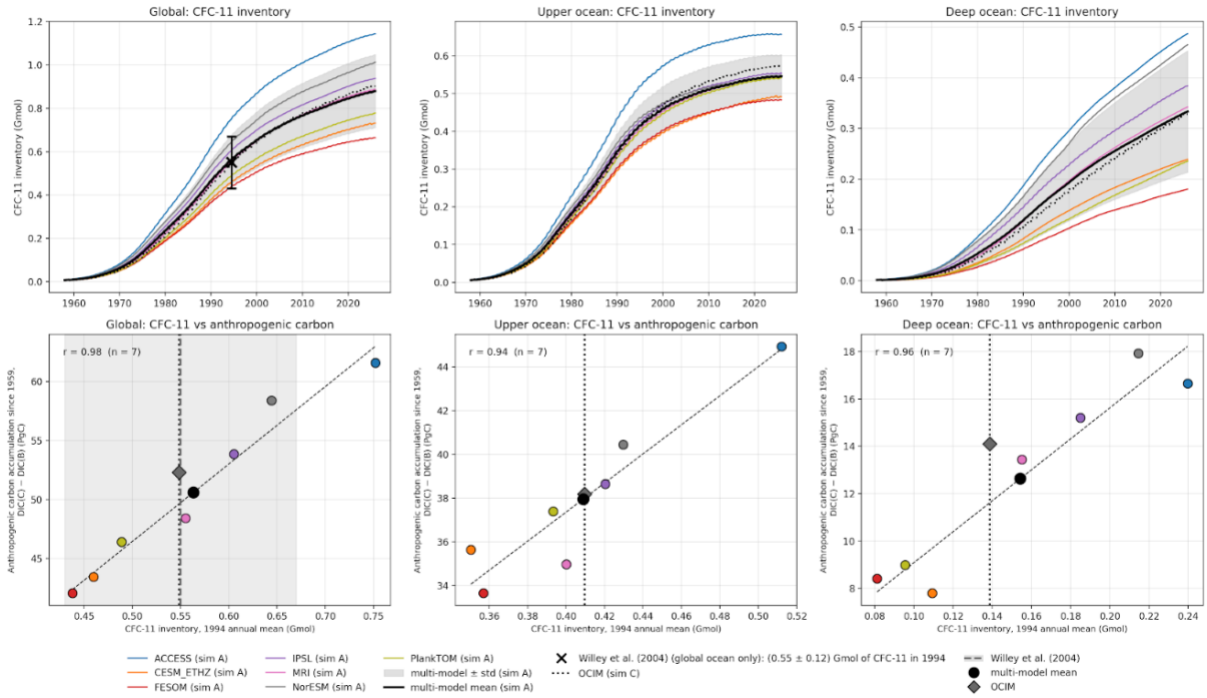


Figure S6: Inventory of transient tracer CFC-11 as simulated by seven out of ten global ocean biogeochemistry models. Upper row: Temporal evolution of the CFC-11 inventory from simulation A (upper row) for the global ocean (left), the upper ocean (centre, $\sigma_0 < 27.5$ kg m^3) and the deep ocean (right, $\sigma_0 > 27.5$ kg m^3). The cross shows the observation-based estimate for the year 1994 (Willey et al., 2004), and the dotted line shows the estimate from the ocean inverse model OCIM simulation C with steady circulation (no climate change). Lower row: The anthropogenic carbon accumulation since 1959 (simulation C minus simulation B, only direct CO_2 effect, no climate change) in 1994 scales with the CFC inventory of the same year for the global (left), upper (centre) and deep (right) ocean. The vertical dashed grey line and shading indicate Willey et al. (2004) estimate and uncertainty, the black dotted line and grey diamond indicate the OCIM estimate. The diagonal dashed black line is a least squares linear fit to the seven GOBMs and the correlation coefficient is indicated in the upper left corner.

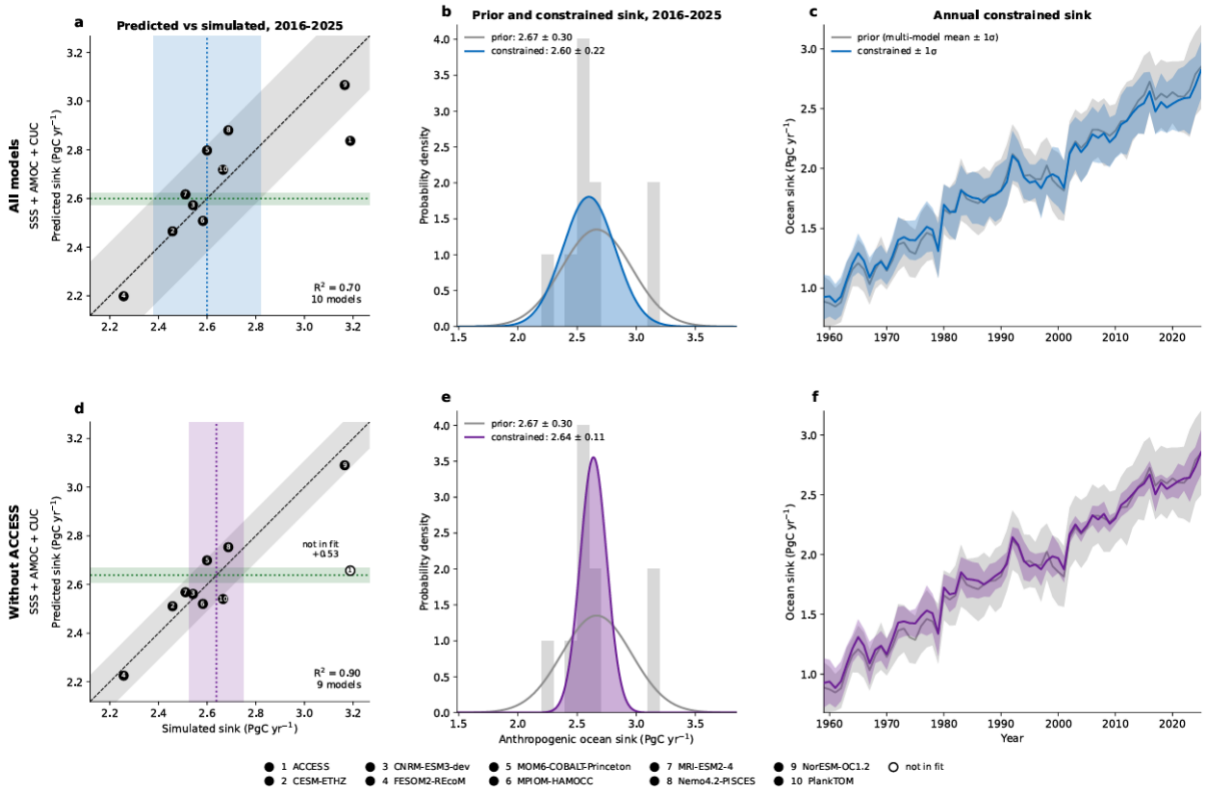


Figure S7. Emergent constraint on the global ocean carbon sink of the GOBMs using inter-frontal Southern Ocean surface salinity (SSS), the AMOC at 26.5°N and the carbon uptake capacity (CUC) as predictors, for all ten models (a-c) and excluding ACCESS (d-f). (a, d) Sink predicted by the regression against the simulated sink, 2016-2025. Black circles show the models used in the fit, numbered as in the legend; the open circle in (d) shows ACCESS, which is not used in the fit. The dashed line is the 1:1 line and the grey band the model uncertainty of the fit. The green dotted line and shading show the sink predicted from the observed predictors and its observational uncertainty; the coloured dotted line and shading show the constrained sink and its total uncertainty. (b, e) Prior (grey; multi-model mean ± 1σ, with a histogram of the individual models) and constrained (coloured) distributions of the sink, 2016-2025. (c, f) Annual multi-model mean ± 1σ (grey) and constrained sink ± 1σ (coloured), with the constraint applied separately to each year. All uncertainties are one standard deviation.

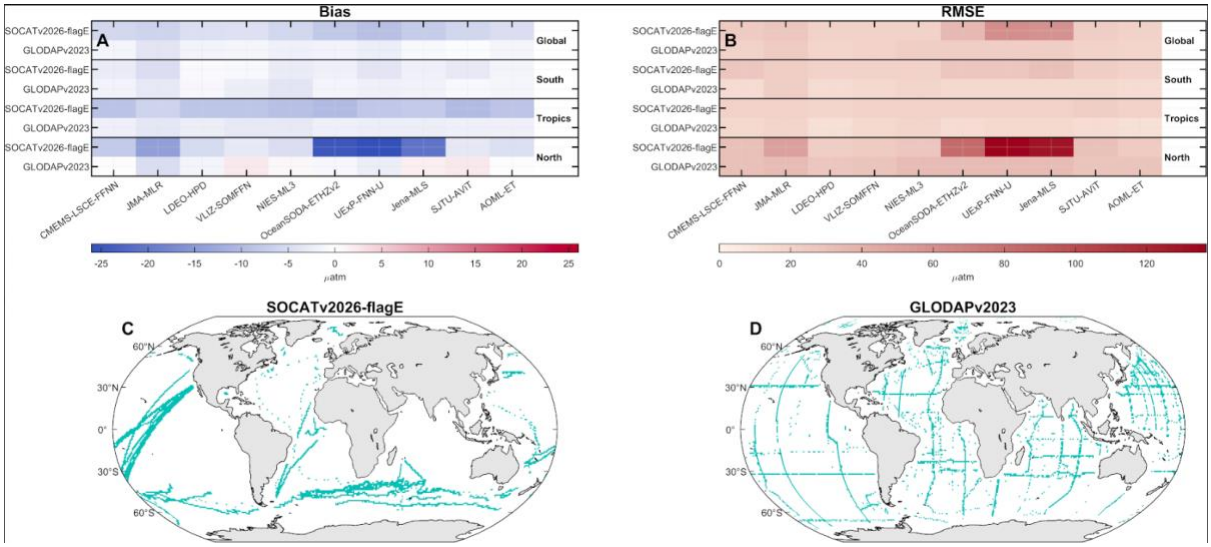


Figure S8: Bias (a) and RMSE (b) between independent observations from the SOCAT flag E and GLODAPv2 datasets with 9 fCO_2-products included in the global carbon budget. Panels C and D show the location of the observations in the global ocean

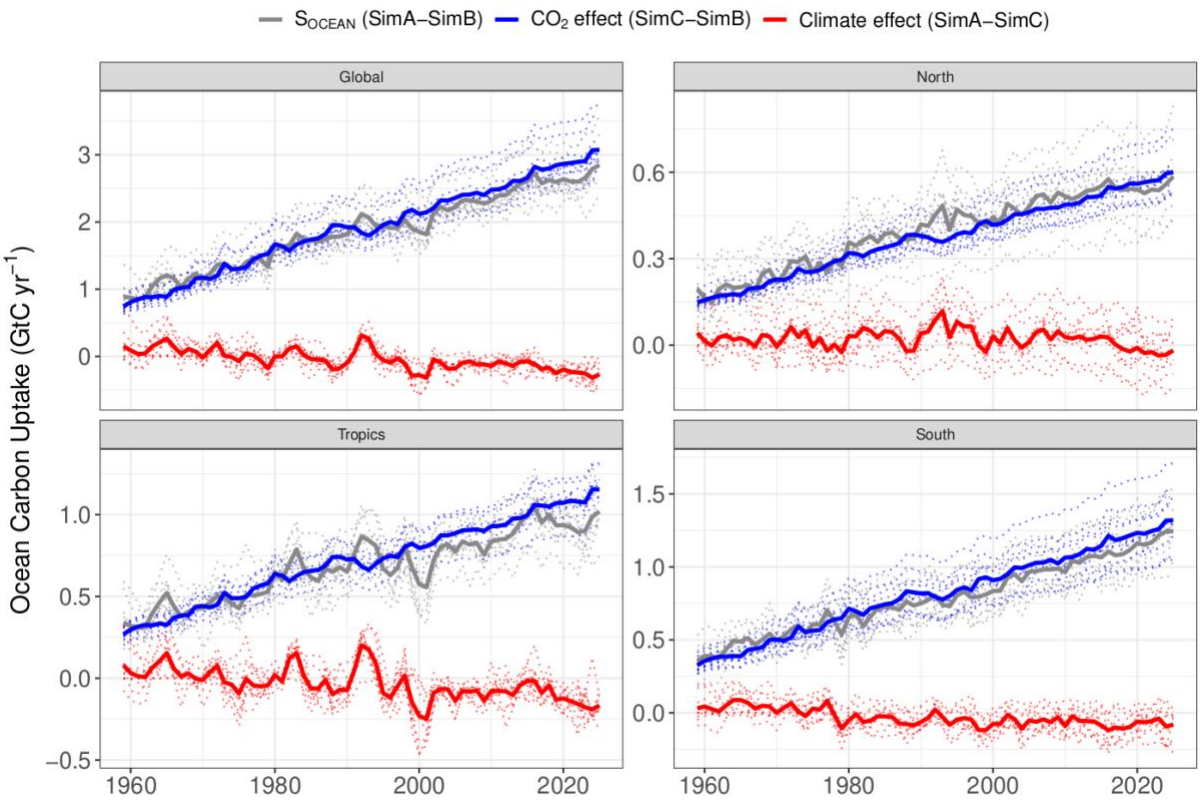


Figure S9 Time-series of CO_2 and climate effects on the S_{OCEAN} in the global ocean, and three latitudinal bands (north, tropics, south) as indicated in the panels. Dotted lines show individual global ocean biogeochemistry models and solid lines indicate the ensemble mean. The grey line shows the S_{OCEAN} flux (simulation A minus simulation B). The CO_2 and climate effects are calculated from simulation C minus B and A minus C, respectively. See section S3.2 on GOBM simulations.

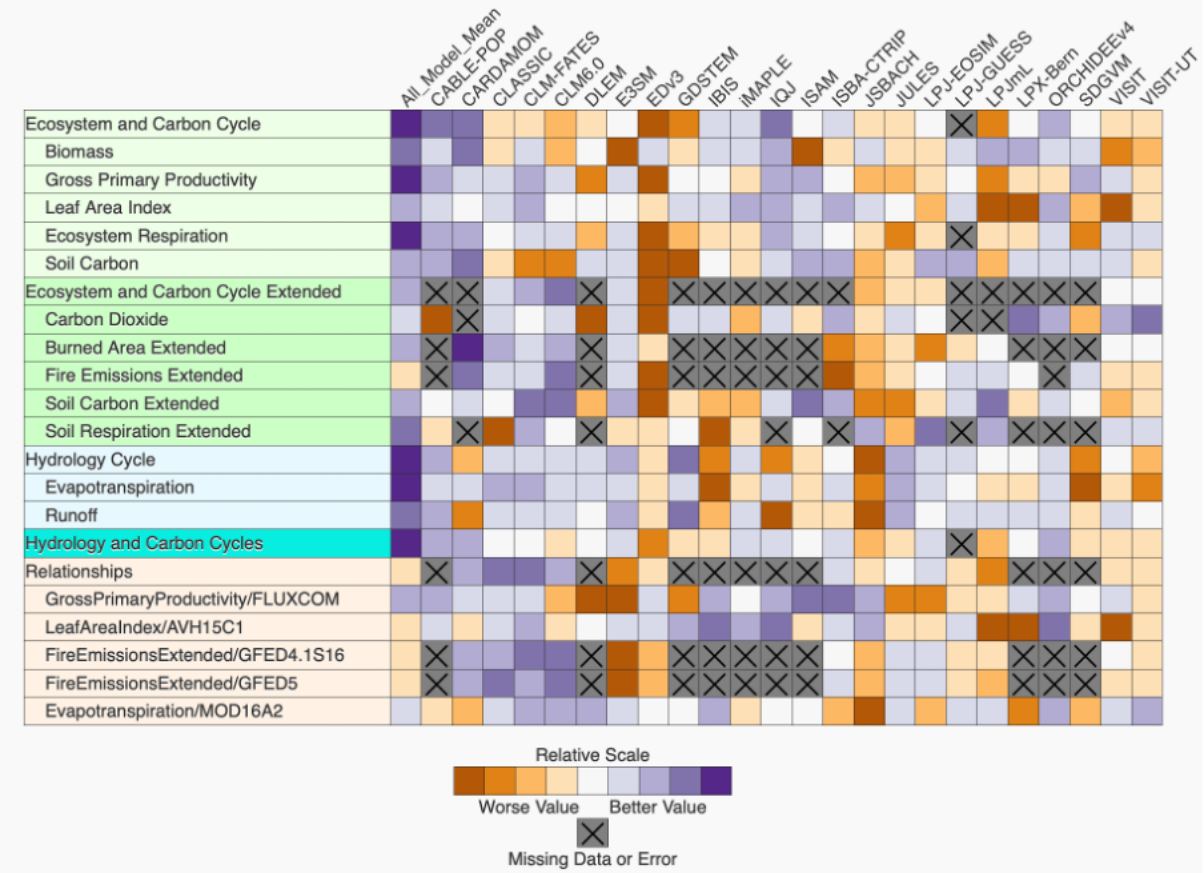


Figure S10. Evaluation of the DGVMs using the International Land Model Benchmarking system (ILAMB; Collier et al., 2018). Skill scores relative to other models. The benchmarking is done with observations for vegetation biomass (Santoro and Cartus, 2021; Saatchi et al., 2011; Thurner et al. 2014; Santoro et al. 2024; Xu et al., 2021; Dubayah et al., 2022), GPP and ecosystem respiration (Reichstein et al., 2007; Lasslop et al., 2010; Knauer et al., 2018; Jung et al., 2017; Tramontana et al., 2016; Alemohammad et al., 2017), leaf area index (Vermote, 2019; Claverie et al., 2016; De Kauwe et al., 2011; Myneni et al., 1997), soil carbon (Hugelius et al., 2013; Fischer et al., 2008), soil respiration (Tang et al., 2019, 2020; Raich et al., 2002; Hashimoto et al., 2015; Hashimoto et al., 2023), carbon dioxide (Dlugokencky et al., 2013; Liptak et al., 2017), burned area and fire emissions (Chen et al., 2023), evapotranspiration (De Kauwe et al., 2011; Martens et al., 2017; Miralles et al., 2011; Mu et al., 2011), and runoff (Dai and Trenberth, 2002; Hobeichi et al., 2019; Hobeichi et al., 2020). Metrics include relationships between carbon cycle variables, precipitation (Adler et al., 2003) and temperature (Harris et al., 2014). For each model–observation comparison a series of error metrics are calculated, scores are then calculated as an exponential function of each error metric, and finally for each variable the multiple scores from different metrics and observational datasets are combined to give the overall variable scores. Overall variable scores increase from 0 to 1 with improvements in model performance. The All_Model_Mean does not include CARDAMOM. The set of error metrics vary with dataset and can include metrics based on the period mean, bias, root mean squared error, spatial distribution, interannual variability, and seasonal cycle. The relative skill score shown is a Z score, which indicates in units of standard deviation the model scores relative to the mean score for a given variable. The overall score is given in the row 'Hydrology and Carbon Cycles', which represents a weighted average of the 'Hydrology Cycle' score and the 'Ecosystem and Carbon Cycle' score. Grey boxes with x's represent missing model data.

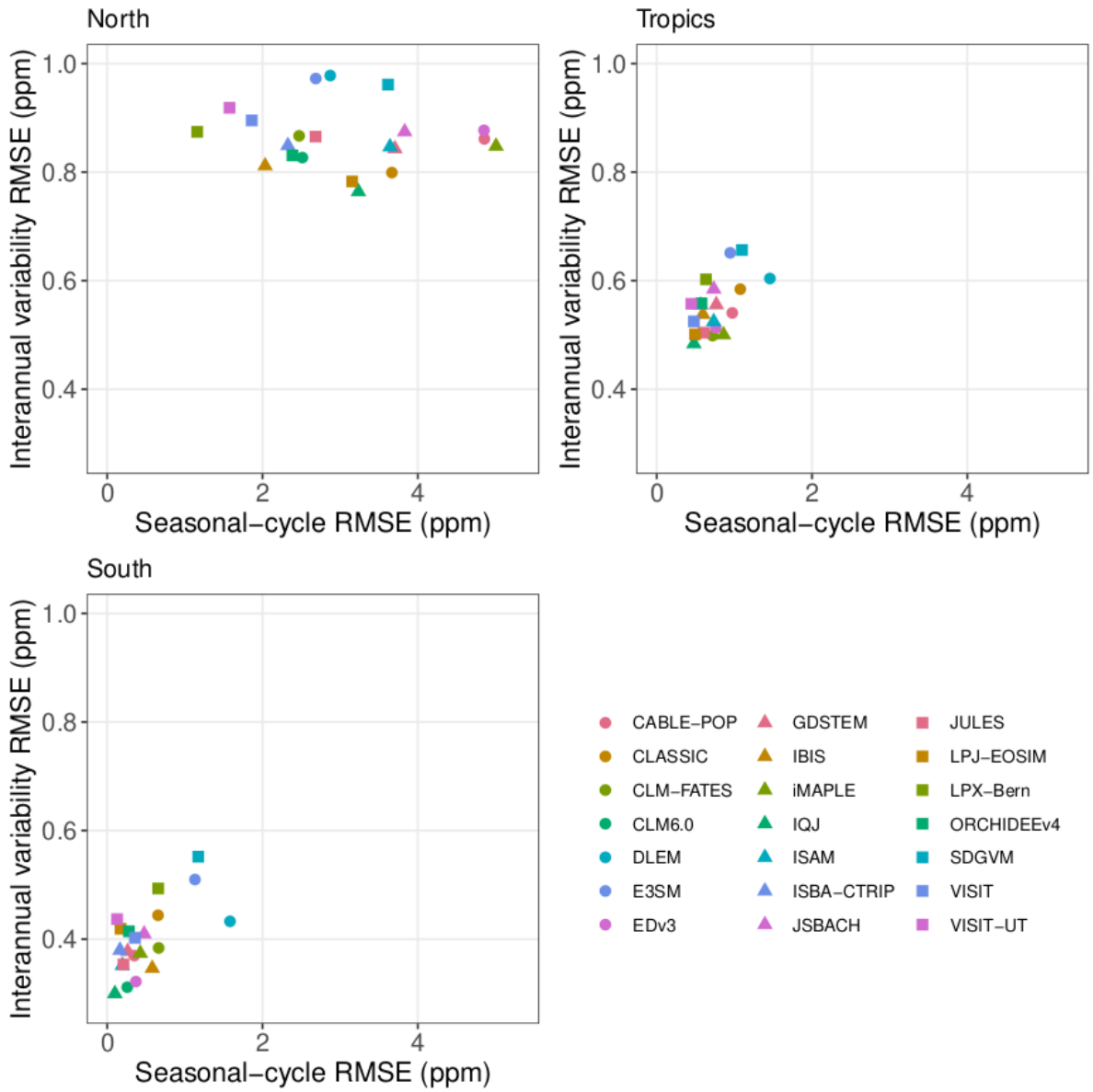


Figure S11 - Evaluation of the DGVM net land flux against atmospheric CO_2 at NOAA Global Monitoring Laboratory stations in three latitude bands: North (north of 30°N, 9 stations), Tropics (30°S-30°N, 20 stations) and South (south of 30°S, 9 stations). For each of the 21 DGVMs that provide monthly NBP, the x-axis shows the root-mean-square error (RMSE, ppm) of the simulated mean seasonal cycle and the y-axis the RMSE of the interannual variability, relative to the observations. Simulated CO2 is emulated in ILAMB from monthly NBP using atmospheric pulse-response functions, and fossil fuel and ocean contributions are removed from the observations. Lower values indicate better agreement. See Supplement S.4.2 for details.

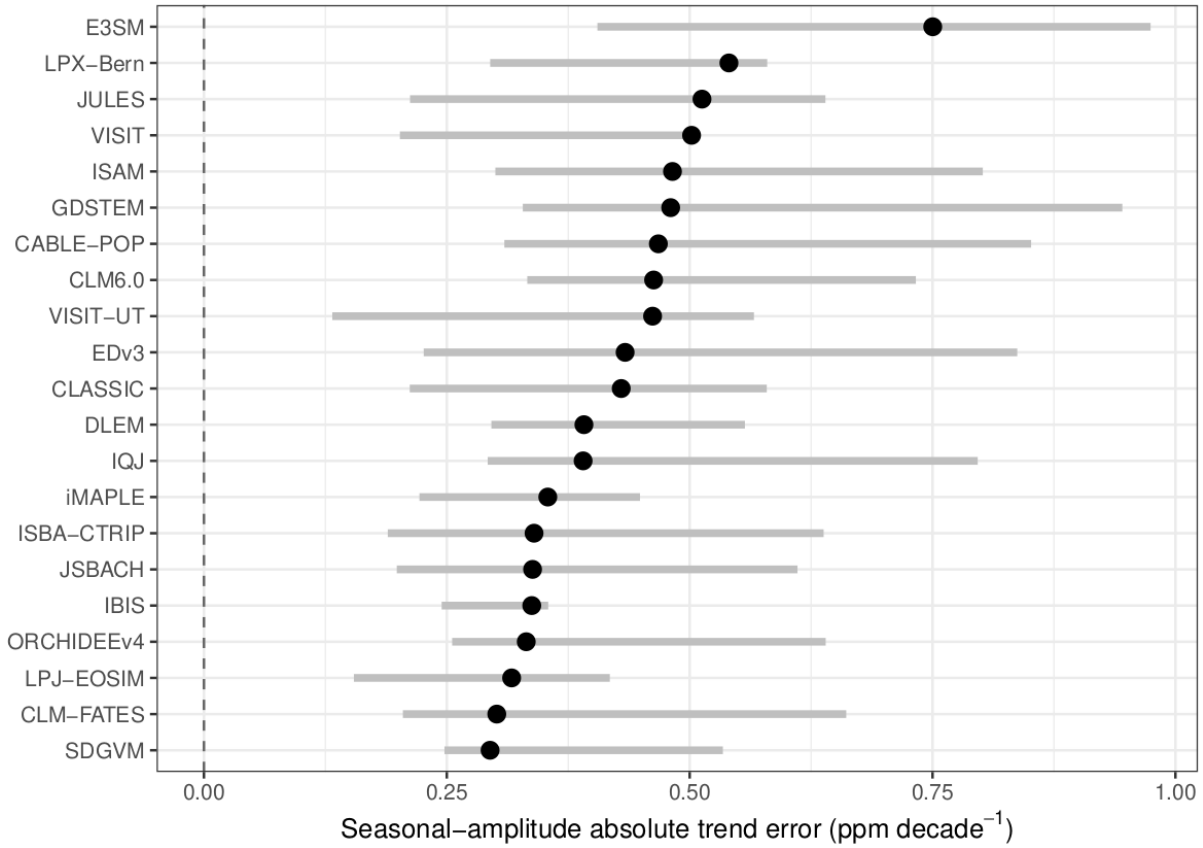


Figure S12 - Absolute error in the trend of the CO_2 seasonal amplitude (ppm decade^{-1}) for the 21 DGVMs that provide monthly NBP, evaluated at the 9 NOAA Global Monitoring Laboratory stations north of 30°N. The error is the absolute difference between the simulated and observed trends in seasonal amplitude. Dots show the median across stations and grey bars the interquartile range. Models are ordered by their median error, and the dashed line marks zero error. See Supplement S.4.2 for details.

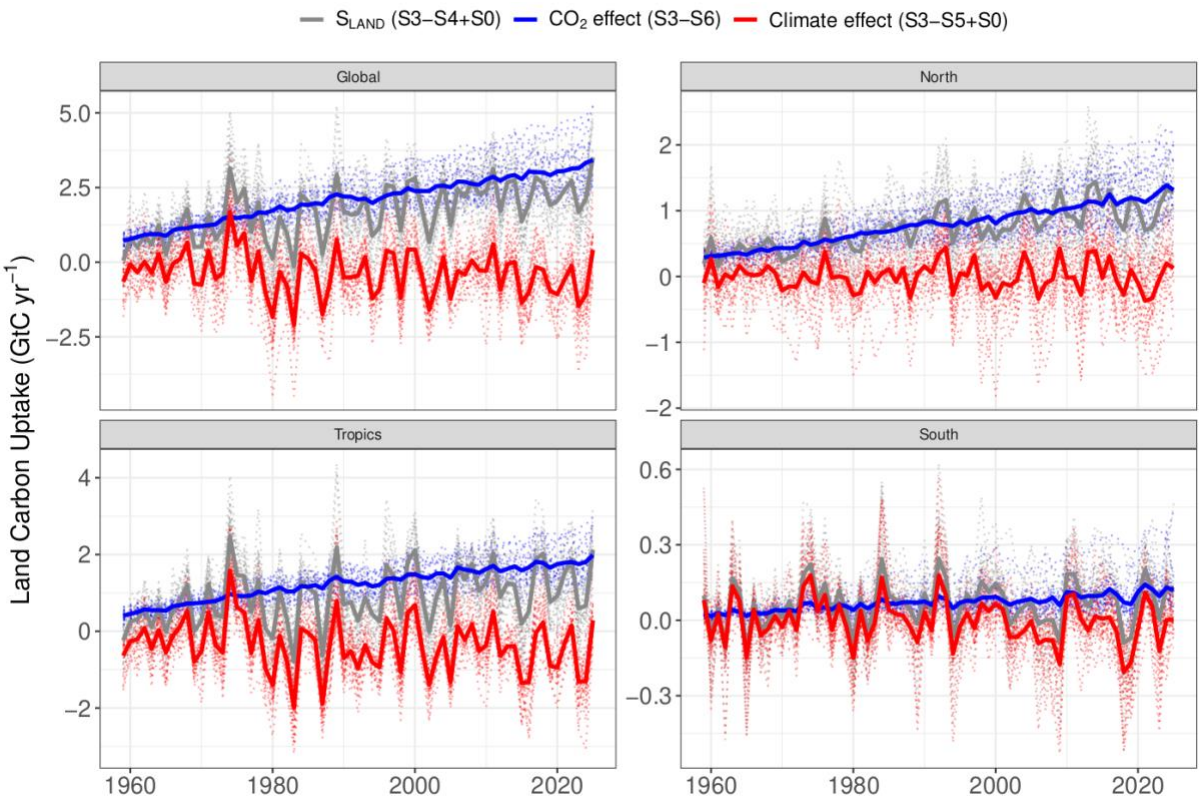


Figure S13. Time-series of CO_2 and climate effects on the land sink for global land, and three latitudinal bands (north, tropics, south) as indicated in the panels. Dotted lines show individual dynamic global vegetation models and solid lines indicate the ensemble mean. The grey line shows the S_{LAND} flux (simulation S3-S4=S0) without δL adjustment, which represents the sum of natural fluxes, CO_2 and climate effects. The CO_2 and climate effects are calculated from simulations S3 minus S6 and S3 minus S5 plus S0, respectively. See section S4.1 on DGVM simulations.

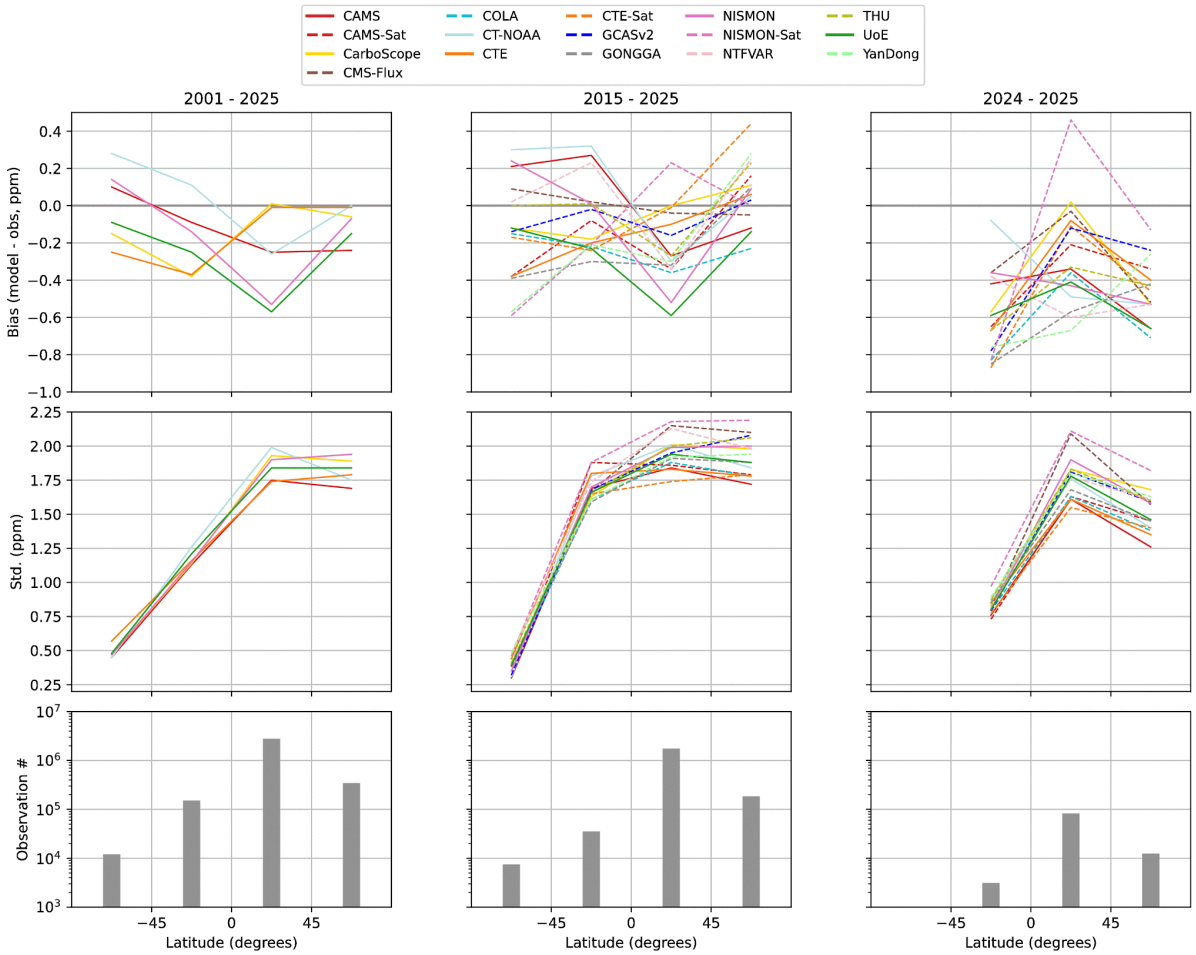


Figure S14. Evaluation of the atmospheric inversion products. The mean of the model minus observations is shown for four latitude bands in three periods: (first panel) 2001-2025, (second panel) 2015-2025, and for the latest year only (third panel). The 16 systems are compared to independent CO_2 observations from aircraft over many places of the world between 2 and 7 km above sea level. Aircraft measurements archived in the Cooperative Global Atmospheric Data Integration Project (Schuldt et al., 2025, Schuldt et al., 2026) from sites, campaigns or programs that have not been assimilated and cover at least 9 months (except for SH programs) between 2001 and 2025, have been used to compute the biases (top row) and their standard deviations (middle row) in four 45° latitude bins. Land and ocean data are used without distinction, and observation density varies strongly with latitude and time as seen on the lower panels.



Figure S15. Fire carbon emissions for the months January-September for each year 2003-2025 from two global fire emissions products. (Top row) Global emissions. (Middle row) Emissions for the northern hemisphere extratropics (>30° N), tropics (30°N-30°S) and southern extratropics (>30°S). (Bottom row) Emissions by RECCAP2 region. The Global Fire Assimilation System (GFAS; Di Giuseppe et al., 2018) (left column) and the Global Fire Emissions Database (GFED, version 4.1s; van der Werf et al., 2017) (right column) are among the most widely applied global fire emissions products based on satellite remote sensing of fire. GFED relies on the post-fire detection of burned areas combined with fuel consumption factors. GFAS relies on the detection of thermal energy release during active fires.

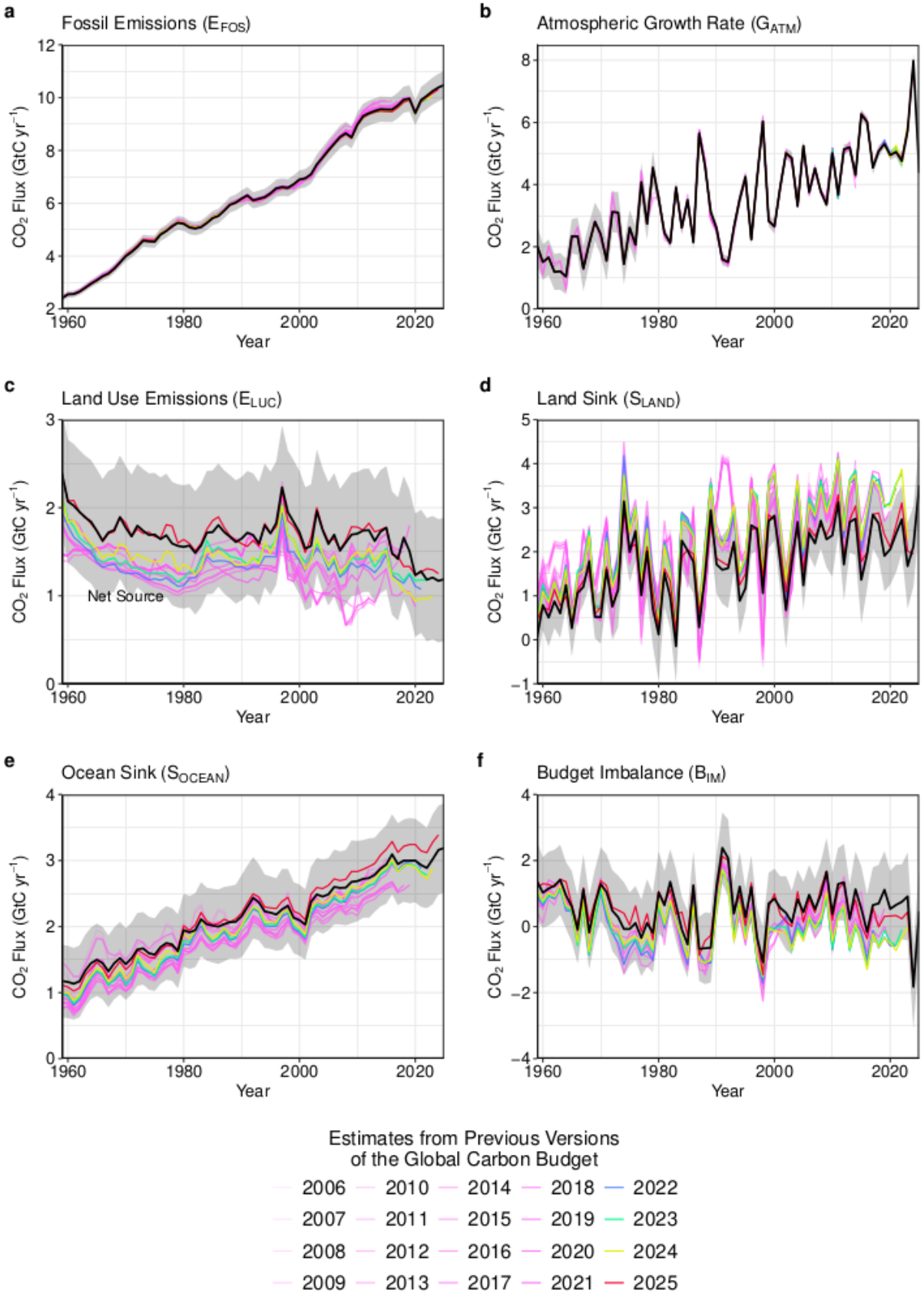
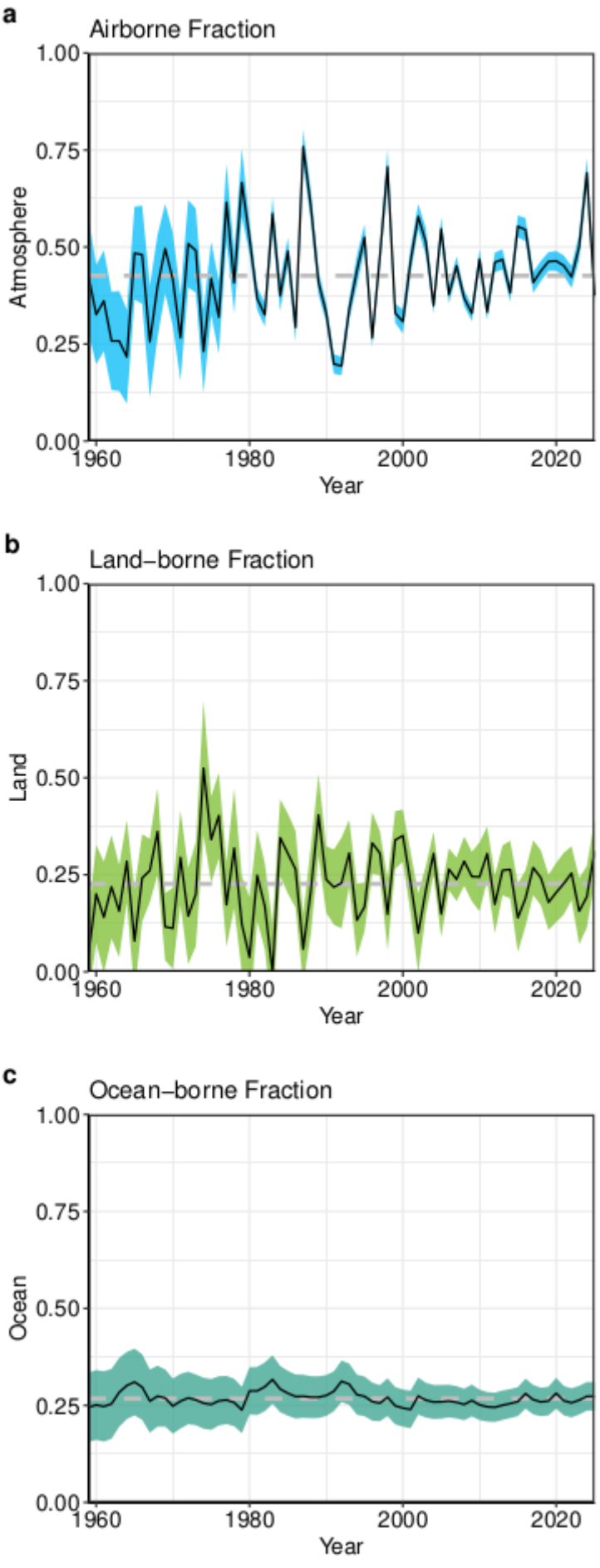


Figure S16. Comparison of the estimates of each component of the global carbon budget in this study (black line) with the estimates released annually by the GCP since 2006. Grey shading shows the uncertainty bounds of

1625 the current global carbon budget, based on the uncertainty assessments described in Supplement S1 to S4. CO_2
1626 emissions from (a) fossil CO_2 emissions excluding cement carbonation (E_{FOS}), and (b) land-use change (E_{LUC}),
1627 as well as their partitioning among (c) the atmosphere (G_{ATM}), (d) the land (S_{LAND}), and (e) the ocean (S_{OCEAN}).
1628 See legend for the corresponding years, and Tables 3 and S10 for description of changes in methodology. The
1629 budget year corresponds to the year when the budget was first released. All values are in GtC yr^{-1}.
1630


a
Airborne Fraction
1.00
0.75
0.50
0.25
0.00
Atmosphere
1960
1980
2000
2020
Year
b
Land–borne Fraction
1.00
0.75
0.50
0.25
0.00
Land
1960
1980
2000
2020
Year
c
Ocean–borne Fraction
1.00
0.75
0.50
0.25
0.00
Ocean
1960
1980
2000
2020
Year

1631

Figure S17. The partitioning of total anthropogenic CO_2 emissions (E_{FOS} + E_{LUC}) across (a) the atmosphere (airborne fraction), (b) land (land-borne fraction), and (c) ocean (ocean-borne fraction). Black lines represent the central estimate, and the coloured shading represents the uncertainty. The grey dashed lines represent the long-term average of the airborne (43%), land-borne (23%) and ocean-borne (27%) fractions during 1959-2025 (with a B_{IM} of 8%).



Figure S18. Kaya decomposition of the main drivers of fossil CO_2 emissions, considering population, GDP per person, Energy per GDP, and CO_2 emissions per energy, for China (top left), USA (top right), EU27 (middle left), India (middle right), Rest of the World (bottom left), and World (bottom right). Black dots are the annual fossil CO_2 emissions growth rate, coloured bars are the contributions from the different drivers to this growth rate. A general trend is that population and GDP growth put upward pressure on emissions (positive values), while energy per GDP and, more recently, CO_2 emissions per energy put downward pressure on emissions (negative values).

Additional references

Adler, R. F., Huffman, G. J., Chang, A., Ferraro, R., Xie, P.-P., Janowiak, J., Rudolf, B., Schneider, U., Curtis, S., Bolvin, D., Gruber, A., Susskind, J., Arkin, P., and Nelkin, E.: The Version-2 Global Precipitation Climatology Project (GPCP) Monthly Precipitation Analysis (1979–Present), J. Hydrometeor, 4, 1147–1167, https://doi.org/10.1175/1525-7541(2003)004<1147:TVGPCP>2.0.CO;2, 2003.

Alemohammad, S. H., Fang, B., Konings, A. G., Aires, F., Green, J. K., Kolassa, J., Miralles, D., Prigent, C., and Gentine, P.: Water, Energy, and Carbon with Artificial Neural Networks (WECANN): a statistically based estimate of global surface turbulent fluxes and gross primary productivity using solar-induced fluorescence, Biogeosciences, 14, 4101–4124, https://doi.org/10.5194/bg-14-4101-2017, 2017.

Alin, S. R., Curless, S., and Feely, R. A.: Fugacity of carbon dioxide (fCO2), temperature, salinity and other variables collected from surface underway observations during the NOAA Ship Bell M. Shimada cruises on the continental shelf of the US West Coast, North Pacific Ocean in 2025 (NCEI Accession 0315127), NOAA National Centers for Environmental Information [data set], https://doi.org/10.25921/ezn3-q004, 2026a.

Alin, S. R., Curless, S., and Feely, R. A.: Fugacity of carbon dioxide (fCO2), temperature, salinity and other variables collected from surface underway observations using shower head equilibrator, carbon dioxide gas detector and other instruments from R/V Thomas G. Thompson cruises in the North Pacific Ocean, Indian Ocean in 2025 (NCEI Accession 0315111), NOAA National Centers for Environmental Information [data set], https://doi.org/10.25921/texj-fc86, 2026b.

Alin, S. R., Curless, S., Feely, R. A., and Herndon, J.: Fugacity of carbon dioxide (fCO2), temperature, salinity, and other variables collected from surface underway observations using shower head equilibrator, carbon dioxide gas detector and other instruments from NOAA Ship Oscar Dyson cruises in the North Pacific Ocean, Gulf of Alaska, Bering Sea in 2025 (NCEI Accession 0315072), NOAA National Centers for Environmental Information [data set], https://doi.org/10.25921/k0fw-mv14, 2026c.

Alin, S. R., Curless, S., Herndon, J., and Feely, R. A.: Fugacity of carbon dioxide (fCO2), temperature, salinity and other variables collected from surface underway observations using shower head equilibrator, carbon dioxide gas detector and other instruments during the ship of opportunity vessel Tysla cruises in the Indian Ocean, Pacific Ocean, Atlantic Ocean, Caribbean Sea in 2025 (NCEI Accession 0315161), NOAA National Centers for Environmental Information [data set], https://doi.org/10.25921/hr6b-p951, 2026d.

Alin, S. R., Feely, R. A., and Curless, S.: Fugacity of carbon dioxide (fCO2), temperature, salinity and other variables collected from surface underway observations from the M/V BlueFin cruises in the Tropical and North Pacific Ocean from 2025-09-14 to 2025-11-01 (NCEI Accession 0315103), NOAA National Centers for Environmental Information [data set], https://doi.org/10.25921/1e16-4t24, 2026e.

Alkama, R.: Land Carbon Budget: Intact and Non-Intact Forest NBP from TRENDY-v11 S2 simulations [code], available at: https://github.com/RamAlkama/LandCarbonBudget_IntactAndNonIntactForest, last access: 21 January 2025, 2022.

Amador-Jiménez, M., Millner, N., Palmer, C., Pennington, R. T., and Sileci, L.: The Unintended Impact of Colombia's Covid-19 Lockdown on Forest Fires, Environ Resource Econ, 76, 1081–1105, https://doi.org/10.1007/s10640-020-00501-5, 2020.

Amante, C. and Eakins, B. W.: ETOPO1 Global Relief Model converted to PanMap layer format, PANGAEA [dataset], https://doi.org/10.1594/PANGAEA.769615, 2009.

Andres, R. J., Boden, T. A., Bréon, F.-M., Ciais, P., Davis, S., Erickson, D., Gregg, J. S., Jacobson, A., Marland, G., Miller, J., Oda, T., Olivier, J. G. J., Raupach, M. R., Rayner, P., and Treanton, K.: A synthesis of carbon dioxide emissions from fossil-fuel combustion, Biogeosciences, 9, 1845–1871, https://doi.org/10.5194/bg-9-1845-2012, 2012.

Andres, R. J., Boden, T. A., and Higdon, D.: A new evaluation of the uncertainty associated with CDIAC estimates of fossil fuel carbon dioxide emission, Tellus B: Chemical and Physical Meteorology, 66, 23616, https://doi.org/10.3402/tellusb.v66.23616, 2014.

Andrew, R. M.: Towards near real-time, monthly fossil CO2 emissions estimates for the European Union with current-year projections, Atmos. Pollut. Res., 12, 12, 101229, https://doi.org/10.1016/j.apr.2021.101229, 2021.

Andrew, R. M. and Peters, G. P.: A multi-region input–output table based on the global trade analysis project database (GTAP-MRIO), Economic Systems Research, 25, 99–121, https://doi.org/10.1080/09535314.2012.761953, 2013.

Aramaki, T., Nakaoka, S.-I., and Wada, C.: Partial pressure of carbon dioxide, water temperature, salinity and other variables collected from surface underway observations during the R/V Oshoro Maru V cruises in the North Pacific Ocean, Japan Sea in 2025 (NCEI Accession 0315076), NOAA National Centers for Environmental Information [data set], https://doi.org/10.25921/qtna-bn06, 2026.

Arora, V. K., Boer, G. J., Christian, J. R., Curry, C. L., Denman, K. L., Zahariev, K., Flato, G. M., Scinocca, J. F., Merryfield, W. J., and Lee, W. G.: The Effect of Terrestrial Photosynthesis Down Regulation on the Twentieth-Century Carbon Budget Simulated with the CCCma Earth System Model, 22, 6066–6088, https://doi.org/10.1175/2009JCLI3037.1, 2009.

Arora, V. K. and Scinocca, J. F.: Constraining the strength of the terrestrial CO2 fertilization effect in the Canadian Earth system model version 4.2 (CanESM4.2), Geosci. Model Dev., 9, 2357–2376, https://doi.org/10.5194/gmd-9-2357-2016, 2016.

Bakker, D. C. E., Pfeil, B., Landa, C. S., Metzl, N., O'Brien, K. M., Olsen, A., Smith, K., Cosca, C., Harasawa, S., Jones, S. D., Nakaoka, S., Nojiri, Y., Schuster, U., Steinhoff, T., Sweeney, C., Takahashi, T., Tilbrook, B., Wada, C., Wanninkhof, R., Alin, S. R., Balestrini, C. F., Barbero, L., Bates, N. R., Bianchi, A. A., Bonou, F., Boutin, J., Bozec, Y., Burger, E. F., Cai, W.-J., Castle, R. D., Chen, L., Chierici, M., Currie, K., Evans, W., Featherstone, C., Feely, R. A., Fransson, A., Goyet, C., Greenwood, N., Gregor, L., Hankin, S., Hardman-Mountford, N. J., Harlay, J., Hauck, J., Hoppema, M., Humphreys, M. P., Hunt, C. W., Huss, B., Ibánhez, J. S. P., Johannessen, T., Keeling, R., Kitidis, V., Körtzinger, A., Kozyr, A., Krasakopoulou, E., Kuwata, A., Landschützer, P., Lauvset, S. K., Lefèvre, N., Lo Monaco, C., Manke, A., Mathis, J. T., Merlivat, L., Millero, F. J., Monteiro, P. M. S., Munro, D. R., Murata, A., Newberger, T., Omar, A. M., Ono, T., Paterson, K., Pearce, D., Pierrot, D., Robbins, L. L., Saito, S., Salisbury, J., Schlitzer, R., Schneider, B., Schweitzer, R., Sieger, R., Skjelvan, I., Sullivan, K. F., Sutherland, S. C., Sutton, A. J., Tadokoro, K., Telszewski, M., Tuma, M., van Heuven, S. M. A. C., Vandemark, D., Ward, B., Watson, A. J., and Xu, S.: A multi-decade record of high-quality CO2 data in version 3 of the Surface Ocean CO2 Atlas (SOCAT), Earth Syst. Sci. Data, 8, 383–413, https://doi.org/10.5194/essd-8-383-2016, 2016.

Bakker, D. C. E., Alin, S. R., Bates, N. R., Ehmen, T., Gkritzalis, T., Jones, S. D., Kamb, L., Kozyr, A., Lauvset, S. K., Macovei, V. A., Metzl, N., Nakaoka, S.-i., O'Brien, K. M., Olsen, A., Pierrot, D., Poelmans, S., Steinhoff, T., Sutton, A. J., Sweeney, C., Takao, S., Telszewski, M., Theetaert, H., Tilbrook, B., Wada, C., Wanninkhof, R., Akl, J., Aramaki, T., Arbilla, L. A., Àvila, R. A., Baier, B. C., Barbero, L., Battisti, R., Beatty, C. M., Becker, H., Benoit-Cattin, A., Berghoff, C. F., Bittig, H. C., Bonin, J. A., Bozzano, R., Burger, E. F., Cai, W.-J., Cantoni, C., Castelli, G., Castro, A., Chambers, D. P., Chierici, M., Cronin, M., Cubiella, Á. H., Curbelo, D., Curless, S. E., Czyz, C., Diverrès, D., Dougherty, S., Enochs, I., Enright, M. P., Enyo, K., Evans, W., Feely, R. A., Flohr, A., Fragiacomo, E., Frangoulis, C., Fransson, A., Gehrung, M., Glockzin, M., González, A. G., González-Dávila, M., González-Santana, D., Hales, B., Hamnca, S., Hartman, S. E., Hermes, R., Herndon, J., Hoppema, M., Howard, E., Huertas, E., Kerr, R., Kristensen, T. O., Landschützer, P., Lee, C. M., Lee, H., Lefèvre, N., Leseurre, C., Lo Monaco, C., Luchetta, A., Maenner Jones, S. M., Manalang, D., McAuliffe, A. M., Mdokwana, B. W., Monacci, N. M., Monteiro, P. M. S., Morell, J. M., Munro, D. R., Neill, C., Newberger, T., Nickford, S., Nillson, E., Noakes, S., Noh, J.-H., Noisel, C., O'Brien, C., Olivier, L., Omar, A., Orselli, I., Padin, A., Pena, L. D., Pensieri, S., Pryterch, J., Rehder, G., Rutgersson, A., Sabine, C. L., Sallée, J.-B., Sanders, R., Santana-Casiano, J. M., Sarpe, D., Schirnik, C., Schlitzer, R., Shadwick, E., Skjelvan, I., T'Jampens, M., Tamsitt, V., Toledo Aboy, A. E., Tovar-Sanchez, A., Tsanwani, M., Van de Velde, S., Van Ooijen, E., Vandemark, D., Veccia, M. H., Voynova, Y. G., Williams, N. L., and Xu, Y.: Surface Ocean CO2 Atlas Database Version 2026 (SOCATv2026) (NCEI Accession 0315110), NOAA National Centers for Environmental Information [data set], https://doi.org/10.25921/8dba-fr90, 2026.

Barbero, L., Pierrot, D., and Wanninkhof, R.: Partial pressure of carbon dioxide, salinity, temperature and other variables collected from surface underway observations from R/V F.G. Walton Smith coastal cruises in the North Atlantic Ocean and Gulf of America in 2025 (NCEI Accession 0312676), NOAA National Centers for Environmental Information [data set], https://doi.org/10.25921/qzwf-se04, 2026.

Bates, N. R. and Enright, M.: Partial pressure of carbon dioxide (pCO_2), water temperature, salinity and barometric pressure collected from surface underway coastal observations during R/V Atlantic Explorer cruises in the North Atlantic Ocean in 2025, NOAA National Centers for Environmental Information [data set], https://doi.org/10.25921/jzzh-vg02, 2026a.

Bates, N. R. and Enright, M.: Partial pressure of carbon dioxide (pCO_2), water temperature, salinity and barometric pressure collected from surface underway observations during the M/V Oleander SOOP Lines in the North Atlantic Ocean in 2025, NOAA National Centers for Environmental Information [data set], https://doi.org/10.25921/jsff-wk47, 2026b.

Bauer, J. E., Cai, W.-J., Raymond, P. A., Bianchi, T. S., Hopkinson, C. S., and Regnier, P. A. G.: The changing carbon cycle of the coastal ocean, Nature, 504, 61–70, https://doi.org/10.1038/nature12857, 2013.

Beckman, J. and Countryman, A. M.: The Importance of Agriculture in the Economy: Impacts from COVID-19, Am. J. Agr. Econ., 103, 1595–1611, https://doi.org/10.1111/ajae.12212, 2021.

Bellouin, N., Rae, J., Jones, A., Johnson, C., Haywood, J., and Boucher, O.: Aerosol forcing in the Climate Model Intercomparison Project (CMIP5) simulations by HadGEM2-ES and the role of ammonium nitrate, J. Geophys. Res.-Atmos., 116, D20206, https://doi.org/10.1029/2011JD016074, 2011.

Benoit-Cattin, A.: Partial pressure of carbon dioxide, water temperature, salinity and other variables collected from surface underway observations during R/V Arni Fridriksson cruises in the Irminger Sea, North Atlantic Ocean in 2025 (NCEI Accession 0315075), NOAA National Centers for Environmental Information [data set], https://doi.org/10.25921/3s7j-5w56, 2026.

Berghoff, C. F., Arbilla, L. A., and Veccia, M. H.: Partial pressure of carbon dioxide, water temperature, salinity and other variables collected from surface underway observations during the R/V Víctor Angelescu cruises in the South Atlantic Ocean in 2025, NOAA National Centers for Environmental Information [data set] (NCEI Accession 0314985), https://doi.org/10.25921/fr55-fp38, 2026

Bernardello, R., Sicardi, V., Lapin, V., Ortega, P., Ruprich-Robert, Y., Tourigny, E., and Ferrer, E.: Ocean biogeochemical reconstructions to estimate historical ocean CO2 uptake, Earth Syst. Dynam.,15, 1255–1275, https://doi.org/10.5194/esd-15-1255-2024, 2024.

Bethke, I., Wang, Y., Counillon, F., Keenlyside, N., Kimmritz, M., Fransner, F., ... & Eldevik, T.: NorCPM1 and its contribution to CMIP6 DCPP. Geoscientific Model Development, 14(11), 7073-7116, 2021.

Bilbao, R., S. Wild, P. Ortega et al. (2021). Assessment of a full-field initialised decadal climate prediction system with the CMIP6 version of EC-Earth. Earth Systems Dynamics, doi:10.5194/esd-2020-66. Broecker, W. S.: Ocean chemistry during glacial time, Geochimica et Cosmochimica Acta, 46, 1689–1705, https://doi.org/10.1016/0016-7037(82)90110-7, 1982.

Boucher O., Servonnat, J., Albright,A. L., Aumont, O., Balkanski, Y.,Bastrikov, V., et al.: Presentation and evaluation of the IPSL-CM6A-LRclimate model.Journal of Advances inModeling Earth Systems,12,e2019MS002010, 2020.

Brune, S., A. Düsterhus, H. Pohlmann, W. A. Müller, and J. Baehr: Time dependency of the prediction skill for the north atlantic subpolar gyre in initialized decadal hindcasts. Climate dynamics, 51 (5), 1947–1970, 2018.

Brunner, L., Pendergrass, A. G., Lehner, F., Merrifield, A. L., Lorenz, R., and Knutti, R.: Reduced global warming from CMIP6 projections when weighting models by performance and independence, Earth Syst. Dynam., 11, 995–1012, https://doi.org/10.5194/esd-11-995-2020, 2020.

Bullister, J. L., and Warner, M. J.: Atmospheric Histories (1765–2022) for CFC-11, CFC-12, CFC-113, CCl4, SF6 and N2O (NCEI Accession 0164584), NOAA National Centers for Environmental Information [data set], https://doi.org/10.3334/cdiac/otg.cfc_atm_hist_2015, 2017.

Cerdeiro, D.A., Komaromi, A., Liu, Y., Saeed, M.: World Seaborne Trade in Real Time: A Proof of Concept for Building AIS-based Nowcasts from Scratch. International Monetary Fund (IMF) WP/20/57, available at: https://www.imf.org/en/Publications/WP/Issues/2020/05/14/World-Seaborne-Trade-in-Real-Time-A-Proof-of-Concept-for-Building-AIS-based-Nowcasts-from-49393, last access: 21 January 2025, 2020.

Chatfield, C.: The Holt-Winters Forecasting Procedure, J. Roy. Stat. Soc. C., 27, 264–279, https://doi.org/10.2307/2347162, 1978.

Chau, T.-T.-T., Gehlen, M., Metzl, N., and Chevallier, F.: CMEMS-LSCE: a global, 0.25°, monthly reconstruction of the surface ocean carbonate system, Earth Syst. Sci. Data, 16, 121–160, https://doi.org/10.5194/essd-16-121-2024, 2024.

Chen, Y., Hall, J., van Wees, D., Andela, N., Hantson, S., Giglio, L., van der Werf, G.R., Morton, D.C., and Randerson, J.T. (2023) Multi-decadal trends and variability in burned area from the fifth version of the Global Fire Emissions Database (GFED5). ESSD 15(11), 5227–5259 https://doi.org/10.5194/essd-15-5227-2023

Cheng, L., Pan, Y., Tan, Z., Zheng, H., Zhu, Y., Wei, W., Du, J., Yuan, H., Li, G., Ye, H., Gouretski, V., Li, Y., Trenberth, K. E., Abraham, J., Jin, Y., Reseghetti, F., Lin, X., Zhang, B., Chen, G., Mann, M. E., and Zhu, J.: IAPv4 ocean temperature and ocean heat content gridded dataset, Earth Syst. Sci. Data, 16, 3517–3546, https://doi.org/10.5194/essd-16-3517-2024, 2024.

Cheng, L., Trenberth, K. E., Gruber, N., Abraham, J. P., Fasullo, J. T., Li, G., Mann, M. E., Zhao, X., and Zhu, J.: Improved Estimates of Changes in Upper Ocean Salinity and the Hydrological Cycle, J. Climate, 33, 10357–10381, https://doi.org/10.1175/JCLI-D-20-0366.1, 2020.

Chini, L., Hurtt, G., Sahajpal, R., Frolking, S., Klein Goldewijk, K., Sitch, S., Ganzenmüller, R., Ma, L., Ott, L., Pongratz, J., and Poulter, B.: Land-use harmonization datasets for annual global carbon budgets, 13, 4175–4189, https://doi.org/10.5194/essd-13-4175-2021, 2021.

Ciais, P., Chevallier, F., Wang, Y., and Lauerwald, R.: Lateral Accounting of Transport in Terrestrial Ecosystems (LATTE): A High-Resolution Global Land-Atmosphere CO2 Flux Data Set From 1961 to 2022 for Atmospheric Inversions and Carbon Budgeting Studies, Global Biogeochemical Cycles, 40, e2026GB009142, https://doi.org/10.1029/2026GB009142, 2026.

Clarke, D., Flachenecker, F., Guidetti, E., and Pionnier, P.-A.: CO2 Emissions from air transport: A near-real-time global database for policy analysis, Organization for Economic Co-operation and Development, Paris OECD Statistics Working Papers 2022/04, available at: https://doi.org/10.1787/ecc9f16b-en, last access: 21 January 2025, 2022.

1817 Clarke, D., Chan P., Dequeljoe, M., Kim, Y., and Barahona, S.: CO2 emissions from global shipping: A new experimental
1818 database", OECD Statistics Working Papers, No. 2023/04, OECD Publishing, Paris, https://doi.org/10.1787/bc2f7599-en,
1819 2023

1820 Claverie, M., Matthews, J., Vermote, E., and Justice, C.: A 30+ Year AVHRR LAI and FAPAR Climate Data Record:
1821 Algorithm Description and Validation, Remote Sensing, 8, 263, https://doi.org/10.3390/rs8030263, 2016.

1822 Clement, D. and Gruber, N.: The eMLR(C*) Method to Determine Decadal Changes in the Global Ocean Storage of
1823 Anthropogenic CO2, Global Biogeochem. Cycles, 32, 654–679, https://doi.org/10.1002/2017GB005819, 2018.

1824 Collier, N., Hoffman, F. M., Lawrence, D. M., Keppel-Aleks, G., Koven, C. D., Riley, W. J., et al. (2018). The International
1825 Land Model Benchmarking (ILAMB) system: Design, theory, and implementation. Journal of Advances in Modeling Earth
1826 Systems, 10, 2731–2754. https://doi.org/10.1029/2018MS001354

1827 Conchedda, G. and Tubiello, F. N.: Drainage of organic soils and GHG emissions: validation with country data, Earth Syst.
1828 Sci. Data, 12, 3113–3137, https://doi.org/10.5194/essd-12-3113-2020, 2020.

1829 Cooper, D. J., Watson, A. J., and Ling, R. D.: Variation of pCO2 along a North Atlantic shipping route (U.K. to the
1830 Caribbean): A year of automated observations, Marine Chemistry, 60, 147-164, 1998.

1831 Crippa, M., Janssens-Maenhout, G., Guizzardi, D., Van Dingenen, R., and Dentener, F.: Contribution and uncertainty of
1832 sectorial and regional emissions to regional and global PM2.5 health impacts, 19, 5165–5186, https://doi.org/10.5194/acp-
1833 19-5165-2019, 2019.

1834 Cunningham, S. A., Kanzow, T., Rayner, D., Baringer, M. O., Johns, W. E., Marotzke, J., Longworth, H. R., Grant, E. M.,
1835 Hirschi, J. J.-M., Beal, L. M., Meinen, C. S., and Bryden, H. L.: Temporal variability of the Atlantic meridional overturning
1836 circulation at 26.5°N, Science, 317, 935–938, https://doi.org/10.1126/science.1141304, 2007.

1837 Dai, A. and Trenberth, K. E.: Estimates of Freshwater Discharge from Continents: Latitudinal and Seasonal Variations, J.
1838 Hydrometeorol., 3, 660–687, https://doi.org/10.1175/1525-7541(2002)003<0660:EOFDFC>2.0.CO;2, 2002.

1839 Davis, S. J. and Caldeira, K.: Consumption-based accounting of CO2 emissions, Proceedings of the National Academy of
1840 Sciences, 107, 5687–5692, https://doi.org/10.1073/pnas.0906974107, 2010.

1841 de Boyer Montégut, C., G. Madec, A. S. Fischer, A. Lazar, and D. Iudicone (2004), Mixed layer depth over the global ocean:
1842 An examination of profile data and a profile-based climatology, J. Geophys. Res., 109, C12003, doi:10.1029/2004JC002378.

1843 de Boyer Montégut Clément (2023). Mixed layer depth climatology computed with a density threshold criterion of
1844 0.03kg/m3 from 10 m depth value. SEANOE. https://doi.org/10.17882/91774

1845 De Kauwe, M. G., Disney, M. I., Quaife, T., Lewis, P., and Williams, M.: An assessment of the MODIS collection 5 leaf
1846 area index product for a region of mixed coniferous forest, Remote Sensing of Environment, 115, 767–780,
1847 https://doi.org/10.1016/j.rse.2010.11.004, 2011.

1848 Dee, D. P., Uppala, S. M., Simmons, A. J., Berrisford, P., Poli, P., Kobayashi, S., ... & Vitart, F.. The ERA-Interim
1849 reanalysis: Configuration and performance of the data assimilation system. Quarterly Journal of the royal meteorological
1850 society, 137(656), 553-597, 2011.

1851 DeVries, T. (2014), The oceanic anthropogenic CO2 sink: Storage, air-sea fluxes, and transports over the industrial era,
1852 Global Biogeochem. Cycles, 28, 631–647, doi:10.1002/2013GB004739.

1853 DeVries, T.: Atmospheric CO2 and Sea Surface Temperature Variability Cannot Explain Recent Decadal Variability of the
1854 Ocean CO2 Sink, Geophysical Research Letters, 49, e2021GL096018, https://doi.org/10.1029/2021GL096018, 2022.

1855 Dickson, A. G., Sabine, C. L., and Christian, J. R.: Guide to best practices for ocean CO2 measurement. Sidney, British
1856 Columbia, North Pacific Marine Science Organization, 191pp. (PICES Special Publication 3; IOCCP Report 8). DOI:
1857 https://doi.org/10.25607/OBP-1342, 2007.

1858 Dorgeist, L., Schwingshackl, C., Bultan, S., and Pongratz, J.: A consistent budgeting of terrestrial carbon fluxes, Nat
1859 Commun, 15, 7426, https://doi.org/10.1038/s41467-024-51126-x, 2024.

1860 Dlugokencky, E. J., Lang, P. M., Masarie, K., Crotwell, A. M., and Crotwell, M. J.: Atmospheric carbon dioxide dry air
1861 mole fractions from the NOAA ESRL carbon cycle cooperative global air sampling network, 1968–2012, Version: 2013-08-
1862 27, available at: ftp://aftp.cmdl.noaa.gov/data/trace_gases/co2/flask/surface/, 2013.

1863 Dou, X., Wang, Y., Ciais, P., Chevallier, F., Davis, S. J., Crippa, M., Janssens-Maenhout, G., Guizzardi, D., Solazzo, E.,
1864 Yan, F., Huo, D., Zheng, B., Zhu, B., Cui, D., Ke, P., Sun, T., Wang, H., Zhang, Q., Gentine, P., Deng, Z., and Liu, Z.: Near-
1865 real-time global gridded daily CO2 emissions, The Innovation, 3, 100182, https://doi.org/10.1016/j.xinn.2021.100182, 2022.

Döscher, R., Acosta, M., Alessandri, A., Anthoni, P., Arneth, A., Arsouze, T., ... & Zhang, Q.: The EC-earth3 Earth system model for the climate model intercomparison project 6. Geoscientific Model Development Discussions, 2021, 1-90. 2021.

Dubayah, R.O., J. Armston, S.P. Healey, Z. Yang, P.L. Patterson, S. Saarela, G. Stahl, L. Duncanson, and J.R. Kellner. 2022. GEDI L4B Gridded Aboveground Biomass Density, Version 2.1. ORNL DAAC, Oak Ridge, Tennessee, USA. https://doi.org/10.3334/ORNLDAAC/2299

Duce, R. A., LaRoche, J., Altieri, K., Arrigo, K. R., Baker, A. R., Capone, D. G., Cornell, S., Dentener, F., Galloway, J., Ganeshram, R. S., Geider, R. J., Jickells, T., Kuypers, M. M., Langlois, R., Liss, P. S., Liu, S. M., Middelburg, J. J., Moore, C. M., Nickovic, S., Oschlies, A., Pedersen, T., Prospero, J., Schlitzer, R., Seitzinger, S., Sorensen, L. L., Uematsu, M., Ulloa, O., Voss, M., Ward, B., and Zamora, L.: Impacts of Atmospheric Anthropogenic Nitrogen on the Open Ocean, Science, 320, 893–897, https://doi.org/10.1126/science.1150369, 2008.

Eakins, B. W. and Sharman, G. F.: National Geophysical Data Center: Volumes of the World's Oceans from ETOPO1, available at: https://www.ngdc.noaa.gov/mgg/global/etopo1_ocean_volumes.html, last access: 21 January 2025, U.S. Department of Commerce, 2010.

Enyo, K. and Kadono, K.: Partial pressure of carbon dioxide, temperature, salinity and other variables collected from surface underway observations using carbon dioxide (CO2) gas analyzer, shower head chamber equilibrator for autonomous CO2 measurement and other instruments during R/V Ryofu Maru III cruises in the Pacific Ocean, East China Sea, Japan Sea in 2025 (NCEI Accession 0311810), NOAA National Centers for Environmental Information [data set], https://doi.org/10.25921/hfs8-k876, 2026.

Eurostat: Countries 2020, 1:1 million, available at: https://ec.europa.eu/eurostat/web/gisco/geodata/reference-data/administrative-units-statistical-units/countries, last access: 21 January 2025, 2024.

Evans, W., Bedard, K., and Campbell, K.: Surface Seawater and Marine Boundary Layer CO2 Time Series from the Bute Inlet Ocean Observing Station (BIOOS) Buoy, Bute Inlet, BC, Canada (Research) (v1.0), Hakai Institute [data set], https://doi.org/10.21966/4jvz-bv44, 2026.

Evans, W., Campbell, K., Hateley, S., and Barrette, J.: Surface Seawater and Marine Boundary Layer CO2 Observations from the Kwakshua Channel (KC) Buoy on the Central Coast of British Columbia (Research) (v1.0), Hakai Institute [data set], https://doi.org/10.21966/hz11-3m59, 2025a.

Evans, W., Campbell, K., Weekes, C., and Hare, A.: Seawater Carbon Dioxide (CO2) Content from the Burke-o-Lator pCO2/TCO2 analyzer located at the Hakai Institute's Quadra Island Field Station, Hyacinthe Bay, BC, Canada (Research) (v1.0), Hakai Institute [data set], https://doi.org/10.21966/ea8w-bf35, 2025b.

Eyring, V., Bony, S., Meehl, G. A., Senior, C. A., Stevens, B., Stouffer, R. J., and Taylor, K. E.: Overview of the Coupled Model Intercomparison Project Phase 6 (CMIP6) experimental design and organization, Geosci. Model Dev., 9, 1937–1958, https://doi.org/10.5194/gmd-9-1937-2016, 2016.

EIA: U.S. Energy Information Administration: Short-Term Energy Outlook, available at: http://www.eia.gov/forecasts/steo/outlook, last access: 21 January 2025, 2023.

FAO: Global Forest Resources Assessment 2020: Main report, FAO, Rome, Italy, 184 pp., https://doi.org/10.4060/ca9825en, 2020.

FAO: FAO Statistical Database (FAOSTAT), domains Climate Change, available at: http://www.fao.org/faostat/en/#data/GT, last access: 21 January 2025, 2021.

FAO: Land statistics 2001–2023 – Global, regional and country trends. FAOSTAT Analytical Briefs, No.107. Rome. https://doi.org/10.4060/cd5765en, 2025.

FAO: FAOSTAT Emissions from Drained organic soils, available at http://www.fao.org/faostat/en/#data/GV, last access: 14 October 2026, 2026a.

FAO: FAOSTAT Emissions totals database, available at https://faostat.fao.org/internal/en/#data/GT, last access: 14 October 2026, FAO2026b.

FAO/UNEP: Food and Agriculture Organisation / United Nations Environment Programme: The state of food and agriculture 1981, available at: https://www.fao.org/3/ap661e/ap661e.pdf, last access: 21 January 2025, 1981.

Fay, A. R., Heimdal, T. H., Acquaviva, V., Shaum, A. P., McKinley, G. A. (2025) Sensitivity of ocean carbon sink estimates to rare observations. Geophysical Research Letters 52, e2025GL117961. doi:10.1029/2025GL117961.

Fay, A. R. and McKinley, G. A.: Global open-ocean biomes: mean and temporal variability, ESSD 6, 273–284, https://doi.org/10.5194/essd-6-273-2014, 2014.

Fernández-Blanco, R., Rodríguez-Gómez, N., Pozo, D., Costescu, A., and Bolado-Lavín, R.: Natural gas consumption estimation in the European Union, Energy Reports, 11, 558–566, https://doi.org/10.1016/j.egyr.2023.12.011, 2024.

Fischer, G., Nachtergaele, F., Prieler, S., van Velthuizen, H. T., Verelst, L., and Wiberg, D.: Global Agro-ecological Zones Assessment for Agriculture (GAEZ 2008). IIASA, Laxenburg, Austria and FAO, Rome, Italy, available at: https://www.fao.org/soils-portal/data-hub/soil-maps-and-databases/harmonized-world-soil-database-v12/land-cover-data/ar/, last access: 21 January 2025, 2008.

Ford, D. J., Blannin, J., Watts, J., Watson, A. J., Landschützer, P., Jersild, A. and Shutler, J. D.: A comprehensive analysis of air-sea CO2 flux uncertainties constructed from surface ocean data products, Global Biogeochemical Cycles, 38, e2024GB008188, doi: 10.1029/2024GB008188., 2024

Ford, D. J., Shutler, J. D., Ashton, I., Sims, R. P., and Holding, T.: Recalculated (depth and temperature consistent) surface ocean CO_2 atlas (SOCAT) version 2026 (v0-1), https://doi.org/10.5281/ZENODO.20757579, 2026a.

Ford, D. J., Shutler, J. D., Holding, T., Sims, R. P., Ashton, I., Woolf, D. K., Goddijn-Murphy, L., Bakker, D. C. E., Sabine, C., Merchant, C. J., Embury, O., Dong, Y., and Wanninkhof, R.: Recalculating the Surface Ocean CO2 Atlas (SOCAT) to a sea surface temperature climate data record, Sci. Data, 13, 1329, https://doi.org/10.1038/s41597-026-07532-5, 2026b.

Ford, D. J., Kulk, G., Watson, A. J., Sathyendranath, S., and Shutler, J. D.: UExP-FNN-U full surface ocean carbonate system (v2026-pre1), https://doi.org/10.5281/ZENODO.19605928, 2026c.

Fransson, A., Czyz, C., and Chierici, M.: Kronprins Haakon surface ocean fCO2 observations taken by a General Oceanics system with a Li-7000 in 2025, ICOS ERIC -- Carbon Portal [data set], https://doi.org/10.18160/Y51V-HFE5, 2026.

Fu, W., Moore, J. K., Primeau, F., Collier, N., Ogunro, O. O., Hoffman, F. M., & Randerson, J. T. (2022). Evaluation of ocean biogeochemistry and carbon cycling in CMIP earth system models with the International Ocean Model Benchmarking (IOMB) software system. Journal of Geophysical Research: Oceans, 127, e2022JC018965. https://doi.org/10.1029/2022JC018965

Gasser, T. and Ciais, P.: A theoretical framework for the net land-to-atmosphere CO2 flux and its implications in the definition of "emissions from land-use change", Earth Syst. Dynam., 4, 171–186, https://doi.org/10.5194/esd-4-171-2013, 2013.

GCCA. Concrete Future: The GCCA 2050 Cement and Concrete Industry Roadmap for Net Zero Concrete, available at: https://gccassociation.org/concretefuture/ last access: 2 August 2022, 2021.

Gkritzalis, T., Bakker, D. C. E., Lauvset, S. K. and Steinhoff, T. (2024) SOCAT Quality Control Cookbook – For version 2025 of the Surface Ocean CO2 Atlas. 26 pp. Published on 18/12/2024. Available here: https://socat.info/wp-content/uploads/2025/01/2024_SOCAT_QC_Cookbook_Update.pdf. Last access 22/05/2025.

Goddijn-Murphy, L. M., Woolf, D. K., Land, P. E., Shutler, J. D., and Donlon, C.: The OceanFlux Greenhouse Gases methodology for deriving a sea surface climatology of CO2 fugacity in support of air–sea gas flux studies, 11, 519–541, https://doi.org/10.5194/os-11-519-2015, 2015.

Golar, G., Malik, A., Muis, H., Herman, A., Nurudin, N., and Lukman, L.: The social-economic impact of COVID-19 pandemic: implications for potential forest degradation, Heliyon, 6, e05354, https://doi.org/10.1016/j.heliyon.2020.e05354, 2020.

Good, S. A., Martin, M. J., and Rayner, N. A.: EN4: Quality controlled ocean temperature and salinity profiles and monthly objective analyses with uncertainty estimates, Journal of Geophysical Research: Oceans, 118, 6704–6716, https://doi.org/10.1002/2013JC009067, 2013.

Gouretski, V. and Cheng, L.: Correction for Systematic Errors in the Global Dataset of Temperature Profiles from Mechanical Bathythermographs, Journal of Atmospheric and Oceanic Technology, 37, 841–855, https://doi.org/10.1175/JTECH-D-19-0205.1, 2020.

Gouretski, V. and Reseghetti, F.: On depth and temperature biases in bathythermograph data: Development of a new correction scheme based on analysis of a global ocean database, Deep Sea Research Part I: Oceanographic Research Papers, 57, 812–833, https://doi.org/10.1016/j.dsr.2010.03.011, 2010.

Grassi, G., House, J., Kurz, W. A., Cescatti, A., Houghton, R. A., Peters, G. P., Sanz, M. J., Viñas, R. A., Alkama, R., Arneth, A., Bondeau, A., Dentener, F., Fader, M., Federici, S., Friedlingstein, P., Jain, A. K., Kato, E., Koven, C. D., Lee, D., Nabel, J. E. M. S., Nassikas, A. A., Perugini, L., Rossi, S., Sitch, S., Viovy, N., Wiltshire, A., and Zaehle, S.: Reconciling global-model estimates and country reporting of anthropogenic forest CO2 sinks, Nature Clim Change, 8, 914–920, https://doi.org/10.1038/s41558-018-0283-x, 2018.

Grassi, G., Conchedda, G., Federici, S., Abad Viñas, R., Korosuo, A., Melo, J., Rossi, S., Sandker, M., Somogyi, Z., and Tubiello, F. N.: Carbon fluxes from land 2000–2020: bringing clarity on countries' reporting, Biogeosciences and biodiversity, https://doi.org/10.5194/essd-2022-104, 2022.

Grassi, G., Schwingshackl, C., Gasser, T., Houghton, R. A., Sitch, S., Canadell, J. G., Cescatti, A., Ciais, P., Federici, S., Friedlingstein, P., Kurz, W. A., Sanz Sanchez, M. J., Abad Viñas, R., Alkama, R., Bultan, S., Ceccherini, G., Falk, S., Kato, E., Kennedy, D., Knauer, J., Korosuo, A., Melo, J., McGrath, M. J., Nabel, J. E. M. S., Poulter, B., Romanovskaya, A. A., Rossi, S., Tian, H., Walker, A. P., Yuan, W., Yue, X., and Pongratz, J.: Harmonising the land-use flux estimates of global models and national inventories for 2000–2020, Earth Syst. Sci. Data, 15, 1093–1114, https://doi.org/10.5194/essd-15-1093-2023, 2023.

Gregg, J. S., Andres, R. J., and Marland, G.: China: Emissions pattern of the world leader in CO 2 emissions from fossil fuel consumption and cement production, Geophys. Res. Lett., 35, L08806, https://doi.org/10.1029/2007GL032887, 2008.

Gregor, Luke; Gruber, Nicolas (2020). OceanSODA-ETHZ: A global gridded dataset of the surface ocean carbonate system for seasonal to decadal studies of ocean acidification (v2023) (NCEI Accession 0220059). [indicate subset used]. NOAA National Centers for Environmental Information. Dataset. https://doi.org/10.25921/m5wx-ja34. Accessed 24 October 2025.

Gregor, L. and Gruber, N.: OceanSODA-ETHZ: a global gridded data set of the surface ocean carbonate system for seasonal to decadal studies of ocean acidification, Earth System Science Data, 13, 777–808, https://doi.org/10.5194/essd-13-777-2021, 2021.

Gkritzalis, T., T'Jampens, M., and Theetaert, H.: Simon Stevin 2025: Simon Stevin surface ocean and atmospheric fCO_2 observations taken by custom instrument with Licor 7815 gas analyzer in 2025, ICOS ERIC -- Carbon Portal [data set], https://doi.org/10.18160/RJKN-RTFU, 2026.

Gruber, N., Clement, D., Carter, B. R., Feely, R. A., van Heuven, S., Hoppema, M., Ishii, M., Key, R. M., Kozyr, A., Lauvset, S. K., Lo Monaco, C., Mathis, J. T., Murata, A., Olsen, A., Pérez, F. F., Sabine, C. L., Tanhua, T., and Wanninkhof, R.: The oceanic sink for anthropogenic CO2 from 1994 to 2007, Science, 363, 1193–1199, https://doi.org/10.1126/science.aau5153, 2019.

Gürses, Ö., Oziel, L., Karakuş, O., Sidorenko, D., Völker, C., Ye, Y., Zeising, M., Butzin, M., and Hauck, J.: Ocean biogeochemistry in the coupled ocean–sea ice–biogeochemistry model FESOM2.1–REcoM3, Geoscientific Model Development, 16, 4883–4936, https://doi.org/10.5194/gmd-16-4883-2023, 2023.

Hamnca, S., Tsanwani, M., and Mdokwana, B.: Partial pressure (or fugacity) of carbon dioxide, water temperature, salinity and other variables collected from surface underway observations during the SA Agulhas II cruise in the South Atlantic Ocean, Indian Ocean from 2025-04-18 to 2025-05-13 (NCEI Accession 0315102), NOAA National Centers for Environmental Information [data set], https://doi.org/10.25921/2yd3-vv23, 2026.

Hansen, M. C., Potapov, P. V., Moore, R., Hancher, M., Turubanova, S. A., Tyukavina, A., Thau, D., Stehman, S. V., Goetz, S. J., Loveland, T. R., Kommareddy, A., Egorov, A., Chini, L., Justice, C. O., and Townshend, J. R. G.: High-Resolution Global Maps of 21st-Century Forest Cover Change, Science, 342, 850–853, https://doi.org/10.1126/science.1244693, 2013.

Harris, I., Jones, P. D., Osborn, T. J., and Lister, D. H.: Updated high-resolution grids of monthly climatic observations - the CRU TS3.10 Dataset, Int. J. Climatol., 34, 623–642, https://doi.org/10.1002/joc.3711, 2014.

Harris, I., Osborn, T. J., Jones, P., and Lister, D.: Version 4 of the CRU TS monthly high-resolution gridded multivariate climate dataset, Sci Data, 7, 109, https://doi.org/10.1038/s41597-020-0453-3, 2020.

Hartman, S. E., Flohr, A., and Phillips, D. P.: Partial pressure of carbon dioxide, sea surface salinity, water temperature and other parameters collected from surface underway observations during the RRS James Cook JC278 (EXPOCODE 740H20250530) in the North Atlantic Ocean and Celtic Sea from 30 May to 22 June 2025 (NCEI Accession 0312066), NOAA National Centers for Environmental Information [data set], https://doi.org/10.25921/9xgt-t091, 2026.

Hashimoto, S., Carvalhais, N., Ito, A., Migliavacca, M., Nishina, K. and Reichstein, M.: Global spatiotemporal distribution of soil respiration modeled using a global database. Biogeosciences, 12(13), pp.4121-4132, 2015.

Hashimoto, S., Ito, A. and Nishina, K.: Divergent data-driven estimates of global soil respiration. Communications Earth & Environment, 4(1), p.460, 2023.

Hefner, M., Marland, G., Boden, T., Andres, R.: Global, Regional, and National Fossil-Fuel CO2 Emissions: 1751-2020 CDIAC-FF, Appalachian Energy Centre [data set], available at: https://energy.appstate.edu/cdiac-appstate/data-products, last access: 21 January 2025, 2023.

2015 Heinimann, A., Mertz, O., Frolking, S., Christensen, A. E., Hurni, K., Sedano, F., Chini, L. P., Sahajpal, R., Hansen, M., and
2016 Hurtt, G.: A global view of shifting cultivation: Recent, current, and future extent, PLOS ONE, 12, e0184479,
2017 https://doi.org/10.1371/journal.pone.0184479, 2017.

2018 Hersbach, H., Bell, B., Berrisford, P., Hirahara, S., Horányi, A., Muñoz-Sabater, J., ... & Thépaut, J. N.: The ERA5 global
2019 reanalysis. Quarterly Journal of the Royal Meteorological Society, 146(730), 1999-2049, 2020.

2020 Hertwich, E. G. and Peters, G. P.: Carbon Footprint of Nations: A Global, Trade-Linked Analysis, Environ. Sci. Technol.,
2021 43, 6414–6420, https://doi.org/10.1021/es803496a, 2009.

2022 Ho, D. T., Wanninkhof, R., Schlosser, P., Ullman, D. S., Hebert, D., and Sullivan, K. F.: Toward a universal relationship
2023 between wind speed and gas exchange: Gas transfer velocities measured with 3He/SF6 during the Southern Ocean Gas
2024 Exchange Experiment, J. Geophys. Res.-Oceans, 116, C00F04, https://doi.org/10.1029/2010JC006854, 2011.

2025 Hobeichi, S., Abramowitz, G., Evans, J., and Beck, H. E.: Linear Optimal Runoff Aggregate (LORA): a global gridded
2026 synthesis runoff product, Hydrol. Earth Syst. Sci., 23, 851–870, https://doi.org/10.5194/hess-23-851-2019, 2019.

2027 Hobeichi, S., Abramowitz, G., and Evans, J.: Conserving Land–Atmosphere Synthesis Suite (CLASS), Journal of Climate,
2028 33, 1821–1844, https://doi.org/10.1175/JCLI-D-19-0036.1, 2020.

2029 Houghton, R. A.: Why are estimates of the terrestrial carbon balance so different?, Glob. Change Biol., 9, 500–509,
2030 https://doi.org/10.1046/j.1365-2486.2003.00620.x, 2003.

2031 Houghton, R. A. and Nassikas, A. A.: Global and regional fluxes of carbon from land use and land cover change 1850-2015:
2032 Carbon Emissions From Land Use, Global Biogeochem. Cycles, 31, 456–472, https://doi.org/10.1002/2016GB005546,
2033 2017.

2034 Hauck, J., Gregor, L., Nissen, C., Patara, L., Hague, M., Mongwe, P., Bushinsky, S., Doney, S. C., Gruber, N., Le Quéré, C.,
2035 Manizza, M., Mazloff, M., Monteiro, P. M. S., & Terhaar, J.: The Southern Ocean Carbon Cycle 1985–2018: Mean,
2036 Seasonal Cycle, Trends, and Storage. Global Biogeochemical Cycles, 37(11), e2023GB007848.
2037 https://doi.org/10.1029/2023GB007848, 2023b.

2038 Huang, Z., Wang, J., Bing, L., Qiu, Y., Guo, R., Yu, Y., Ma, M., Niu, L., Tong, D., Andrew, R. M., Friedlingstein, P.,
2039 Canadell, J. G., Xi, F., and Liu, Z.: Global carbon uptake of cement carbonation accounts 1930–2021, Earth Syst. Sci. Data,
2040 15, 4947–4958, https://doi.org/10.5194/essd-15-4947-2023, 2023.

2041 Hugelius, G., Bockheim, J. G., Camill, P., Elberling, B., Grosse, G., Harden, J. W., Johnson, K., Jorgenson, T., Koven, C.
2042 D., Kuhry, P., Michaelson, G., Mishra, U., Palmtag, J., Ping, C.-L., O'Donnell, J., Schirrmeister, L., Schuur, E. A. G.,
2043 Sheng, Y., Smith, L. C., Strauss, J., and Yu, Z.: A new data set for estimating organic carbon storage to 3 m depth in soils of
2044 the northern circumpolar permafrost region, Earth Syst. Sci. Data, 5, 393–402, https://doi.org/10.5194/essd-5-393-2013,
2045 2013.

2046 Hui, D., & Jackson, R. B. (2006). Geographical and interannual variability in biomass partitioning in grassland ecosystems:
2047 a modeling analysis. Proceedings of the National Academy of Sciences of the United States of America (PNAS), 103(39),
2048 14271–14275. https://doi.org/10.1073/pnas.0604342103

2049 Humphreys, M. P., Lewis, E. R., Sharp, J. D., and Pierrot, D.: PyCO2SYS v1.8: marine carbonate system calculations in
2050 Python, Geosci. Model Dev., 15, 15–43, https://doi.org/10.5194/gmd-15-15-2022, 2022.

2051 Hurtt, G., Chini, L., Sahajpal, R., Frolking, S., Bodirsky, B. L., Calvin, K., Doelman, J., Fisk, J., Fujimori, S., Klein
2052 Goldewijk, K., Hasegawa, T., Havlik, P., Heinimann, A., Humpenöder, F., Jungclaus, J., Kaplan, J., Krisztin, T., Lawrence,
2053 D., Lawrence, P., Mertz, O., Pongratz, J., Popp, A., Riahi, K., Shevliakova, E., Stehfest, E., Thornton, P., van Vuuren, D.,
2054 and Zhang, X.: input4MIPs.CMIP6.CMIP.UofMD.UofMD-landState-2-1-h, World Climate Research Programme [dataset],
2055 https://doi.org/10.22033/ESGF/input4MIPs.1127, 2017.

2056 Hurtt, G. C., Chini, L. P., Frolking, S., Betts, R. A., Feddema, J., Fischer, G., Fisk, J. P., Hibbard, K., Houghton, R. A.,
2057 Janetos, A., Jones, C. D., Kindermann, G., Kinoshita, T., Klein Goldewijk, K., Riahi, K., Shevliakova, E., Smith, S.,
2058 Stehfest, E., Thomson, A., Thornton, P., van Vuuren, D. P., and Wang, Y. P.: Harmonization of land-use scenarios for the
2059 period 1500–2100: 600 years of global gridded annual land-use transitions, wood harvest, and resulting secondary lands,
2060 Climatic Change, 109, 117–161, https://doi.org/10.1007/s10584-011-0153-2, 2011.

2061 Hurtt, G. C., Chini, L., Sahajpal, R., Frolking, S., Bodirsky, B. L., Calvin, K., Doelman, J. C., Fisk, J., Fujimori, S., Klein
2062 Goldewijk, K., Hasegawa, T., Havlik, P., Heinimann, A., Humpenöder, F., Jungclaus, J., Kaplan, J. O., Kennedy, J.,
2063 Krisztin, T., Lawrence, D., Lawrence, P., Ma, L., Mertz, O., Pongratz, J., Popp, A., Poulter, B., Riahi, K., Shevliakova, E.,
2064 Stehfest, E., Thornton, P., Tubiello, F. N., van Vuuren, D. P., and Zhang, X.: Harmonization of global land use change and
2065 management for the period 850–2100 (LUH2) for CMIP6, Geosci. Model Dev., 13, 5425–5464,
2066 https://doi.org/10.5194/gmd-13-5425-2020, 2020.

IEA/OECD: International Energy Agency/Organisation for Economic Cooperation and Development: CO2 emissions from fuel combustion, available at: https://webstore.iea.org/co2-emissions-from-fuel-combustion-2019-highlights, last access: 21 January 2025, 2019.

Iida, Y., Kojima, A., Takatani, Y., Nakano, T., Sugimoto, H., Midorikawa, T., and Ishii, M.: Trends in pCO2 and sea–air CO2 flux over the global open oceans for the last two decades, J Oceanogr, 71, 637–661, https://doi.org/10.1007/s10872-015-0306-4, 2015.

Iida, Y., Takatani, Y., Kojima, A., and Ishii, M.: Global trends of ocean CO2 sink and ocean acidification: an observation-based reconstruction of surface ocean inorganic carbon variables, J. Oceanogr., 77, 323–358, https://doi.org/10.1007/s10872-020-00571-5, 2021.

Ilyina, T., Six, K. D., Segschneider, J., Maier-Reimer, E., Li, H., and Núñez-Riboni, I.: Global ocean biogeochemistry model HAMOCC: Model architecture and performance as component of the MPI-Earth system model in different CMIP5 experimental realizations: The Model Hamocc within Mpi-Esm in Cmip5, J. Adv. Model. Earth Syst., 5, 287–315, https://doi.org/10.1029/2012MS000178, 2013.

Inness, A., Ades, M., Agustí-Panareda, A., Barré, J., Benedictow, A., Blechschmidt, A.-M., Dominguez, J. J., Engelen, R., Eskes, H., Flemming, J., Huijnen, V., Jones, L., Kipling, Z., Massart, S., Parrington, M., Peuch, V.-H., Razinger, M., Remy, S., Schulz, M., and Suttie, M.: The CAMS reanalysis of atmospheric composition, 19, 3515–3556, https://doi.org/10.5194/acp-19-3515-2019, 2019.

Intergovernmental Panel on Climate Change (IPCC): Climate Change 2021: The Physical Science Basis. Contribution of Working Group I to the Sixth Assessment Report of the Intergovernmental Panel on Climate Change. Edited by V. Masson-Delmotte, P. Zhai, A. Pirani, S. L. Connors, C. Péan, S. Berger, N. Caud, Y. Chen, L. Goldfarb, M. I. Gomis, M. Huang, K. Leitzell, E. Lonnoy, J. B. R. Matthews, T. K. Maycock, T. Waterfield, O. Yelekçi, R. Yu, and B. Zhou. Cambridge University Press, Cambridge, UK and New York, NY, USA. https://doi.org/10.1017/9781009157896, 2021.

Intergovernmental Panel on Climate Change (IPCC): 2006 IPCC Guidelines for National Greenhouse Gas Inventories, Prepared by the National Greenhouse Gas Inventories Programme, Eggleston H.S., Buendia L., Miwa K., Ngara T. and Tanabe K. (eds). Published: IGES, Japan, 2006.

Ishii, M., and M., Kimoto: Reevaluation of historical ocean heat content variations with time-varying XBT and MBT depth bias corrections. Journal of Oceanography, 65(3), 287–299, 2009.

Iversen, C. M., McCormack, M. L., Powell, A. S., Blackwood, C. B., Freschet, G. T., Kattge, J., Roumet, C., Stover, D. B., Soudzilovskaia, N. A., Valverde-Barrantes, O. J., van Bodegom, P. M., & Violle, C. (2017). A global fine-root ecology database to address below-ground challenges in plant ecology. New Phytologist, 215, 15-26. https://doi.org/10.1111/nph.14486

Jackson, R. B., Lajtha, K., Crow, S. E., Hugelius, G., Kramer, M. G., & Piñeiro, G. (2017). The ecology of soil carbon: pools, vulnerabilities, and biotic and abiotic controls. Annual Review of Ecology, Evolution, and Systematics, 48, 419-445. https://doi.org/10.1146/annurev-ecolsys-112414-054234

Jähne, B.: Air-Sea Gas Exchange, in: Encyclopedia of Ocean Sciences, Elsevier, 1–13, https://doi.org/10.1016/B978-0-12-409548-9.11613-6, 2019.

Jähne, B. and Haußecker, H.: Air-water gas exchange, Annu. Rev. Fluid Mech., 30, 443–468, https://doi.org/10.1146/annurev.fluid.30.1.443, 1998.

JODI: Joint Organisations Data Initiative, available at: https://www. jodidata.org, last access: 21 January 2025, 2022.

Jones, M.W., Andrew, R.M., Peters, G.P. et al., 2021: Gridded fossil CO2 emissions and related O2 combustion consistent with national inventories 1959–2018. Sci Data 8, 2. https://doi.org/10.1038/s41597-020-00779-6

Jones, M. W., Andrew, R. M., Peters, G. P., Janssens-Maenhout, G., De-Gol, A. J., Dou, X., Liu, Z., Pickers, P., Ciais, P., Patra, P. K., Chevallier, F., and Le Quéré, C.: Gridded fossil CO2 emissions and related O2 combustion consistent with national inventories 1959-2022, Zenodo [dataset], https://doi.org/10.5281/zenodo.8386803, 2023.

Jung, M., Reichstein, M., Schwalm, C. R., Huntingford, C., Sitch, S., Ahlström, A., Arneth, A., Camps-Valls, G., Ciais, P., Friedlingstein, P., Gans, F., Ichii, K., Jain, A. K., Kato, E., Papale, D., Poulter, B., Raduly, B., Rödenbeck, C., Tramontana, G., Viovy, N., Wang, Y.-P., Weber, U., Zaehle, S., and Zeng, N.: Compensatory water effects link yearly global land CO2 sink changes to temperature, Nature, 541, 516–520, https://doi.org/10.1038/nature20780, 2017.

Kadono, K. and Enyo, K.: Partial pressure of carbon dioxide, salinity, temperature and other variables collected from surface underway observations using carbon dioxide (CO_2) gas analyzer, shower head chamber equilibrator for autonomous CO_2

measurement and other instruments from R/V Keifu Maru II in the Pacific Ocean in 2025 (NCEI Accession 0311803), NOAA National Centers for Environmental Information [data set], https://doi.org/10.25921/5z8d-2e87, 2026.

Keppler, L., Landschützer, P., Lauvset, S. K., and Gruber, N.: Recent Trends and Variability in the Oceanic Storage of Dissolved Inorganic Carbon, Global Biogeochemical Cycles, 37, e2022GB007677, https://doi.org/10.1029/2022GB007677, 2023.

Keeling, R. F. and Manning, A. C.: 5.15 - Studies of Recent Changes in Atmospheric O2 Content, in: Treatise on Geochemistry (Second Edition), edited by: Holland, H. D. and Turekian, K. K., Elsevier, Oxford, 385–404, https://doi.org/10.1016/B978-0-08-095975-7.00420-4, 2014.

Khatiwala, S., Tanhua, T., Mikaloff Fletcher, S., Gerber, M., Doney, S. C., Graven, H. D., Gruber, N., McKinley, G. A., Murata, A., Ríos, A. F., & Sabine, C. L. (2013). Global ocean storage of anthropogenic carbon. Biogeosciences, 10(4), 2169–2191. https://doi.org/10.5194/bg-10-2169-2013

Klein Goldewijk, K., Beusen, A., Doelman, J., and Stehfest, E.: Anthropogenic land use estimates for the Holocene – HYDE 3.2, Earth Syst. Sci. Data, 9, 927–953, https://doi.org/10.5194/essd-9-927-2017, 2017a.

Klein Goldewijk, K., Dekker, S. C., and van Zanden, J. L.: Per-capita estimations of long-term historical land use and the consequences for global change research, J. Land Use Sci., 12, 313–337, https://doi.org/10.1080/1747423X.2017.1354938, 2017b.

Knauer, J., Zaehle, S., Medlyn, B. E., Reichstein, M., Williams, C. A., Migliavacca, M., De Kauwe, M. G., Werner, C., Keitel, C., Kolari, P., Limousin, J., and Linderson, M.: Towards physiologically meaningful water-use efficiency estimates from eddy covariance data, Global Change Biology, 24, 694–710, https://doi.org/10.1111/gcb.13893, 2018.

Kobayashi, S., Ota, Y., Harada, Y., Ebita, A., Moriya, M., Onoda, H., Onogi, K., Kamahori, H., Kobayashi, C., Endo, H., Miyaoka, K., and Takahashi, K.: The JRA-55 Reanalysis: General Specifications and Basic Characteristics, Journal of the Meteorological Society of Japan, 93, 5–48, https://doi.org/10.2151/jmsj.2015-001, 2015.

Koven, C., Hugelius, G., Lawrence, D. et al. Higher climatological temperature sensitivity of soil carbon in cold than warm climates. Nature Clim Change 7, 817–822,. https://doi.org/10.1038/nclimate3421, 2017,

Lamboll, R. D., Jones, C. D., Skeie, R. B., Fiedler, S., Samset, B. H., Gillett, N. P., Rogelj, J., Forster, P. M.: Modifying emissions scenario projections to account for the effects of COVID-19: protocol for CovidMIP, Geosci. Model Dev., 14, 3683–3695, https://doi.org/10.5194/gmd-14-3683-2021, 2021.

Landschützer, P., Gruber, N., Bakker, D. C. E., and Schuster, U.: Recent variability of the global ocean carbon sink, Global Biogeochem. Cycles, 28, 927–949, https://doi.org/10.1002/2014GB004853, 2014.

Landschützer, P., Laruelle, G. G., Roobaert, A., and Regnier, P.: A uniform pCO2 climatology combining open and coastal oceans, 12, 2537–2553, https://doi.org/10.5194/essd-12-2537-2020, 2020.

Lasslop, G., Reichstein, M., Papale, D., Richardson, A. D., Arneth, A., Barr, A., Stoy, P., and Wohlfahrt, G.: Separation of net ecosystem exchange into assimilation and respiration using a light response curve approach: critical issues and global evaluation: Separation of NEE into GPP and RECO, Glob. Change Biol., 16, 187–208, https://doi.org/10.1111/j.1365-2486.2009.02041.x, 2010.

Lauvset, S. K., Key, R. M., Olsen, A., van Heuven, S., Velo, A., Lin, X., Schirnick, C., Kozyr, A., Tanhua, T., Hoppema, M., Jutterström, S., Steinfeldt, R., Jeansson, E., Ishii, M., Perez, F. F., Suzuki, T., and Watelet, S.: A new global interior ocean mapped climatology: the 1° × 1° GLODAP version 2, Earth System Science Data, 8, 325–340, https://doi.org/10.5194/essd-8-325-2016, 2016.

Lauvset, S. K., Lange, N., Tanhua, T., Bittig, H. C., Olsen, A., Kozyr, A., Alin, S., Álvarez, M., Azetsu-Scott, K., Barbero, L., Becker, S., Brown, P. J., Carter, B. R., Da Cunha, L. C., Feely, R. A., Hoppema, M., Humphreys, M. P., Ishii, M., Jeansson, E., Jiang, L.-Q., Jones, S. D., Lo Monaco, C., Murata, A., Müller, J. D., Pérez, F. F., Pfeil, B., Schirnick, C., Steinfeldt, R., Suzuki, T., Tilbrook, B., Ulfsbo, A., Velo, A., Woosley, R. J., and Key, R. M.: GLODAPv2.2022: the latest version of the global interior ocean biogeochemical data product, Earth Syst. Sci. Data, 14, 5543–5572, https://doi.org/10.5194/essd-14-5543-2022, 2022.

Lauvset, S. K., Lange, N., Tanhua, T., Bittig, H. C., Olsen, A., Kozyr, A., Álvarez, M., Azetsu-Scott, K., Brown, P. J., Carter, B. R., Cotrim da Cunha, L., Hoppema, M., Humphreys, M. P., Ishii, M., Jeansson, E., Murata, A., Müller, J. D., Pérez, F. F., Schirnick, C., Steinfeldt, R., Suzuki, T., Ulfsbo, A., Velo, A., Woosley, R. J., and Key, R. M.: The annual update GLODAPv2.2023: the global interior ocean biogeochemical data product, Earth Syst. Sci. Data, 16, 2047–2072, https://doi.org/10.5194/essd-16-2047-2024, 2024

Lienert, S. and Joos, F.: A Bayesian ensemble data assimilation to constrain model parameters and land-use carbon emissions, Biogeosciences, 15, 2909–2930, https://doi.org/10.5194/bg-15-2909-2018, 2018.

Li, H., Ilyina, T., Loughran, T., Spring, A., and Pongratz, J.: Reconstructions and predictions of the global carbon budget with an emission-driven Earth system model, Earth Syst. Dyn., 14, 101–119, https://doi.org/10.5194/esd-14-101-2023, 2023.

Liptak, J., Keppel-Aleks, G., and Lindsay, K. (2017) Drivers of multi-century trends in the atmospheric CO2 mean annual cycle in a prognostic ESM. Biogeosciences, 14, 1383–1401 https://bg.copernicus.org/articles/14/1383/2017/bg-14-1383-2017.pdf

Liu, Z., Ciais, P., Deng, Z., Davis, S. J., Zheng, B., Wang, Y., Cui, D., Zhu, B., Dou, X., Ke, P., Sun, T., Guo, R., Zhong, H., Boucher, O., Bréon, F.-M., Lu, C., Guo, R., Xue, J., Boucher, E., Tanaka, K., and Chevallier, F.: Carbon Monitor, a near-real-time daily dataset of global CO2 emission from fossil fuel and cement production, Sci Data, 7, 392, https://doi.org/10.1038/s41597-020-00708-7, 2020a.

Liu, Z., Ciais, P., Deng, Z., Lei, R. Davis, S. J., Feng, S., Zheng, B., Cui, D., Dou, X., Zhu, B., Guo, R., Ke, P., Sun, T., Lu, C., He, P., Wang, Y., Yue, X., Wang, Y., Lei, Y., Zhou, H., Cai, Z., Wu, Y., Guo, R., Han, T., Xue, J., Boucher, O., Boucher, E., Chevallier, F., Tanaka, K., Wei, Y., Zhong, H., Kang, C., Zhang, N., Chen, B., Xi, F., Liu, M., Bréon, F.-M., Lu, Y., Zhang, Q., Guan, D., Gong, P., Kammen, D. M., He, K., and Schellnhuber, H. J.: Near-real-time monitoring of global CO2 emissions reveals the effects of the COVID-19 pandemic, Nat Commun, 11, 5172, https://doi.org/10.1038/s41467-020-18922-7, 2020b.

Locarnini, R.A., A.V. Mishonov, O.K. Baranova, J.R. Reagan, T.P. Boyer, D. Seidov, Z. Wang, H.E. Garcia, C. Bouchard, S.L. Cross, C.R. Paver, and D. Dukhovskoy. World Ocean Atlas 2023, Volume 1: Temperature. A. Mishonov Technical Ed. NOAA Atlas NESDIS 89, doi.org/10.25923/54bh-1613

Lo Monaco, C. and Metzl, N.: Surface underway measurements of partial pressure of carbon dioxide (pCO_2), salinity, water temperature and other associated parameters during the R/V Marion Dufresne OISO-35 cruise (EXPOCODE 35MV20241225) in the Indian Ocean from 2024-12-25 to 2025-02-02 (NCEI Accession 0311456), NOAA National Centers for Environmental Information [data set], https://doi.org/10.25921/ztee-xr07, 2026.

Lueker, T. J., Dickson, A. G., and Keeling, C. D.: Ocean pCO2 calculated from dissolved inorganic carbon, alkalinity, and equations for K1 and K2: validation based on laboratory measurements of CO2 in gas and seawater at equilibrium, Mar. Chem., 70, 105–119, https://doi.org/10.1016/S0304-4203(00)00022-0, 2000.

Ma, L., Hurtt, G. C., Chini, L. P., Sahajpal, R., Pongratz, J., Frolking, S., Stehfest, E., Klein Goldewijk, K., O'Leary, D., and Doelman, J. C.: Global rules for translating land-use change (LUH2) to land-cover change for CMIP6 using GLM2, Geosci. Model Dev., 13, 3203–3220, https://doi.org/10.5194/gmd-13-3203-2020, 2020.

Maki, T., Ikegami, M., Fujita, T., Hirahara, T., Yamada, K., Mori, K., Takeuchi, A., Tsutsumi, Y., Suda, K., and Conway, T. J.: New technique to analyse global distributions of CO2 concentrations and fluxes from non-processed observational data, Tellus B., 62, 797–809, https://doi.org/10.1111/j.1600-0889.2010.00488.x, 2010.

MapBiomas Brasil. Collection 9 of annual maps of land cover and land use in Brazil, accessed on 04/2025 through the link: https://brasil.mapbiomas.org/estatisticas/

MapBiomas Indonesia. Collection 3 of annual maps of land cover and land use in Indonesia, accessed on 03/2025 through the link: https://platform.indonesia.mapbiomas.org/

Matsumoto, K., Sarmiento, J. L., Key, R. M., Aumont, O., Bullister, J. L., Caldeira, K., Campin, J.-M., Doney, S. C., Drange, H., Dutay, J.-C., Follows, M., Gao, Y., Gnanadesikan, A., Gruber, N., Ishida, A., Joos, F., Lindsay, K., Maier-Reimer, E., Marshall, J. C., Matear, R. J., Monfray, P., Mouchet, A., Najjar, R., Plattner, G.-K., Schlitzer, R., Slater, R., Swathi, P. S., Totterdell, I. J., Weirig, M.-F., Yamanaka, Y., Yool, A., and Orr, J. C.: Evaluation of ocean carbon cycle models with data-based metrics, Geophys. Res. Lett., 31, L07303, https://doi.org/10.1029/2003GL018970, 2004.

McCarthy, G. D., Smeed, D. A., Johns, W. E., Frajka-Williams, E., Moat, B. I., Rayner, D., Baringer, M. O., Meinen, C. S., Collins, J., & Bryden, H. L. (2015). Measuring the Atlantic Meridional Overturning Circulation at 26°N. Progress in Oceanography, 130, 91–111. https://doi.org/10.1016/j.pocean.2014.10.006

McKinley, G. A., Fay, A. R., Heimdal, T. H., Moseley, L. A., and Shaum, A. P.: How well do global ocean approaches constrain local fCO2?, Environ. Res. Lett., 21, 134011, https://doi.org/10.1088/1748-9326/ae803e, 2026.

Melo, J., Rossi, S., Achard, F., Alkama, R., Canadell, J. G., Federici, S., Friedlingstein, P., Gibbs, D., Harris, N., Heinrich, V., O'Sullivan, M., Peters, G. P., Pongratz, J., Rose, M., Roman-Cuesta, R., Sanz, M. J., Schwingshackl, C., Sitch, S., and Grassi, G.: The LULUCF Data Hub: translating global land use emissions estimates into the national GHG inventory framework, Earth Syst. Sci. Data Discuss. [preprint], https://doi.org/10.5194/essd-2025-631, in review, 2026a.

Melo, J., Rossi, S., Achard, F., Alkama, R., Canadell, J. G., Federici, S., Friedlingstein, P., Gibbs, D., Harris, N., Heinrich, V., O'Sullivan, M., Peters, G., Pongratz, J., Rose, M., Roman-Cuesta, R., Sanz Sanchez, M. J., Schwingshackl, C., Sitch, S., & Grassi, G. (2026). The LULUCF Data Hub: translating global land use emissions estimates into the national GHG inventory framework (Version 4.1.0, 2026 NGHGI release) (Version 4.1.0) [Dataset]. Zenodo. https://doi.org/10.5281/zenodo.17140775, 2026b.

Mokany, K., Raison, R. J., & Prokushkin, A. S. (2006). Critical analysis of root:shoot ratios in terrestrial biomes. Global Change Biology, 15, 129-144. doi: 10.1111/j.1365-2486.2005.001043.x

Manning, A. and Keeling, R. F.: Global oceanic and land biotic carbon sinks from the Scripps atmospheric oxygen flask sampling network, Tellus B Chem. Phys. Meteorol., 58, 95–116, https://doi.org/10.1111/j.1600-0889.2006.00175.x, 2006.

Marland, G.: Uncertainties in Accounting for CO 2 From Fossil Fuels, J. Indust. Ecol., 12, 136–139, https://doi.org/10.1111/j.1530-9290.2008.00014.x, 2008.

Marland, G., Hamal, K., and Jonas, M.: How Uncertain Are Estimates of CO2 Emissions?, J. Indust. Ecol., 13, 4–7, https://doi.org/10.1111/j.1530-9290.2009.00108.x, 2009.

Martens, B., Miralles, D. G., Lievens, H., Van Der Schalie, R., De Jeu, R. A. M., Fernández-Prieto, D., Beck, H. E., Dorigo, W. A., and Verhoest, N. E. C.: GLEAM v3: satellite-based land evaporation and root-zone soil moisture, Geosci. Model Dev., 10, 1903–1925, https://doi.org/10.5194/gmd-10-1903-2017, 2017.

Mauritsen, T. et al.: Developments in the MPI-M Earth System Model version 1.2 (MPI-ESM1. 2) and its response to increasing CO2. Journal of Advances in Modeling Earth Systems, 11 (4), 998–1038, 2019.

McNeil, B. I.: Anthropogenic CO2 Uptake by the Ocean Based on the Global Chlorofluorocarbon Data Set, Science, 299, 235–239, https://doi.org/10.1126/science.1077429, 2003.

Mikaloff Fletcher, S. E., Gruber, N., Jacobson, A. R., Doney, S. C., Dutkiewicz, S., Gerber, M., Follows, M., Joos, F., Lindsay, K., Menemenlis, D., Mouchet, A., Müller, S. A., and Sarmiento, J. L.: Inverse estimates of anthropogenic CO2 uptake, transport, and storage by the ocean, Glob. Biogeochem. Cycles, 20, GB2002, https://doi.org/10.1029/2005GB002530, 2006.

Miralles, D. G., Holmes, T. R. H., De Jeu, R. A. M., Gash, J. H., Meesters, A. G. C. A., and Dolman, A. J.: Global land-surface evaporation estimated from satellite-based observations, Hydrol. Earth Syst. Sci., 15, 453–469, https://doi.org/10.5194/hess-15-453-2011, 2011.

Moat B.I.; Smeed D.A.; Rayner D.; Johns W.E.; Smith, R.; Volkov, D.; Elipot S.; Petit T.; Kajtar J.; Baringer M. O.; and Collins, J. (2025). Atlantic meridional overturning circulation observed by the RAPID-MOCHA-WBTS (RAPID-Meridional Overturning Circulation and Heatflux Array-Western Boundary Time Series) array at 26N from 2004 to 2024 (v2024.1), British Oceanographic Data Centre - Natural Environment Research Council, UK. doi: 10.5285/3f24651e-2d44-dee3-e063-7086abc0395e

Monacci, N. M., Battisti, R., Bell, S., Bott, R., Dougherty, S., Osborne, J., Stabeno, P. J., Strausz, D., and Sutton, A.: High-resolution ocean and atmosphere pCO_2 time-series measurements from mooring M2_164W_57N, NOAA National Centers for Environmental Information [data set], https://doi.org/10.3334/cdiac/otg.tsm_m2_164w_57n, 2025a.

Monacci, N. M., Battisti, R., Bott, R., Osborne, J., and Sutton, A.: High-resolution ocean and atmosphere pCO_2 time-series measurements from mooring GAKOA_149W_60N, NOAA National Centers for Environmental Information [data set], https://doi.org/10.3334/cdiac/otg.tsm_gakoa_149w_60n, 2025b.

Mu, Q., Zhao, M., and Running, S. W.: Improvements to a MODIS global terrestrial evapotranspiration algorithm, Remote Sensing of Environment, 115, 1781–1800, https://doi.org/10.1016/j.rse.2011.02.019, 2011.

Müller, J. and Joos, F.: Global peatland area and carbon dynamics from the Last Glacial Maximum to the present – a process-based model investigation, Biogeosciences, 17, 5285–5308, https://doi.org/10.5194/bg-17-5285-2020, 2020.

Müller, J. and Joos, F.: Committed and projected future changes in global peatlands – continued transient model simulations since the Last Glacial Maximum, Biogeosciences, 18, 3657–3687, https://doi.org/10.5194/bg-18-3657-2021, 2021.

Müller, J. D., Gruber, N., Carter, B., Feely, R., Ishii, M., Lange, N., Lauvset, S. K., Murata, A., Olsen, A., Pérez, F. F., Sabine, C., Tanhua, T., Wanninkhof, R., and Zhu, D.: Decadal trends in the oceanic storage of anthropogenic carbon from 1994 to 2014, AGU Adv., 4, e2023AV000875, https://doi.org/10.1029/2023AV000875, 2023.

Myneni, R. B., Ramakrishna, R., Nemani, R., and Running, S. W.: Estimation of global leaf area index and absorbed par using radiative transfer models, IEEE Trans. Geosci. Remote Sensing, 35, 1380–1393, https://doi.org/10.1109/36.649788, 1997.

Naegler, T.: Reconciliation of excess 14C-constrained global CO2 piston velocity estimates, Tellus B., 61, 372–384, https://doi.org/10.1111/j.1600-0889.2008.00408.x, 2009.

Nakamura, T., Yamazaki, K., Iwamoto, K., Honda, M., Miyoshi, Y., Ogawa, Y., and Ukita, J.: A negative phase shift of the winter AO/NAO due to the recent Arctic sea-ice reduction in late autumn, J. Geophys. Res. Atmos., 120, 3209–3227, https://doi.org/10.1002/2014JD022848, 2015.

Nakaoka, S.-I., Takao, S., and Wada, C.: Surface underway measurements of partial pressure of carbon dioxide (pCO_2), sea surface salinity, temperature and other parameters during the ship of opportunity (SOOP) M/S New Century 2 cruises in the Pacific Ocean, Atlantic Ocean, Caribbean Sea in 2025 (NCEI Accession 0315165), NOAA National Centers for Environmental Information [data set], https://doi.org/10.25921/c5kn-5a07, 2026a.

Nakaoka, S.-I., Takao, S., and Wada, C.: Surface underway measurements of partial pressure of carbon dioxide (pCO_2), sea surface salinity, temperature and other parameters obtained during the ship of opportunity (SOOP) M/S Trans Future-5 cruises in the Pacific Ocean in 2025 (NCEI Accession 0315166), NOAA National Centers for Environmental Information [data set], https://doi.org/10.25921/h5rp-2r03, 2026b.

Narayanan, B., Aguiar, A., and McDougall, R.: Global Trade, Assistance, and Production: The GTAP 9 Data Base, Cent. Glob. Trade Anal. Purdue Univ., available at: https:// www.gtap.agecon.purdue.edu/databases/v9/default.asp, last access: 21 January 2025, 2015.

Nightingale, P. D., Liss, P. S., and Schlosser, P.: Measurements of air-sea gas transfer during an open ocean algal bloom, Geophys. Res. Lett., 27, 2117–2120, https://doi.org/10.1029/2000GL011541, 2000.

Ogunro, O. O., Elliott, S. M., Wingenter, O. W., Deal, C., Fu, W., Collier, N., & Hoffman, F. M. (2018). Evaluating Uncertainties in Marine Biogeochemical Models: Benchmarking Aerosol Precursors. Atmosphere, 9(5), 184. https://doi.org/10.3390/atmos9050184

Olivier, L., Hoppema, M., and Becker, H.: Surface underway measurements of pCO_2, water temperature, salinity and other variables collected during R/V Polarstern cruises in the North Atlantic Ocean, South Atlantic Ocean, Southern Ocean and Arctic Ocean from 2024-12-24 to 2025-08-31 (NCEI Accession 0314939), NOAA National Centers for Environmental Information [data set], https://doi.org/10.25921/y6qs-j872, 2026.

Olivier, L. and Landschützer, P.: Surface underway measurements of partial pressure (or fugacity) of carbon dioxide, salinity and water temperature collected from the sailing vessel HOLCIM during the Vendée Globe 2024 race in the Atlantic Ocean, Pacific Ocean, Indian Ocean from 2024-11-10 to 2025-01-25 (NCEI Accession 0310919), NOAA National Centers for Environmental Information [data set], https://doi.org/10.25921/h176-tz06, 2026.

Olsen, A. Ehmen, T. and Becker, M.: Surface ocean and atmospheric fCO2 observations taken by a General Oceanics system on Ship of Opportunity Tukuma Arctica during 2025, ICOS ERIC -- Carbon Portal [data set], https://doi.org/10.18160/6exv-xdsk, 2026.

Omar, A., Skjelvan, I., and Kristensen, T. O.: Surface ocean fCO2 observations taken by a General Oceanics system on Sea-Cargo Express in 2025, ICOS ERIC -- Carbon Portal [data set], https://doi.org/10.18160/7PQC-P96W, 2026.

Orr, J. C., Najjar, R. G., Aumont, O., Bopp, L., Bullister, J. L., Danabasoglu, G., Doney, S. C., Dunne, J. P., Dutay, J.-C., Graven, H., Griffies, S. M., John, J. G., Joos, F., Levin, I., Lindsay, K., Matear, R. J., McKinley, G. A., Mouchet, A., Oschlies, A., Romanou, A., Schlitzer, R., Tagliabue, A., Tanhua, T., and Yool, A.: Biogeochemical protocols and diagnostics for the CMIP6 Ocean Model Intercomparison Project (OMIP), 10, 2169–2199, https://doi.org/10.5194/gmd-10-2169-2017, 2017.

Ortega, P., E. Guilyardi, D. Swingedouw, J. Mignot, and S. Nguyen: Reconstructing extreme amoc events through nudging of the ocean surface: a perfect model approach. Climate Dynamics, 49 (9), 3425–3441, 2017.

Padín, X. A., Huertas, I. E., Tovar-Sánchez, A., and Pena González, L. D.: Partial pressure (or fugacity) of carbon dioxide, water temperature, salinity and other variables collected from surface underway observations during the R/V Sarmiento De Gamboa DICHOSO-2 and MORIA cruises in the South and North Atlantic Ocean, Southern Ocean in 2025 (NCEI Accession 0314986), NOAA National Centers for Environmental Information [data set], https://doi.org/10.25921/406n-yb48, 2026.

Peters, G. P., Andrew, R., and Lennox, J.: Constructing an environmentally-extended multi-regional input–output table using the GTAP database, Economic Systems Research, 23, 131–152, https://doi.org/10.1080/09535314.2011.563234, 2011b.

Peters, G. P., Davis, S. J., and Andrew, R.: A synthesis of carbon in international trade, Biogeosciences, 9, 3247–3276, https://doi.org/10.5194/bg-9-3247-2012, 2012b.

Pierrot, D. and Wanninkhof, R.: Partial pressure of carbon dioxide, water temperature, salinity and other variables collected from surface underway observations during Ships of Opportunity (SOOP) M/V Le Commandant Charcot cruise lines in the Southern Ocean, South Atlantic Ocean, North Atlantic Ocean, Arctic Ocean in 2025 (NCEI Accession 0312635), NOAA National Centers for Environmental Information [data set], https://doi.org/10.25921/0ggc-0c52, 2026.

Pongratz, J., Smith, S. M., Schwingshackl, C., Dayathilake, L., Gasser, T., Grassi, G. and Pilli, R.: Chapter 7: Current levels of CDR. in The State of Carbon Dioxide Removal 2024 – 2nd Edition, https://doi.org/10.17605/OSF.IOZXSKB, 2024.

Poorter, H., Niklas, K. J., Reich, P. B., Oleksyn, J., Poot, P., & Mommer, L. (2012): Biomass allocation to leaves, stems and roots: meta-analyses of interspecific variation and environmental control. New Phytologist, 193, 30–50. https://doi.org/10.1111/j.1469-8137.2011.03952.x

Potapov, P., Hansen, M. C., Laestadius, L., Turubanova, S., Yaroshenko, A., Thies, C., Smith, W., Zhuravleva, I., Komarova, A., Minnemeyer, S., and Esipova, E.: The last frontiers of wilderness: Tracking loss of intact forest landscapes from 2000 to 2013, Sci. Adv., 3, e1600821, https://doi.org/10.1126/sciadv.1600821, 2017.

Poulter, B., Freeborn, P. H., Jolly, W. M., and Varner, J. M.: COVID-19 lockdowns drive decline in active fires in southeastern United States, PNAS, 118, e2105666118, https://doi.org/10.1073/pnas.2105666118, 2021.

Prather, M.: Interactive comment on "Carbon dioxide and climate impulse response functions for the computation of greenhouse gas metrics: a multi-model analysis" by F. Joos et al., Atmospheric Chem. Phys. Discuss., 12, C8465, 2012.

Prosperi, P., Bloise, M., Tubiello, F. N., Conchedda, G., Rossi, S., Boschetti, L., Salvatore, M., and Bernoux, M.: New estimates of greenhouse gas emissions from biomass burning and peat fires using MODIS Collection 6 burned areas, Climatic Change, 161, 415–432, https://doi.org/10.1007/s10584-020-02654-0, 2020.

Qin, Z., Zhu, Y., Canadell, J.G., Chen, M., Li, T., Mishra, U. and Yuan, W.: Global spatially explicit carbon emissions from land-use change over the past six decades (1961–2020). One Earth, 7(5), pp.835-847, 2024.

Qiu, C., Ciais, P., Zhu, D., Guenet, B., Peng, S., Petrescu, A. M. R., Lauerwald, R., Makowski, D., Gallego-Sala, A. V., Charman, D. J., and Brewer, S. C.: Large historical carbon emissions from cultivated northern peatlands, Sci. Adv., 7, eabf1332, https://doi.org/10.1126/sciadv.abf1332, 2021.

Raich, J.W., Potter, C.S. and Bhagawati, D.: Interannual variability in global soil respiration, 1980–94. Global Change Biology, 8(8), pp.800-812, 2002.

Rayner, N. A., Parker, D. E., Horton, E. B., Folland, C. K., Alexander, L. V., Rowell, D. P., Kent, E. C., and Kaplan, A.: Global analyses of sea surface temperature, sea ice, and night marine air temperature since the late nineteenth century, Journal of Geophysical Research: Atmospheres, 108, https://doi.org/10.1029/2002JD002670, 2003.

Rayner, P. J., Enting, I. G., Francey, R. J., and Langenfelds, R.: Reconstructing the recent carbon cycle from atmospheric CO2, δ13C and O2/N2 observations*, Tellus B, 51, 213–232, https://doi.org/10.1034/j.1600-0889.1999.t01-1-00008.x, 1999.

Reagan, J.R., D. Seidov, Z. Wang, D. Dukhovskoy, T.P. Boyer, R.A. Locarnini, O.K. Baranova, A.V. Mishonov, H.E. Garcia, C. Bouchard, S.L. Cross, and C.R. Paver. World Ocean Atlas 2023, Volume 2: Salinity. A. Mishonov, Technical Editor, NOAA Atlas NESDIS 90, doi.org/10.25923/70qt-9574

Regnier, P., Friedlingstein, P., Ciais, P., Mackenzie, F. T., Gruber, N., Janssens, I. A., Laruelle, G. G., Lauerwald, R., Luyssaert, S., Andersson, A. J., Arndt, S., Arnosti, C., Borges, A. V., Dale, A. W., Gallego-Sala, A., Goddéris, Y., Goossens, N., Hartmann, J., Heinze, C., Ilyina, T., Joos, F., LaRowe, D. E., Leifeld, J., Meysman, F. J. R., Munhoven, G., Raymond, P. A., Spahni, R., Suntharalingam, P., and Thullner, M.: Anthropogenic perturbation of the carbon fluxes from land to ocean, Nature Geosci, 6, 597–607, https://doi.org/10.1038/ngeo1830, 2013.

Rehder, G., Bittig, H., Glockzin, M., Neubert, S., Sadkowiak, B., and Steinberg, M.: Surface ocean and atmospheric fCO2 observations taken by a custom Ferrybox system with Los Gatos and Picarro gas analysers on the Finnmaid in 2025, ICOS ERIC -- Carbon Portal [data set], https://doi.org/10.18160/NA24-25YF, 2026.

Reichstein, M., Papale, D., Valentini, R., Aubinet, M., Bernhofer, C., Knohl, A., Laurila, T., Lindroth, A., Moors, E., Pilegaard, K., and Seufert, G.: Determinants of terrestrial ecosystem carbon balance inferred from European eddy covariance flux sites, Geophys. Res. Lett., 34, L01402, https://doi.org/10.1029/2006GL027880, 2007.

Rhein, M., Rintoul, S. R., Aoki, S., Campos, E., Chambers, D., Feely, R. A., Gulev, S., Johnson, G. C., Josey, S. A., Kostianoy, A., Mauritzen, C., Roemmich, D., and Talley, L. D.: Observations: Ocean, in: Climate Change 2013: The Physical Science Basis. Contribution of Working Group I to the Fifth Assessment Report of the Intergovernmental Panel on Climate Change [Stocker, T. F., Qin, D., Plattner, G.-K., Tignor, M., Allen, S. K., Boschung, J., Nauels, A., Xia, Y., Bex, V., and Midgley, P. M. (eds.)], Cambridge University Press, 255–316, ISBN: 9781107057991, 2013.

Rödenbeck, C., Bakker, D. C. E., Gruber, N., Iida, Y., Jacobson, A. R., Jones, S., Landschützer, P., Metzl, N., Nakaoka, S., Olsen, A., Park, G.-H., Peylin, P., Rodgers, K. B., Sasse, T. P., Schuster, U., Shutler, J. D., Valsala, V., Wanninkhof, R., and Zeng, J.: Data-based estimates of the ocean carbon sink variability – first results of the Surface Ocean CO2 Mapping intercomparison (SOCOM), Biogeosciences, 12, 7251–7278, https://doi.org/10.5194/bg-12-7251-2015, 2015.

Rödenbeck, C., DeVries, T., Hauck, J., Le Quéré, C., and Keeling, R. F.: Data-based estimates of interannual sea–air CO2 flux variations 1957–2020 and their relation to environmental drivers, Biogeosciences, 19, 2627–2652, https://doi.org/10.5194/bg-19-2627-2022, 2022.

Roobaert, A., Laruelle, G. G., Landschützer, P., and Regnier, P.: Uncertainty in the global oceanic CO2 uptake induced by wind forcing: quantification and spatial analysis, 15, 1701–1720, https://doi.org/10.5194/bg-15-1701-2018, 2018.

Rossi, S., Brandão De Melo, J., Ceccherini, G., Alkama, R., and Grassi, G. JRC global proxy maps of managed and unmanaged forest (Version 1.0). Zenodo. https://doi.org/10.5281/zenodo.14549036. 2024.

Rypdal, K., Paciornik, N., Eggleston, S., Goodwin, J., Irving, W., Penman, J., and Woodfield, M.: Volume 1: Introduction to the 2006 Guidelines in: 2006 IPCC guidelines for national greenhouse gas inventories, available at: https://www.ipcc-nggip.iges.or.jp/public/2006gl/vol1.html, last access: 21 January 2025, 2006.

Saatchi, S. S., Harris, N. L., Brown, S., Lefsky, M., Mitchard, E. T. A., Salas, W., Zutta, B. R., Buermann, W., Lewis, S. L., Hagen, S., Petrova, S., White, L., Silman, M., and Morel, A.: Benchmark map of forest carbon stocks in tropical regions across three continents, Proceedings of the National Academy of Sciences, 108, 9899–9904, https://doi.org/10.1073/pnas.1019576108, 2011.

Sallée, JB., Pellichero, V., Akhoudas, C. et al. Summertime increases in upper-ocean stratification and mixed-layer depth. Nature 591, 592–598 (2021). https://doi.org/10.1038/s41586-021-03303-x

Santana-Casiano, J. M., González-Dávila, M., Castro, A., Curbelo, D., Gonzalez Santana, D., and González, A.: CanOA 2025: Surface ocean fCO_2 observations taken by a General Oceanics system during 2025, ICOS ERIC -- Carbon Portal [data set], https://doi.org/10.18160/88C7-K7P9, 2026.

Santoro, M., and Cartus, O. (2021) ESA Biomass Climate Change Initiative (Biomass_cci): Global datasets of forest above-ground biomass for the years 2010, 2017 and 2018, v3, NERC EDS Centre for Environmental Data Analysis, http://dx.doi.org/10.5285/5f331c418e9f4935b8eb1b836f8a91b8

Santoro, M., Cartus, O., Quegan, S., Kay H., Lucas, R. M., Araza, A., Herold, M., Labrière, N., Chave, J., Rosenqvist, Å., Tadono, T., Kobayashi, K., Kellndorfer, J., Avitabile, V., Brown, H., Carreiras, J., Campbell, M. J., Cavlovic, J., Conceição Bispo, P., Gilani, H., Khan, M. L., Kumar, A., Lewis, S. L., Jingjing Liang, J., Mitchard, E. T. A., Pacheco-Pascagaza, A. M., Phillips, O. L., Ryan, C. M., Saikia, P., Schepaschenko, D., Sukhdeo, H., Verbeeck, H., Vieilledent, G., Wijaya, A., Willcock, S. and Seifert, F.M. (2024) Design and performance of the Climate Change Initiative Biomass global retrieval algorithm. Science of Remote Sensing. https://doi.org/10.1016/j.srs.2024.100169

Sarmiento, J. L., Orr, J. C., and Siegenthaler, U.: A perturbation simulation of CO2 uptake in an ocean general circulation model, J. Geophys. Res.-Oceans., 97, 3621–3645, https://doi.org/10.1029/91JC02849, 1992.

Sato, M., Hansen, J. E., McCormick, M. P., and Pollack, J. B.: Stratospheric aerosol optical depths, 1850–1990, Geophys. Res.-Atmos., 98, 22987–22994, https://doi.org/10.1029/93JD02553, 1993.

Saunois, M., Stavert, A. R., Poulter, B., Bousquet, P., Canadell, J. G., Jackson, R. B., Raymond, P. A., Dlugokencky, E. J., Houweling, S., Patra, P. K., Ciais, P., Arora, V. K., Bastviken, D., Bergamaschi, P., Blake, D. R., Brailsford, G., Bruhwiler, L., Carlson, K. M., Carrol, M., Castaldi, S., Chandra, N., Crevoisier, C., Crill, P. M., Covey, K., Curry, C. L., Etiope, G., Frankenberg, C., Gedney, N., Hegglin, M. I., Höglund-Isaksson, L., Hugelius, G., Ishizawa, M., Ito, A., Janssens-Maenhout, G., Jensen, K. M., Joos, F., Kleinen, T., Krummel, P. B., Langenfelds, R. L., Laruelle, G. G., Liu, L., Machida, T., Maksyutov, S., McDonald, K. C., McNorton, J., Miller, P. A., Melton, J. R., Morino, I., Müller, J., Murguia-Flores, F., Naik, V., Niwa, Y., Noce, S., O'Doherty, S., Parker, R. J., Peng, C., Peng, S., Peters, G. P., Prigent, C., Prinn, R., Ramonet, M., Regnier, P., Riley, W. J., Rosentreter, J. A., Segers, A., Simpson, I. J., Shi, H., Smith, S. J., Steele, L. P., Thornton, B. F., Tian, H., Tohjima, Y., Tubiello, F. N., Tsuruta, A., Viovy, N., Voulgarakis, A., Weber, T. S., van Weele, M., van der Werf, G. R., Weiss, R. F., Worthy, D., Wunch, D., Yin, Y., Yoshida, Y., Zhang, W., Zhang, Z., Zhao, Y., Zheng, B., Zhu, Q., Zhu, Q., and Zhuang, Q.: The Global Methane Budget 2000–2017, Earth Syst. Sci. Data, 12, 1561–1623, https://doi.org/10.5194/essd-12-1561-2020, 2020.

Schuldt, K. N., Mund, J., Aalto, T., Abshire, J. B., Aikin, K., Allen, G., Andrews, A., Apadula, F., Arnold, S., Baier, B., Bakwin, P., Bartyzel, J., Bentz, G., Bergamaschi, P., Beyersdorf, A., Biermann, T., Biraud, S. C., Blanc, P.-E., Boenisch, H., Bowling, D., Brailsford, G., Brand, W. A., Brunner, D., Bui, T. P., Bäni, L., Calzolari, F., Chang, C. S., Chen, H., Chen, G., Chmura, L., Clark, S., Climadat, S., Colomb, A., Commane, R., Conen, F., Conil, S., Couret, C., Cristofanelli, P., Cuevas, E., Curcoll, R., Daube, B., Davis, K. J., De Mazière, M., De Wekker, S., Dean-Day, J. M., Della Coletta, J., Delmotte, M., Di Iorio, T., DiGangi, E., DiGangi, J. P., Elkins, J. W., Elsasser, M., Emmenegger, L., Fang, S., Fischer, M. L., Forster, G.,

France, J., Frumau, A., Fuente-Lastra, M., Galkowski, M., Gatti, L. V., Gehrlein, T., Gerbig, C., Gheusi, F., Gloor, E., Goto, D., Griffis, T., Hammer, S., Hanisco, T. F., Hanson, C., Haszpra, L., Hatakka, J., Heimann, M., Heliasz, M., Heltai, D., Henne, S., Hensen, A., Hermans, C., Hermansen, O., Hintsa, E., Hoheisel, A., Holst, J., Iraci, L. T., Ivakhov, V., Jaffe, D. A., Jordan, A., Joubert, W., Karion, A., Kawa, S. R., Kazan, V., Keeling, R. F., Keronen, P., Kim, J., Klausen, J., Kneuer, T., Kolari, P., Kominkova, K., Kort, E., Kozlova, E., Krummel, P. B., Kubistin, D., Kulawik, S. S., Kumps, N., Labuschagne, C., Lam, D. H., Lan, X., Langenfelds, R. L., Lanza, A., Laurent, O., Laurila, T., Lauvaux, T., Lavric, J., Law, B. E., Lee, J., Lehner, I., Lehtinen, K., Leppert, R., Leskinen, A., Leuenberger, M., Leung, W. H., Levin, I., Levula, J., Lin, J., Lindauer, M., Lindroth, A., Loh, Z. M., Lopez, M., Lunder, C. R., Löfvenius, M. O., Machida, T., Mammarella, I., Manca, G., Manning, A., Manning, A., Marek, M. V., Marklund, P., Marrero, J. E., Martin, D., Martin, M. Y., Martins, G. A., Matsueda, H., McKain, K., Meijer, H., Meinhardt, F., Merchant, L., Metzger, J.-M., Mihalopoulos, N., Miles, N. L., Miller, J. B., Miller, C. E., Mitchell, L., Monteiro, V., Montzka, S., Moore, F., Moossen, H., Morgan, E., Morgui, J.-A., Morimoto, S., Munger, J. W., Munro, D., Mutuku, M., Myhre, C. L., Mölder, M., Müller-Williams, J., Necki, J., Newman, S., Nichol, S., Nisbet, E., Niwa, Y., Njiru, D. M., Noe, S. M., Nojiri, Y., O'Doherty, S., Obersteiner, F., Paplawsky, B., Parworth, C. L., Peischl, J., Peltola, O., Peters, W., Philippon, C., Piacentino, S., Pichon, J. M., Pickers, P., Piper, S., Pitt, J., Plass-Dülmer, C., Platt, S. M., Prinzivalli, S., Ramonet, M., Ramos, R., Reyes-Sanchez, E., Richardson, S. J., Rigouleau, L.-J., Riris, H., Rivas, P. P., Rothe, M., Roulet, Y.-A., Ryerson, T., Ryoo, J.-M., Sargent, M., Sasakawa, M., Scheeren, B., Schmidt, M., Schuck, T., Schumacher, M., Seibel, J., Seifert, T., Sha, M. K., Shepson, P., Shook, M., Sloop, C. D., Smith, P. D., Spain, G., St. Clair, J. M., Steger, D., Steinbacher, M., Stephens, B., Sweeney, C., Sørensen, L. L., Taipale, R., Takatsuji, S., Tans, P., Thoning, K., Timas, H., Torn, M., Trisolino, P., Turnbull, J., Vermeulen, A., Viner, B., Vitkova, G., Walker, S., Watson, A., Weiss, R., Weyrauch, D., Wofsy, S. C., Worsey, J., Worthy, D., Xueref-Remy, I., Yates, E. L., Young, D., Yver-Kwok, C., Zaehle, S., Zahn, A., Zellweger, C., Zimnoch, M., de Souza, R. A., di Sarra, A. G., van Dinther, D., and van den Bulk, P. (2023) Multi-laboratory compilation of atmospheric carbon dioxide data for the period 1957-2022; obspack_co2_1_GLOBALVIEWplus_v9.0_2023-09-09; NOAA Earth System Research Laboratory, Global Monitoring Laboratory. http://doi.org/10.25925/20230801.

Schuldt, K. N., Jacobson, A. R., Aalto, T., Andrews, A., Apadula, F., Arnold, S., Bakwin, P., Bartyzel, J., Bergamaschi, P., Biermann, T., Biraud, S. C., Blanc, P.-E., Bäni, L., Calzolari, F., Chen, H., Chmura, L., Colomb, A., Condori, L., Conen, F., Conil, S., Couret, C., Cristofanelli, P., Cuevas, E., De Mazière, M., De Wekker, S., Della Coletta, J., Delmotte, M., Di Iorio, T., Elsasser, M., Emmenegger, L., Fischer, M. L., Forster, G., Frumau, A., Fuente-Lastra, M., Galkowski, M., Gheusi, F., Hammer, S., Hatakka, J., Heliasz, M., Heltai, D., Hensen, A., Hermans, C., Hermansen, O., Hoheisel, A., Holst, J., Jaffe, D. A., Karion, A., Kazan, V., Keronen, P., Kneuer, T., Kolari, P., Kominkova, K., Krummel, P. B., Kubistin, D., Kumps, N., Lan, X., Langenfelds, R. L., Lanza, A., Laurent, O., Laurila, T., Lee, J., Lehner, I., Lehtinen, K., Leskinen, A., Leuenberger, M., Levin, I., Levula, J., Lindauer, M., Lindroth, A., Loh, Z. M., Lopez, M., Lunder, C. R., Löfvenius, M. O., Mammarella, I., Manca, G., Manning, A., Manning, A., Marek, M. V., Marklund, P., McKain, K., Meijer, H., Meinhardt, F., Metzger, J.-M., Miller, C. E., Miller, J. B., Myhre, C. L., Mölder, M., Müller-Williams, J., Necki, J., O'Doherty, S., Peltola, O., Philippon, C., Piacentino, S., Pichon, J. M., Pickers, P., Pitt, J., Plass-Dülmer, C., Platt, S. M., Ramonet, M., Ramos, R., Reyes-Sanchez, E., Rigouleau, L.-J., Rivas, P. P., Roulet, Y.-A., Scheeren, B., Schmidt, M., Schumacher, M., Sha, M. K., Sloop, C. D., Smith, P. D., Steger, D., Steinbacher, M., Sweeney, C., Sørensen, L. L., Taipale, R., Tans, P., Thoning, K., Trisolino, P., Turnbull, J., Vermeulen, A., Viner, B., Vitkova, G., Weyrauch, D., Worthy, D., Xueref-Remy, I., Young, D., Yver-Kwok, C., Zimnoch, M., di Sarra, A. G., van Dinther, D., and van den Bulk, P. (2024) Multi-laboratory compilation of atmospheric carbon dioxide data for the period 2023-2024; obspack_co2_1_NRT_v9.2_2024-03-25; NOAA Earth System Research Laboratory, Global Monitoring Laboratory. http://doi.org/10.25925/20240215.

Sharp, J. D., Pierrot, D., Humphreys, M. P., Epitalon, J.-M., Orr, J. C., Lewis, E. R., and Wallace, D. W. R.: CO2SYSv3 for MATLAB, , https://doi.org/10.5281/ZENODO.3950563, 2020.

Skjelvan, I., Kristensen, T. O., and Omar, A.: Surface ocean fCO2 observations taken by a General Oceanics system on the Research Vessel G. O. Sars during 2025, ICOS ERIC -- Carbon Portal [data set], https://doi.org/10.18160/G60G-VQ58, 2026.

Smith, T. M., Reynolds, R. W., Peterson, T. C., & Lawrimore, J.: Improvements to NOAA's historical merged land–ocean surface temperature analysis (1880–2006). Journal of climate, 21(10), 2283-2296, 2008.

Sospedra-Alfonso, R., W. J. Merryfield, G. J. Boer, V. V. Kharin, W.-S. Lee, C. Seiler, and J. R. Christian: Decadal climate predictions with the canadian earth system model version 5 (canesm5). Geoscientific Model Development, 14 (11), 6863–6891, 2021.

Souza, C. M., Z. Shimbo, J., Rosa, M. R., Parente, L. L., A. Alencar, A., Rudorff, B. F. T., Hasenack, H., Matsumoto, M., G. Ferreira, L., Souza-Filho, P. W. M., de Oliveira, S. W., Rocha, W. F., Fonseca, A. V., Marques, C. B., Diniz, C. G., Costa, D., Monteiro, D., Rosa, E. R., Vélez-Martin, E., Weber, E. J., Lenti, F. E. B., Paternost, F. F., Pareyn, F. G. C., Siqueira, J. V., Viera, J. L., Neto, L. C. F., Saraiva, M. M., Sales, M. H., Salgado, M. P. G., Vasconcelos, R., Galano, S., Mesquita, V. V., and Azevedo, T.: Reconstructing Three Decades of Land Use and Land Cover Changes in Brazilian Biomes with Landsat Archive and Earth Engine, Remote Sens., 12, 2735, https://doi.org/10.3390/rs12172735, 2020.

Steinhoff, T., Gkritzalis, T., Jones, S., Macovei, V.A., Neill, C., Schuster, U., Akl, J., Arruda, R., Atamanchuk, D., Barry, M., Beaumont, L., Cantoni, C., Dickson, A., Fahning, J., Fought, J., Frangoulis, C., Gutiérrez-Loza, L., Hagan, C., Honkanen, M., Kielosto, S., Kinski, N., Körtzinger, A., Landschützer, P., Lauvset, S.K., Lawrence-Slavas, N., Li, Q.,

Luchetta, A., Malarde, D., Paulsen, M., Ritschel, M., Rutgersson, A., Sanders, R., Shitashima, K., Spaulding, R., Stamataki, N., Stenbäck, K., Sutton, A., Tatkiewicz, W., Telszewski, M., Theetaert, H., Tilbrook, B., Wanninkhof, R.: The ICOS OTC pCO2 instrument intercomparison. Limnology and Oceanography: Methods, 1-66, http://doi.org/10.1002/lom3.10727, 2025.

Sutton, A. J., Hales, B., Musielewicz, S., Maenner Jones, S., Bott, R., and Osborne, J.: High-resolution ocean and atmosphere pCO_2 time-series measurements from mooring CB-06_125W_43N in the North Pacific Ocean (NCEI Accession 0190840), subset used: CB-06_125W_43N_Jan2025_May2025, NOAA National Centers for Environmental Information [data set], https://doi.org/10.25921/rr8z-se53, 2025a.

Sutton, A. J., Sabine, C. L., Dietrich, C., Maenner Jones, S., Musielewicz, S., Bott, R., and Osborne, J.: High-resolution ocean and atmosphere pCO_2 time-series measurements from mooring Papa_145W_50N in the North Pacific Ocean (NCEI Accession 0100074), subset used: Papa_145W_50N_Aug2024_May2025, NOAA National Centers for Environmental Information [data set], https://doi.org/10.3334/cdiac/otg.tsm_papa_145w_50n, 2025b.

Sutton, A. J., Sabine, C. L., Dietrich, C., Maenner Jones, S., Musielewicz, S., Bott, R., and Osborne, J.: High-resolution ocean and atmosphere pCO_2 time-series measurements from mooring KEO_145E_32N in the North Pacific Ocean (NCEI Accession 0100071), subset used: KEO_145E_32N_Nov2024_Apr2025, NOAA National Centers for Environmental Information [data set], https://doi.org/10.3334/cdiac/otg.tsm_keo_145e_32n, 2026a.

Sutton, A. J., Sabine, C. L., Trull, T., Dietrich, C., Maenner Jones, S., Musielewicz, S., Bott, R., and Osborne, J.: High-resolution ocean and atmosphere pCO_2 time-series measurements from mooring SOFS_142E_46S in the Indian Ocean (NCEI Accession 0118546), subset used: SOFS_142E_46S_Apr2024_Apr2025, NOAA National Centers for Environmental Information [data set], https://doi.org/10.3334/cdiac/otg.tsm_sofs_142w_46s, 2026b.

Sweeney, C., Baier, B., McAuliffe, A. M., and Munro, D. R.: Surface underway measurements of partial pressure of carbon dioxide (pCO_2), sea surface temperature, sea surface salinity and barometric pressure during R/V Nathaniel B. Palmer expeditions in the Southern Ocean, South Pacific Ocean, Drake Passage in 2025 (NCEI Accession 0312069), NOAA National Centers for Environmental Information [data set], https://doi.org/10.25921/4ez1-ck76, 2026a.

Sweeney, C., Baier, B., McAuliffe, A. M., and Munro, D. R.: Surface underway measurements of partial pressure of carbon dioxide (pCO_2), sea surface temperature, sea surface salinity and barometric pressure during R/V Sikuliaq expeditions in the Pacific Ocean, Gulf of Alaska, Bering Sea, Beaufort Sea, Arctic Ocean in 2025 (NCEI Accession 0311966), NOAA National Centers for Environmental Information [data set], https://doi.org/10.25921/nhdc-3328, 2026b.

Sweeney, C., Baier, B., McAuliffe, A. M., and Munro, D. R.: Surface underway measurements of partial pressure of carbon dioxide (pCO_2), sea surface temperature, sea surface salinity and barometric pressure during the USCGC Healy expeditions in the North Pacific Ocean, Gulf of Alaska, Bering Sea, Chukchi Sea, Beaufort Sea, Arctic Ocean in 2025 (NCEI Accession 0312070), NOAA National Centers for Environmental Information [data set], https://doi.org/10.25921/3syk-0t70, 2026c.

Swart, N. C. et al.: The Canadian Earth System Model version 5 (CanESM5. 0.3). Geoscientific Model Development, 12 (11), 4823–4873, 2019.

Tang, X., Fan, S., Zhang, W., Gao, S., Chen, G. and Shi, L.: Global variability in belowground autotrophic respiration in terrestrial ecosystems. Earth System Science Data, 11(4), pp.1839-1852, 2019.

Tang, X., Fan, S., Du, M., Zhang, W., Gao, S., Liu, S., Chen, G., Yu, Z. and Yang, W., 2020. Spatial and temporal patterns of global soil heterotrophic respiration in terrestrial ecosystems. Earth System Science Data, 12(2), pp.1037-1051.

Tatebe, H. et al.: The initialization of the MIROC climate models with hydrographic data assimilation for decadal prediction. Journal of Meteorological Society of Japan, 90A, 275–294, 2012.

Terhaar, J., Bopp, L., Friedlingstein, P., Frölicher, T., Hollitzer, H., Ilyina, T., Kwiatkowski, L., Lerner, P., Li, H., Romanou, A., Schwinger, J., Séférian, R., and Wienkers, A.: Observation-based constraint suggests larger ocean carbon uptake and stronger climate feedbacks, EGUsphere [preprint], https://doi.org/10.5194/egusphere-2026-5757, 2026.

Terhaar, J., Frölicher, T. L., and Joos, F.: Observation-constrained estimates of the global ocean carbon sink from Earth system models, Biogeosciences, 19, 4431–4457, https://doi.org/10.5194/bg-19-4431-2022, 2022.

Thomason, L. W., Ernest, N., Millán, L., Rieger, L., Bourassa, A., Vernier, J.-P., Manney, G., Luo, B., Arfeuille, F., and Peter, T.: A global space-based stratospheric aerosol climatology: 1979–2016, 10, 469–492, https://doi.org/10.5194/essd-10-469-2018, 2018.

Thurner, M., Beer, C., Santoro, M., Carvalhais, N., Wutzler, T., Schepaschenko, D., Shvidenko, A., Kompter, E., Ahrens, B., Levick, S. R., and Schmullius, C.: Carbon stock and density of northern boreal and temperate forests, Global Ecology and Biogeography, 23, 297–310, https://doi.org/10.1111/geb.12125, 2014.

Tian, H., Yao, Y., Li, Y., Shi, H., Pan, S., Najjar, R. G., Pan, N., Bian, Z., Ciais, P., Cai, W., Dai, M., Friedrichs, M. A. M., Li, H., Lohrenz, S., and Leung, L. R.: Increased Terrestrial Carbon Export and CO2 Evasion From Global Inland Waters Since the Preindustrial Era, Global Biogeochemical Cycles, 37, e2023GB007776, https://doi.org/10.1029/2023GB007776, 2023.

Tilbrook, B., Neill, C., van Ooijen, E., Passmore, A., and Black, J.: Partial pressure (or fugacity) of carbon dioxide, salinity, oxygen and other variables collected from time series observations from Mooring Maria_Island_42S_148E deployed in the Tasman Sea, Pacific Ocean (NCEI Accession 0165305), NOAA National Centers for Environmental Information [data set], https://doi.org/10.7289/V5BV7DT6, 2017.

Tilbrook, B., Neill, C., van Ooijen, E., Passmore, A., and Black, J.: Partial pressure (or fugacity) of carbon dioxide, water temperature, salinity and other variables collected from time series observations from Mooring Kangaroo_Island_35S_136E deployed in the South Australian Basin near Kangaroo_Island (NCEI Accession 0253461), NOAA National Centers for Environmental Information [data set], https://doi.org/10.25921/c2ry-gk21, 2022.

Tilbrook, B., Neill, C., and Akl, J.: Integrated Marine Observing System (IMOS) sea surface and atmospheric fCO_2 measurements in the South Pacific Ocean, Tasman Sea onboard R/V Investigator in 2025 (NCEI Accession 0310599), NOAA National Centers for Environmental Information [data set], https://doi.org/10.25921/9qgr-pj77, 2025.

Tilbrook, B., Neill, C., Akl, J., and Sallée, J.-B.: Integrated Marine Observing System (IMOS) sea surface and atmospheric fCO_2 measurements in the South Pacific Ocean, Southern Ocean, Tasman Sea onboard R/V L'Astrolabe in 2025 (NCEI Accession 0311455), NOAA National Centers for Environmental Information [data set], https://doi.org/10.25921/11gg-bz22, 2026.

Tilbrook, B., van Ooijen, E., Neill, C., Sutton, A. J., Sabine, C. L., and Musielewicz, S.: High-resolution ocean and atmosphere pCO_2 time-series measurements from mooring Heron_Island_152E_23 in the Tasman Sea, South Pacific Ocean (NCEI Accession 0100062), NOAA National Centers for Environmental Information [data set], https://doi.org/10.3334/cdiac/otg.tsm_heron_152e_23s, 2012.

Tramontana, G., Jung, M., Schwalm, C. R., Ichii, K., Camps-Valls, G., Ráduly, B., Reichstein, M., Arain, M. A., Cescatti, A., Kiely, G., Merbold, L., Serrano-Ortiz, P., Sickert, S., Wolf, S., and Papale, D.: Predicting carbon dioxide and energy fluxes across global FLUXNET sites withregression algorithms, Biogeosciences, 13, 4291–4313, https://doi.org/10.5194/bg-13-4291-2016, 2016.

Tubiello, F. N., Branthomme, A., Obli-Laryea, G., Piccoli, M., Ramadan, N., Condor, R. D., Wanner, N., Brivio, R., Jonsson, Ö., Conchedda, G., and Pekkarinen, A.: FAO estimates of net forest emissions and removals, 1990–2025, Earth Syst. Sci. Data, 18, 6799–6813, https://doi.org/10.5194/essd-18-6799-2026, 2026

UN: United Nations Statistics Division: National Accounts Main Aggregates Database, available at: http://unstats.un.org/unsd/snaama/Introduction.asp, last access: 21 January 2025, 2021.

Uppala, S. M., Kållberg, P. W., Simmons, A. J., Andrae, U., Bechtold, V. D. C., Fiorino, M., ... & Woollen, J.: The ERA-40 re-analysis. Quarterly Journal of the Royal Meteorological Society: A journal of the atmospheric sciences, applied meteorology and physical oceanography, 131(612), 2961-3012, 2005.

van de Velde, S.: Surface underway measurements of fugacity of carbon dioxide (fCO_2), sea surface temperature, sea surface salinity and barometric pressure during R/V Polaris II cruises in the South Pacific Ocean in 2025 (NCEI Accession 0311481), NOAA National Centers for Environmental Information [data set], https://doi.org/10.25921/32pw-2808, 2026.

van de Velde, S. and Marriner, A.: Surface underway measurements of fugacity of carbon dioxide (fCO_2), sea surface temperature, sea surface salinity and barometric pressure during R/V Tangaroa cruises in the South Pacific Ocean, Southern Ocean in 2025 (NCEI Accession 0311483), NOAA National Centers for Environmental Information [data set], https://doi.org/10.25921/72p3-9k79, 2026.

Van Der Werf, G. R., Randerson, J. T., Van Wees, D., Chen, Y., Giglio, L., Hall, J., Vernooij, R., Mu, M., Binte Shahid, S., Barsanti, K. C., Yokelson, R., and Morton, D. C.: Landscape fire emissions from the 5th version of the Global Fire Emissions Database (GFED5), Sci Data, 12, 1870, https://doi.org/10.1038/s41597-025-06127-w, 2025.

Vermote, E. and NOAA CDR Program: NOAA Climate Data Record (CDR) of AVHRR Leaf Area Index (LAI) and Fraction of Absorbed Photosynthetically Active Radiation (FAPAR), Version 5, https://doi.org/10.7289/V5TT4P69, 2018.

Viovy, N.: CRUNCEP data set, available at: ftp://nacp.ornl.gov/synthesis/2009/frescati/temp/land_use_change/original/readme.htm, last access: 21 January 2025, 2016.

Wanninkhof, R.: Relationship between wind speed and gas exchange over the ocean, J. Geophys. Res.-Oceans., 97, 7373–7382, https://doi.org/10.1029/92JC00188, 1992.

Wanninkhof, R.: Relationship between wind speed and gas exchange over the ocean revisited, Limnol. Oceanogr. Methods., 12, 351–362, https://doi.org/10.4319/lom.2014.12.351, 2014.

Wanninkhof, R., Park, G.-H., Takahashi, T., Sweeney, C., Feely, R., Nojiri, Y., Gruber, N., Doney, S. C., McKinley, G. A., Lenton, A., Le Quéré, C., Heinze, C., Schwinger, J., Graven, H., and Khatiwala, S.: Global ocean carbon uptake: magnitude, variability and trends, Biogeosciences, 10, 1983–2000, https://doi.org/10.5194/bg-10-1983-2013, 2013.

Wanninkhof, R., Pierrot, D., and Sullivan, K. F.: Partial pressure of carbon dioxide, temperature, salinity and other variables collected from surface underway observations during Ships of Opportunity (SOOP) M/V Celebrity Equinox cruise lines in the Caribbean Sea, North Atlantic Ocean in 2025 (NCEI Accession 0302087), NOAA National Centers for Environmental Information [data set], https://doi.org/10.25921/1q1z-tx93, 2025a.

Wanninkhof, R. and Pierrot, D.: Partial pressure of carbon dioxide, temperature, salinity and other variables collected from the coastal surface underway observations from NOAA Ship Gordon Gunter in the Gulf of America and North Atlantic Ocean in 2025 (NCEI Accession 0312683), NOAA National Centers for Environmental Information [data set], https://doi.org/10.25921/ktst-qc70, 2026a.

Wanninkhof, R. and Pierrot, D.: Partial pressure of carbon dioxide, temperature, salinity and other variables collected from the coastal surface underway observations from NOAA Ship Henry B. Bigelow in the North Atlantic Ocean, US North-East Coast in 2025 (NCEI Accession 0312765), NOAA National Centers for Environmental Information [data set], https://doi.org/10.25921/z2j3-x957, 2026b.

Wanninkhof, R., Triñanes, J., Pierrot, D., Munro, D. R., Sweeney, C., and Fay, A. R.: Trends in Sea-Air CO2 Fluxes and Sensitivities to Atmospheric Forcing Using an Extremely Randomized Trees Machine Learning Approach, Global Biogeochemical Cycles, 39, e2024GB008315, https://doi.org/10.1029/2024GB008315, 2025.

Wanninkhof, R., Sullivan, K. F., and Pierrot, D.: Partial pressure of carbon dioxide, temperature, salinity and other variables collected from surface underway observations during Ships of Opportunity (SOOP) C/S Allure of the Seas lines in the North Atlantic Ocean in 2025 (NCEI Accession 0302085), NOAA National Centers for Environmental Information [data set], https://doi.org/10.25921/8hkd-w728, 2025b.

Watanabe, M., H. Tatebe, H. Koyama, T. Hajima, M. Watanabe, and M. Kawamiya: Importance of El Ni˜no reproducibility for reconstructing historical CO2 flux variations in the equatorial Pacific. Ocean Science, 16, 1431–1442, 2020.

Weiss, R. F. and Price, B. A.: Nitrous oxide solubility in water and seawater, Marine Chemistry, 8, 347–359, https://doi.org/10.1016/0304-4203(80)90024-9, 1980.

Willey, D. A., Fine, R. A., Sonnerup, R. E., Bullister, J. L., Smethie, W. M., and Warner, M. J.: Global oceanic chlorofluorocarbon inventory, Geophys. Res. Lett., 31, L01303, https://doi.org/10.1029/2003GL018816, 2004.

Woolf, D. K., P. E. Land, J. D. Shutler, L. M. Goddijn-Murphy, and C. J. Donlon: On the calculation of air-sea fluxes of CO2 in the presence of temperature and salinity gradients, J. Geophys. Res. Oceans, 121, 1229–1248, https://doi.org/10.1002/2015JC011427, 2016.

Xia, J., Chen, Y., Liang, S., Liu, D., and Yuan, W.: Global simulations of carbon allocation coefficients for deciduous vegetation types, Tellus B, 67, 28016, https://doi.org/10.3402/tellusb.v67.28016, 2015.

Xu, L., Saatchi, S.S., Yang, Y., Yu, Y., Pongratz, J., Bloom, A.A., Bowman, K., Worden, J., Liu, J., Yin, Y., Domke, G., McRoberts, R.E., Woodall, C., Nabuurs, G.-J., de-Miguel, S., Keller, M., Harris, N., Maxwell, S., & Schimel, D. (2021), Zenodo, doi:10.5281/zenodo.4161694

Yu, Z., Ciais, P., Piao, S., Houghton, R. A., Lu, C., Tian, H., Agathokleous, E., Kattel, G. R., Sitch, S., Goll, D., Yue, X., Walker, A., Friedlingstein, P., Jain, A. K., Liu, S., and Zhou, G.: Forest expansion dominates China's land carbon sink since 1980, Nat. Commun., 13, 5374, https://doi.org/10.1038/s41467-022-32961-2, 2022.

Zeng, J., Nojiri, Y., Landschützer, P., Telszewski, M., and Nakaoka, S.-I.: A global surface ocean fCO2 climatology based on a feed forward neural network, J. Atmos. Ocean. Tech., 31, 1838–1849, https://doi.org/10.1175/JTECH-D-13-00137.1, 2014.

Zeng J., Matsunaga T., Tan Z-H., Saigusa N., Shirai T., Tang Y., Peng S. and Fukuda Y.: Global terrestrial carbon fluxes of 1999–2019 estimated by upscaling eddy covariance data with a random forest, Sci. Data, 7, 1–11, https://doi.org/10.1038/s41597-020-00653-5, 2020.

Zhang, X., Liao, E., Lu, W., Wu, Z., Wang, G., Zhu, X., and Liang, S.: A surface ocean p CO2 product with improved representation of interannual variability using a vision transformer-based model, Earth Syst. Sci. Data, 17, 6071–6095, https://doi.org/10.5194/essd-17-6071-2025, 2025.

Zheng, B., Chevallier, F., Yin, Y., Ciais, P., Fortems-Cheiney, A., Deeter, M. N., Parker, R. J., Wang, Y., Worden, H. M., and Zhao, Y.: Global atmospheric carbon monoxide budget 2000–2017 inferred from multi-species atmospheric inversions, Earth Syst. Sci. Data, 11, 1411–1436, https://doi.org/10.5194/essd-11-1411-2019, 2019.

Zuo, H., Balmaseda, M. A., Tietsche, S., Mogensen, K., & Mayer, M.: The ECMWF operational ensemble reanalysis–analysis system for ocean and sea ice: a description of the system and assessment. Ocean science, 15(3), 779-808, 2019.